

Simulations of cosmic muons and background radiations for muon tomography and underground experiments



David Woodward

Supervisor: Dr. Vitaly Kudryavtsev

Department of Physics & Astronomy
University of Sheffield

This dissertation is submitted for the degree of
Doctor of Philosophy

March 2018

Declaration

I declare that the contents of this dissertation are original and have not been submitted in whole or in part for consideration for any other degree or qualification in this, or any other university. The author's contribution to the work detailed in this thesis is specified below. Chapter 1 contains background information relevant to the research described in later sections.

- **Section 2.1**

The Geant4-based simulation and analysis framework was developed by the author and Joel Klinger (University of Sheffield). The author was responsible for developing code related to particle tracking, geometry construction and the generation of primary muons. The analysis was performed using codes developed by the author and Joel Klinger. The contributions of other collaborators are specifically mentioned in the text.

- **Section 2.2**

The work presented in this section is the result of collaboration with other members of the LUX-ZEPLIN (LZ) simulation group. The author was responsible for the implementation of the MUSUN code within the LUXSim/BACCARAT framework and for writing codes to run simulations on the Sheffield HEP computing cluster. The author was part of the working group that developed the post-simulation processing codes and analysis.

- **Section 3.1**

The author was responsible for all aspects of the decay generator and its implementation in other code bases.

- **Section 3.2**

The author was responsible for all aspects of the simulation, production and analysis codes. The GEANT4-based simulation is based on a framework provided by Joel Klinger. The author acknowledges the assistance of undergraduate student Daniel Gillard (University of Sheffield).

- **Section 3.3**

The author developed the event biasing scheme for simulations using LUXSim/BAC-CARAT and codes to run the simulations on the Sheffield HEP computing cluster. The author was a member of the simulation group responsible for the development of the analysis procedures. The author acknowledges the assistance of undergraduate students Nigel Gibbions (University of Sheffield) and Aurélie Astoul (Magistère de Physique Fondamentale d'Orsay).

David Woodward

March 2018

Acknowledgements

Firstly, I would like to thank my supervisor, Dr. Vitaly Kudryavtsev for his help and guidance throughout the course of my PhD. It has been an absolute pleasure to work with him. I would also like to thank my co-supervisor, Prof. Jon Gluyas at Durham University, for affording me the opportunity to work on this thesis project.

I have been lucky to be a member of two fantastic collaborations and my work has been enhanced greatly by talented people on both the muon tomography project and the LZ experiment. In particular I would like to acknowledge the help of Joel Klinger, who guided me through the early parts of my PhD. Without his help I would probably still be figuring out how to use GEANT4.

It has been a pleasure to work in the Sheffield particle physics group over the last 4 years. Special thanks to Dr. Elena Korolkova, who I worked closely with on LZ, for all of her help and advice. To all those I shared an office with: Tim, Leon, Jon, Patrick, Nic, Liam, Celeste - thanks for making my working days all the more pleasurable.

I was very lucky to share my time as a PhD student with Mike, Andy, Matt, Karl, Anthony and Calum. Special thanks must go to Calum for enduring the highs and lows of following Sheffield Wednesday across the country. I have also been supported by a fantastic group of friends throughout my time studying at Sheffield University. I cannot mention all of them by name, but I would particularly like to thank Amy, Jamie, Andy, Charlotte and Jack for their support. Also, to my housemates for 4 years: Ben, Martin, Tom, and especially Rob and Jonny who were ever-present at Springvale Road. Thanks for making my time there truly special.

One of my biggest passions in life is football, and I have no doubt played too much of it throughout this PhD. I have been privileged to be a part of many teams and made some great friends. AC Southside FC and Byron House FC have been a fixture of my weekends for a while now, and I like to think those cold, wet mornings running around a muddy field somehow helped me along the way.

Finally, and most importantly, I would like to thank my family. Mum, Dad, Alice and Emily - I couldn't have done this without your constant love and support.

Abstract

Controlling atmospheric levels of greenhouse gases is required to mitigate the effects of anthropogenic climate change. A promising solution to reduce emissions of carbon dioxide (CO_2) to the atmosphere is carbon capture and storage (CCS). These technologies comprise methods to isolate CO_2 at its point of production, and inject it underground into a suitable geological formation for long-term storage. While CCS has been demonstrated at a number of sites across the world, there are challenges involved in monitoring the fate of CO_2 in the subsurface after its injection. Muon tomography has been suggested as a monitoring technique that can compliment other methods such as repeat seismic surveys. It is proposed that muon detectors, which can be deployed in underground boreholes beneath a storage site, will measure changes in muon intensity caused by variations in the density distribution of the overburden due to the presence of CO_2 . In this thesis, muon simulations of a geological repository are presented to determine the feasibility of muon tomography for monitoring carbon storage sites. In addition, simulations of the local radioactive backgrounds for borehole detectors have been developed to understand their setup and operating conditions. It is found that the constant injection of CO_2 into a typical storage formation leads to changes in density that are observable as a statistically significant change in muon intensity within 50 days of data taking.

While cosmic-ray muons provide a signal for muon tomography, they are an unwanted background for underground experiments searching for rare physics events. Backgrounds from radioactivity in the vicinity of a sensitive detector may also obscure potential signals and limit sensitivity. Using the models developed for muon tomography simulations, the muon-induced and laboratory backgrounds for the LUX-ZEPLIN (LZ) dark matter experiment have been characterised. It is found that the rate from these sources is subdominant to internal detector backgrounds.

Table of contents

List of figures	xi
List of tables	xxi
1 Geological carbon storage, cosmic rays and background radiations	1
1.1 Carbon capture and storage	1
1.1.1 Storage and trapping	3
1.1.2 Monitoring techniques	4
1.2 Cosmic rays	13
1.2.1 Muons at the Earth's surface	15
1.3 Muon distribution underground	19
1.3.1 Muon transport through materials	20
1.3.2 Muons underground	22
1.4 Applications of muons	25
1.5 Backgrounds for underground detectors	25
1.5.1 Cosmogenic backgrounds	26
1.5.2 Muon-induced backgrounds	27
1.5.3 Radioactivity	29
1.5.4 Shielding background particles	36
2 Muon simulations	41
2.1 Muon simulations for carbon storage sites	41
2.1.1 Conceptual overview	41
2.1.2 Muons at the surface	44
2.1.3 Geometry construction	45
2.1.4 Code setup, validations and optimisations	50
2.1.5 Subsurface carbon dioxide distributions	54
2.1.6 Analysis and results	55

2.1.7	Muon detection efficiency	58
2.1.8	Discussion	60
2.2	Muon simulations for underground laboratories	64
2.2.1	Underground muon spectrum at SURF	65
2.2.2	Muon generator for the LZ simulation software	66
2.2.3	Validations	69
2.2.4	Transport of muons through the detector geometry	71
2.2.5	Adding cavern rock to the simulation geometry	74
2.2.6	LZ detection principles	74
2.2.7	WIMP signals in LZ	83
2.2.8	Post-processing and analysis	83
2.2.9	Muon-induced background rate	85
3	Simulations of background radiations	91
3.1	Radioactive decay event generator	91
3.1.1	Simulations of radioactive backgrounds	91
3.1.2	Radioactive decay in Geant4	93
3.1.3	Radioactive decay generator - ‘G4Decay’	94
3.2	Radioactive backgrounds for borehole detectors	100
3.2.1	Simulation setup	100
3.2.2	Background events in the detector	104
3.2.3	Evaluating trigger conditions	108
3.3	Radioactive backgrounds for underground experiments	111
3.3.1	Gammas from rock	112
3.3.2	CPU requirements	113
3.3.3	Event biasing scheme	115
3.3.4	Geometry construction	118
3.3.5	Analysis and results	118
3.3.6	Neutrons from rock	122
3.3.7	Spectra of neutrons from rock	126
3.3.8	Simulation, processing and final rate	126
	References	135

List of figures

1.1	The typical formation of a carbon storage site. Supercritical CO ₂ is injected via a pipeline into a permeable rock layer that is situated below an impermeable ‘cap rock’ layer.	3
1.2	The predicted contribution of each mechanism to the overall trapping of CO ₂ in a typical storage reservoir [1].	5
1.3	Seismic snapshots showing the presence of CO ₂ in the Utsira sandstone formation at Sleipner field [2]. The three plots in the upper panel show a cross-section of the reservoir from seismic surveys undertaken in 1994 (before injection), 1999 and 2001. The <i>y</i> -axis shows ‘two-way-time’ (TWT) - the time it takes for the seismic signal to propagate through the subsurface and back to the seismometer - and the colour scale shows seismic amplitude, with the red/yellow areas denoting a negative reflection coefficient caused by the presence of CO ₂ . The bottom panel shows the lateral extent of the plume from the same three seismic surveys. In these three plots, the colour scale shows the integrated reflection amplitudes in a TWT window from 0.84 to 1.08 s. The blue regions correspond to low reflectivity and the red regions correspond to high reflectivity.	7
1.4	The operating principle of a zero-length spring. A change in gravity, δg , causes the mass M to move from the horizontal, but all moment forces remain balanced and the system is in equilibrium for different values of θ . During operation, a second spring is used to bring the mass M back to the horizontal and provide a measurement of δg . Figure adapted from [3].	9
1.5	The difference in gravimetry measurements between a survey of 30 benchmark points taken in 2002 and 2005 [4]. The outline of the CO ₂ plume is based on seismic data.	10

1.6	InSAR map showing the ‘range velocity’ - the rate of change in the distance from a point on the surface of the Earth to a fixed reference point in space - in the vicinity of the In Salah storage site [5]. Three injection wells (KB-501, KB-502 and KB-503) are superimposed onto the image. The effect of surface uplift, signified by negative range velocities, around the injection wells indicates the presence of CO ₂ in these regions.	12
1.7	Measured energy spectra of individual components of the primary cosmic ray spectrum [6].	14
1.8	Diagram showing the interaction of a primary cosmic ray with nuclei in the Earth’s upper atmosphere and the production of secondary cosmic rays in the form of muons, neutrinos, electromagnetic showers and hadronic cascades [7].	16
1.9	The spectrum of muons at the surface of the Earth measured at two angles from the vertical, $\theta=0^\circ$ and $\theta=75^\circ$, as shown in [6].	18
1.10	The stopping power of muons on copper, adapted from [6]. E_μ^c is the critical energy of muons, which is defined as the energy at which losses by ionisation and radiative processes are equal.	21
1.11	The depth-vertical muon intensity relation for standard rock and water (solid and dashed lines) as calculated using the MUSIC simulation code [8]. The data points for rock (filled triangles) are taken from from a collection of experiments [9]. The data points for water are taken from the Baikal [10] (open circles) and AMANDA [11] (filled circles) experiments.	23
1.12	The energy spectra of 2 TeV muons transported through 3 km of water using MUSIC (solid curve), Geant4 (dashed curve) and FLUKA (dotted curve) [8].	24
1.13	Vertical muon intensity as a function of depth (1 km w. e. = 10^5 g cm ⁻² of standard rock) [6]. The shaded area at depths > 15 km w. e. is due to neutrino-induced muons and the darker shading shows the muon flux measured by the Super-Kamiokande experiment. The insert shows vertical muon intensity vs depth for water and ice.	27
1.14	The ²³⁸ U decay chain. Figure taken from [12].	30

1.15	The activity of radioisotopes on the ^{238}U decay chain as a function of time assuming only ^{238}U nuclei are present at $t = 0$. In the top plot, ^{234}Th and $^{234\text{m}}\text{Pa}$, which immediately follow ^{238}U in the decay chain, are shown. In the bottom plot, significantly longer times are represented (note the different scale on the x -axis) for ^{234}U and ^{230}Th	34
1.16	The activity of radioisotopes on the ^{238}U decay chain as a function of time, assuming that the chain is in equilibrium at $t = 0$, under two conditions; (a) the removal of 50% of the nuclei of ^{222}Rn (top plot) and (b) the removal of 50% of the nuclei of a long-lived isotope ^{226}Ra (bottom plot).	35
1.17	Total photon cross sections for two targets (carbon and lead) as a function of energy [6]. The contributions of the following processes are shown: $\sigma_{\text{p.e.}}$ = photoelectric effect, σ_{Rayleigh} = Rayleigh (coherent) scattering, σ_{Compton} = incoherent Compton scattering off an electron, κ_{nuc} = pair production (nuclear field), κ_{e} = pair production (electron field), $\sigma_{\text{g.d.r}}$ = photonuclear interactions (Giant Dipole Resonance). . .	38
1.18	The range of electrons in xenon, argon and germanium as a function of incident energy calculated using data obtained from [13].	40
2.1	A sketch of the arrangement of muon detectors for monitoring CO_2 storage in an underground formation. Muons are detected beneath the injection region, using detectors that fit inside boreholes. In this representation, the detectors will be placed inside sidetracks that are drilled from a mother bore, as shown in the insert. The arrangement is similar for both on-shore and off-shore sites.	42
2.2	Left - the 20% CFD time difference as a function of distance along the bar. Each point represents the mean of 1000 events, and the green and yellow bands represent the 1σ and 2σ Gaussian deviations from this value. Right - the 20% CFD time difference and the fractional difference in signal amplitudes for each position along the bar. Each data point represents a single muon event, and the corresponding sigma contours for each cluster are overlaid. Both figures have been taken from [14]. . .	44
2.3	The energy of muons sampled with zenith angles $65^\circ < \theta < 70^\circ$ and energy $160 \text{ GeV} < E < 1 \text{ TeV}$ (blue) and the analytical distribution obtained using Eq. (1.6) (red). This provides a validation of the Monte Carlo code for sampling muons at the surface.	46

2.4	The $\cos(\theta)$ distribution of sampled muons (blue), where θ represents the zenith angle of muons, normalised to the vertical ($\theta = 0$) intensity. The red line shows a $\cos^2(\theta)$ distribution for comparison.	46
2.5	A map of the United Kingdom showing the location of the Boulby Mine on the North East coast of England.	47
2.6	A 2D drawing of the geological repository showing the bulk density values (before injection) of the rock layers. X marks the location of the detector site used in this study.	48
2.7	Left - a sketch of the corner-point grid geometry showing the definition of two cells, each with 8 corner points, defined according to 4 pillars and distances d_i along the pillars. Right - a representation of the triangular and quadrangular meshes used to describe irregular cells in the model.	49
2.8	A 3D drawing of the geological repository for use in Geant4 after converting the corner-point grid into triangular and quadrangular meshes.	49
2.9	The energy spectrum of 2 TeV muons transported through 3 km w. e. in standard rock ($Z = 11$, $A = 22$) using the Geant4 v.9.6 (blue) and MUSIC (red) computer codes.	51
2.10	The displacement along the x -axis of 2 TeV muons transported through 3 km w. e. in standard rock ($Z = 11$, $A = 22$) using the GEANT v.9.6 (blue) and MUSIC (red) computer codes.	51
2.11	The distribution of $ r_{det} - r_{proj} $ describing the displacement of muons measured with a radial position, r_{det} , from their projected radial position at the detector site, r_{proj} (calculated based on the muon trajectory at sea level) [15].	52
2.12	A quarter-symmetric rendering of the density profile of the injection region predicted after 64 days [15]. The output from the numerical model is shown in (a) and the corresponding voxelisation, which is overlaid onto the physical Geant4 geometry, is shown in (b). The injection point in both (a) and (b) is at the bottom of the dashed black line.	55

- 2.13 The change in muon count due to the constant injection of CO₂ parameterised as the significance factor, S . For the ‘extreme’ injection scenarios ~ 45 live days of statistics are shown and for the ‘nominal’ injection scenarios ~ 30 live days of statistics are shown. Each distribution shows S for muons detected with a zenith angle, θ (plotted radially) and azimuthal angle, ϕ (plotted anti-clockwise with $\phi = 0^\circ$ pointing to the right). In total there are 100 angular bins, with widths $\Delta\theta = 7^\circ$ and $\Delta\phi = 36^\circ$. A linear interpolation has been applied between adjacent bins. 59
- 2.14 The difference in total muon count, ΔN_μ between the ‘no-CO₂’, and ‘nominal-CO₂’, and ‘extreme-CO₂’ scenarios as a function of time since injection, T . The required values of ΔN_μ to achieve a 3σ , 4σ and 5σ value of S are also shown. 60
- 2.15 The change in muon count due to the constant injection of CO₂ parameterised as the significance factor, S . The caption for each contour plot shows the time interval since the start of CO₂ injection. Each distribution shows S for muons detected with a zenith angle, θ (plotted radially) and azimuthal angle, ϕ (plotted anti-clockwise starting from the right). In total there are 100 bins, with a bin width $\Delta\theta = 7^\circ$ and $\Delta\phi = 36^\circ$. A linear interpolation is made between adjacent bins. 61
- 2.16 The change in muon count due to the constant injection of CO₂ parameterised as the significance factor, S . The caption for each contour plot shows the time interval since the start of CO₂ injection. Each distribution shows S for muons detected with a zenith angle, θ (plotted radially) and azimuthal angle, ϕ (plotted anti-clockwise with $\phi = 0^\circ$ pointing to the right). In total there are 100 angular bins, with widths $\Delta\theta = 7^\circ$ and $\Delta\phi = 36^\circ$. A linear interpolation has been applied between adjacent bins. 62
- 2.17 The arrangement of bars inside the borehole container that are considered for the efficiency calculations. The ‘loose’ packing (left) comprises 16 bars and the ‘tight’ packing (right) comprises 24 bars. 63
- 2.18 The acceptance, A , of muons that are recorded over the detector region for different combinations of the detector fraction, F_{det} , and the number of bars per detector, N_{bar} . A is plotted as a function of the number of bars that are traversed by a muon, N_{bar}^{hit} 63

-
- 2.19 Top left - The muon azimuth angle ϕ distribution at the Davis campus integrated over θ . The vertical lines show 22.5° divisions for comparison with the surface altitude profile shown in in the top right. On this map, ϕ is defined counter clockwise with $\phi = 0$ at east (the direction pointing to the right). One can match, by eye, the peaks in the azimuth angle distribution with regions of low altitude in the surface map. Bottom - a satellite image of the region above the Davis cavern. The prominent feature on all three figures is the ‘open cut’, which appears as a blue region on the altitude map and as a peak in the azimuthal distribution at $\sim 170^\circ$ 67
- 2.20 The energy spectra of muons generated in LUXSim (left) and the stand-alone MUSUN code (right). The apparent discrepancy at low energies (< 10 GeV) is an effect of binning on the output from MUSUN, which writes energies to the nearest 100 MeV. 69
- 2.21 The distribution of azimuth angle ϕ for muons generated in LUXSim (left) and the stand-alone MUSUN code (right). This distribution takes into account a specific cavern configuration (see Section 2.2.4) and is therefore different from the distribution shown in Figure 2.19. 70
- 2.22 Direction cosines in the x -direction and y -direction of muons generated in LUXSim (left) and the stand-alone MUSUN code (right). 70
- 2.23 The x - y positions of the muons generated in LUXSim (left) and the stand-alone MUSUN code (right). Muons are sampled on the surface of a cuboid that sits outside the Davis cavern (see Section 2.2.4). The relative alignment of the cavern, LUXSim and geographical (North-South) coordinate systems are also shown. 71
- 2.24 The layout of the Davis cavern at SURF. The size of the cavern is approximately 20 m running north-south and 14 m running east-west. The height is approximately 12 m. Note that the cavern is rotated approximately 14 degrees east from the north-south direction. 73
- 2.25 The alignment of the geographical directions with respect to the cavern coordinate system and the simulation - labelled ‘LUXSim’ - coordinate system. A representation of the cavern walls is marked out in red. . . . 73
- 2.26 A visualisation of the simulation geometry showing a top-view (top figure) and a side-view (bottom figure) of the cavern rock (grey), the cavern space (yellow), the water tank (red) and the steel pyramid (green). 75

2.27	A representation of a particle interaction in the LZ TPC. An incoming particle produces prompt scintillation light ('S1') and ionisation electrons, which are drifted under the influence of an electric field to a gas region at the top of the TPC where they are extracted and undergo electroluminesce. The resulting photons are detected as a secondary pulse ('S2'). The time between these two signals indicates the depth of the event and the hit map on the top PMT array indicates the position in x - y . Figure adapted from [16].	78
2.28	A plot of LUX calibration sources showing the anti-correlation between the amount of charge ('S2/E') and light ('S1/E') produced for each recoil event [17]. The units of 'S1' and 'S2' are detected photons (phd).	79
2.29	A discrimination plot of electron recoils (blue) and nuclear recoils (yellow) from calibration data [18]. The large filled circles show the mean of a fitted Gaussian and the small filled circles show the $\pm 1\sigma$	80
2.30	The arrangement of the LZ detector systems. Figure adapted from [16].	82
2.31	Energy spectra of all 'electromagnetic' events in the forward-field region of the liquid xenon TPC for high energies (above) and intermediate energies (below). The broad peak in the top plot is due to energy depositions from muon ionisation as they traverse length of the detector. In the bottom plot, the peak at 511 keV is caused by energy depositions of γ -rays produced from annihilation.	87
2.32	Energy spectra of muon-induced events in the forward-field and reverse-field regions of the liquid xenon TPC. The top plot shows energy depositions from nuclear recoils only, including both pure events (involving just nuclear recoils) and mixed events (involving nuclear recoils and electromagnetic energy depositions due to pile-up). The bottom plot shows events made up of energy depositions from both nuclear recoils and electron recoils. The spectra is shown for events surviving each of the analysis cuts described in Section 2.2.8	88
3.1	The event scheme for a ^{238}U decay chain using the default Geant4 setup. The event starts with the appearance of the parent isotope and terminates at the final stable daughter. The time of all tracks and steps are measured with respect to the appearance of the first isotope on the chain.	93

3.2	The event scheme for a ^{238}U decay chain using the <code>G4Decay</code> generator. The decay chain is split into sub-events which correspond to the individual decays of the radioactive isotopes in the chain. The time of the tracks and steps are measured with respect to the appearance of daughter particles produced by the radioactive decay at the start of each sub-event.	94
3.3	Flowchart showing the algorithm used in the <code>G4Decay</code> generator to split a decay chain into sub-events.	95
3.4	The β -decay of $^{234}\text{Th} \rightarrow ^{234\text{m}}\text{Pa}$. The energy levels of $^{234\text{m}}\text{Pa}$ are shown in black, as well as the energy (in blue) and intensity (in red) of each γ -ray from nuclear de-excitation. All excited states decay to the 73.92 keV energy level, from which there is a β -decay of $^{234\text{m}}\text{Pa}$ with a half-life of 1.16 minutes.	96
3.5	Number of occurrences of each radioisotope in each decay tree for the ^{238}U decay chain (top) and the ^{232}Th decay chain (bottom), based on $1 \cdot 10^5$ initial decays. In the top plot the occurrences of ^{214}Po are not shown because these events are automatically grouped with its parent isotope due to its short half-life. Similarly, in the bottom plot the occurrences of ^{212}Po are not shown.	98
3.6	Comparison of γ -lines generated in a Monte Carlo simulation of 10000 decays using the <code>G4DECAY</code> generator (blue histogram) and data from the NuDat database (red markers) for the ^{238}U decay chain (top) and the ^{232}Th decay chain (bottom).	99
3.7	The detector setup as constructed in the Geant4 framework. For clarity, only the ends of the rock cylinder (red) and the steel casing (pink) have been drawn. In total, there are 20 scintillator bars (grey, with yellow ends) each with a thickness of 2 cm and a length of 100 cm.	101
3.8	The fraction of detected events as a function of R , the distance from the center of the borehole detector.	103
3.9	Initial positions of events in the rock that contribute to the background rate in the borehole detector i.e. events that give an energy deposition in any of the scintillator bars.	103

3.10	Energy deposition in the scintillator bars for all events coming from ^{238}U decays in the rock. The distribution in the top plot shows the true energy deposits and the distribution in the bottom plot shows the energy deposits after the smearing is applied according to Eq. (3.8) with $\xi = 0.032$	105
3.11	Energy deposition in the scintillator bars for all events coming from ^{232}Th decays in the rock. The distribution in the top plot shows the true energy deposits and the distribution in the bottom plot shows the energy deposits after the smearing is applied according to Eq. (3.8) with $\xi = 0.032$. For an explanation of the features visible in the top figure, the reader is referred to the main text.	106
3.12	Energy-weighted positions of events in the scintillator bars from ^{232}Th decays (top) and ^{238}U decays (bottom). Note the different colour scales on the z axis. The overall rate is higher for ^{232}Th compared with ^{238}U	109
3.13	Rate of events as a function of the number of bars hit per event N_{bar}^{hit} for ^{238}U (top) and ^{232}Th (bottom). The distributions are shown for different energy thresholds E_{thres} ranging from 0 - 1000 keV. The rate of muons through the borehole detector, based on the simulations described in Section 2.1 is also shown.	110
3.14	Rate of events as a function of the number of bars hit per event N_{bar}^{hit} for both ^{238}U and ^{232}Th events combined. The distribution is shown for different energy thresholds E_{thres} ranging from 0 - 1000 keV. The rate of muons through the borehole detector, based on the simulations described in Section 2.1 is also shown.	111
3.15	The arrangement and dimensions of the LZ detector systems [19].	113
3.16	The simulated gamma flux emerging from the rock, normalised to the measured gamma lines from Table 3.2.	115
3.17	The arrangement of the LZ detector with the approximate positions of the three surfaces on which gammas are saved and boosted shown in orange [19].	117
3.18	Visualisation of the simulation geometry showing the cavern rock ‘shell’ (magenta), the cavern space (brown), the water tank (blue) and the steel pyramid (green).	118
3.19	Energy spectra of gammas, coming from ^{232}Th (top), ^{238}U (middle) and ^{40}K (bottom) decays, at the end of each stage of the simulation run.	120

3.20	Energy spectrum of events in the forward-field region of the TPC after 10^{15} ^{232}Th decays in the rock, before any cuts are applied (blue) and after all cuts are applied (red). Only events with $S1c$ (phd) > 0 and $S2$ (phd) > 450 are included.	121
3.21	Distribution of events coming from gammas from ^{232}Th decays in the rock. The top plot shows all events depositing < 150 keV_{ee} , and the bottom plot shows events surviving all analysis cuts and depositing < 150 keV_{ee} . In both plots, only events occurring in the forward-field region of the TPC ($z > 0$) are shown. The dashed line represents the fiducial volume.	123
3.22	Diagram of the LZ detector highlighting the tubes/pipes/conduits that connect the inner detector with the laboratory [19]. Three vertical calibration delivery tubes and one horizontal neutron calibration tube on the opposite side of the detector are not shown.	124
3.23	Spectra of neutrons from the cavern rock due to spontaneous fission and (α,n) reactions from ^{232}Th and ^{238}U decays. The spectra have been normalised assuming an activity of 1 mBq/kg.	127
3.24	Estimated background rates for the LZ experiment, parameterised as the number counts in 1000 days for a 5.6 ton fiducial volume [16]. . . .	129

List of tables

1.1	Carbon storage monitoring techniques that have been used at three CCS demonstration projects (used = ●, not used = ○) [20].	13
1.2	The depth and measured muon flux at several underground laboratories. The references for the muon flux measurements are stated individually for each entry in the table. The depth information is taken from [21].	28
2.1	Muon intensities and mean energies at a depth of 2 km w. e. for ‘standard rock’ using the Geant4 and MUSIC codes. The difference between the muon fluxes is due to different detector configurations - MUSIC records muons on a spherical surface whereas the Geant4 simulations use a flat surface.	53
2.2	The global muon intensity at the detector region for different bulk density values of the sandstone storage layer.	57
2.3	The muon flux, ψ_μ , at various time intervals T since injection and the associated significance S of the change in ψ_μ relative to the pre-injection scenario. The error values are statistical uncertainties in the muon count.	58
2.4	Composition of the rock in the Davis Cavern according to [22].	74
2.5	The abundances of isotopes of natural gadolinium and the thermal neutron capture cross-section for Gd(n, γ) according to [23].	82
2.6	Number of events surviving after each analysis cut for 2.3×10^8 muon events.	89
3.1	Branching ratios of isotopes on the ^{238}U and ^{232}Th decay chains whose parent isotopes decay by two modes.	100
3.2	Intensities of the highest energy gamma lines from the ^{238}U and ^{232}Th decay chains and the ^{40}K single decay as measured by a HPGe detector in the Davis cavern [24].	114

3.3	Activity, concentration and number of gammas in 1000 days coming from the Davis cavern for each radioisotope. These values are calculated from the gamma spectrum shown in Figure 3.16, which is based on measurements made in [24].	114
3.4	Simulated live time and background rates coming from the decays of ^{40}K , ^{238}U and ^{232}Th in the cavern rock.	122
3.5	Summary of the conduits/pipes that connect the inner detector to the outside of the water tank (see 3.22) and the corresponding ‘ ω -value’. The bottom conduit will allow the passage of the most neutrons from the rock based on this metric.	125

Chapter 1

Geological carbon storage, cosmic rays and background radiations

1.1 Carbon capture and storage

The rise of atmospheric concentrations of greenhouse gases, such as carbon dioxide (CO₂), is triggering changes in the world's climate and increasing the likelihood of extreme weather events [25]. While the use of renewable energy sources is on the rise, most scenarios for economic development predict an increase in fossil fuel usage and consequently CO₂ emissions to the atmosphere [26]. A promising technological solution to stabilise CO₂ levels and mitigate the risks of anthropogenic climate change is the use of carbon capture and storage (CCS). Carbon capture technologies comprise methods to isolate a nearly pure stream of CO₂ from waste gases that are commonly produced in large quantities at point sources such as large-scale fossil fuel or biomass energy facilities. Existing carbon capture technologies are capable of removing 85-95% of the CO₂ contained in waste gas products [27, 1]. This CO₂ may be sold for use in other industries, but storage in an underground geological formation is the best option for significant reductions in carbon emissions.

In the early 1990s, geologists suggested that sedimentary basins could be suitable for this type of long-term storage [28, 29]. These formations typically consist of alternating layers of coarse and fine-textured sediments. The coarse layers, formed mostly of sandstone, are permeable and so provide a reservoir in which to store CO₂. The impermeable fine-textured layers, formed mostly of clay, shale, or evaporites, form an overlying seal that prevents the upward migration of CO₂ and leakage to the surface.

Two types of sedimentary basins, saline aquifers and depleted oil or gas formations, have been identified as good candidates for permanent geological storage. Saline

aquifers are porous rock formations that are already saturated with non-potable water, usually brackish water or brine (salt water). The first industrial-scale carbon storage project, which started operations in 1996 at Sleipner Field near Norway, involves CO₂ injection into a saline formation [30]. Natural gas extracted from the nearby ‘Sleipner East Field’ has CO₂ concentrations of up to 9%, which exceeds export requirements. The excess CO₂ is removed from the hydrocarbons at an offshore platform and pumped underground into a saline reservoir known as the ‘Utsira’ formation for geological storage. Figure 1.1 shows the various production and injection wells at Sleipner Field, where ~ 2700 tonnes of CO₂ is injected each day. The setup depicted in this diagram is representative of operations at other storage sites, both onshore and offshore, although it is possible for projects to operate using CO₂ that is transported over large distances (hundreds of kilometers) from its point of production before being injected underground.

The technologies involved in transport and injection are well-established in the hydrocarbon industry. In fact, the practice of pumping CO₂ underground to extract more oil has been taking place since the early 1970s. Not only does the injection increase the pressure of the reservoir, allowing more oil to be extracted, but the CO₂ mixes with the oil liberating it from traps in the subsurface. Today, around 20 Mt/year of CO₂ is injected into over 50 oil fields in Texas, USA for the purposes of enhanced oil recovery (EOR) [31]. A research project has been established at Weyburn field in Canada that combines EOR with long-term carbon sequestration [32]. The CO₂ is produced at a coal gasification and coal power station located in North Dakota, USA and is transported over 330 km via an onshore pipeline. Depleted oil formations are an economically attractive option for CCS, in part because of the prospect of enhanced oil recovery (EOR), but also because the formations have been well studied during previous explorations and the integrity of the cap rock is well established. This is also true for depleted gas formations. In Algeria, over 3.8 Mt of CO₂ produced from a gas processing facility at the In Salah oil field has been stored in a former gas reservoir [33]. Injection was suspended in 2011 due to concerns about the integrity of the rock seal, although no leakage was reported over the lifetime of the project. This highlights the importance of storage monitoring, which will be discussed in more detail in Section 1.1.2.

The world-wide storage capacity of CO₂ has been investigated by different groups of geologists. Early research, based on the volumetric capacity of underground formations, suggested that hundreds of years worth of global CO₂ emissions could be stored [1]. In addition, the potential to store it over geological time periods is proven by naturally occurring CO₂ reservoirs, which exist in various places throughout the world. In

Mississippi, USA, ~ 200 Mt of CO_2 has been trapped in a formation known as the Pisgah Anticline for some 65 million years with no evidence of leakage [34]. There are, however, different challenges associated with engineered sites. The main concerns are related to pressure increases after CO_2 is injected into the subsurface. This may limit the storage potential of some sites, since fractures or faults in the overlying cap rock may be created or reactivated. Storage sites are often classified as being either an ‘open formation’ - where the pressure can dissipate laterally - or a ‘closed formation’ - where pressure builds and there is a risk that CO_2 may leak if injection continues. Monitoring the CO_2 migration after injection can help to characterise a formation and determine whether or not the storage capacity has been reached. Based on these considerations, the actual world-wide capacity for geological carbon storage, while still large, may be less than previously thought [35, 36].

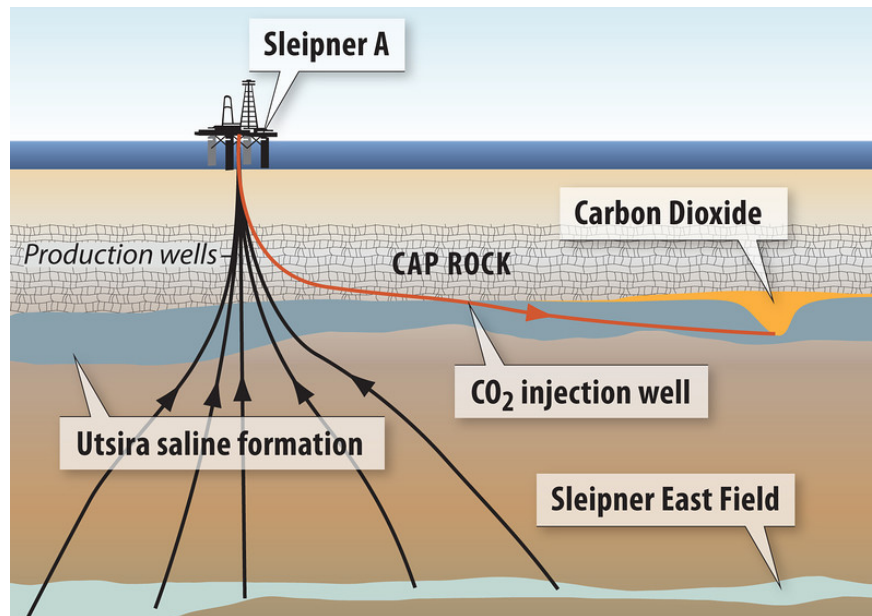


Figure 1.1: The typical formation of a carbon storage site. Supercritical CO_2 is injected via a pipeline into a permeable rock layer that is situated below an impermeable ‘cap rock’ layer.

1.1.1 Storage and trapping

For long-term geological storage, the injection of CO_2 should be at a depth $\gtrsim 800$ m so that there is sufficient temperature and pressure to maintain the CO_2 at or above the critical point. In this regime, the CO_2 is a supercritical fluid, meaning it expands to fill a volume like a gas but has the density of a fluid. This is advantageous for carbon

storage, since more CO₂ can be sequestered in a given volume than if CO₂ remained a gas. Once injected, the carbon remains trapped via four mechanisms:

- **Structural trapping**

This dominates during the early phases after injection and occurs when an immiscible phase of CO₂, which is less dense than the surrounding fluids, migrates upwards under buoyancy forces and is trapped by the impermeable ‘cap rock’ layer that overlays the storage region.

- **Residual trapping**

As the CO₂ plume moves through the rock, small parts become disconnected inside the rock pores. As the rest of the plume continues to migrate, the formation fluids that were originally displaced fill in the rest of the pore space, trapping disconnected ‘bubbles’ of CO₂.

- **Solubility trapping**

This form of trapping refers to the dissolution of the CO₂ in the surrounding brine (salt water). The resulting mixture is denser than the surrounding formation fluids, causing it to sink towards the bottom of the reservoir.

- **Mineral trapping**

This is the final phase of trapping. CO₂ that is dissolved in the brine slowly reacts with minerals in the sandstone layer forming stable, carbonate materials which are permanently bound to the rock.

The fate of CO₂ after injection is dependent upon the physical and chemical conditions of the storage site [37]. The rate of solubility trapping, for example, depends on the proportion of the CO₂ that dissolves in the water, which is sensitive to the temperature, pressure, composition of the formation fluids, injection rate, and the overall surface area of the CO₂-water interaction. Figure 1.2 shows a prediction of the relative contribution of each trapping mechanism as a function of time since first injection. It is clear that shortly after CO₂ is introduced into a storage reservoir the mobility of the CO₂, and therefore the potential for leakage, is highest. Monitoring of the CO₂ distribution during these times is essential to ensure the security of the storage.

1.1.2 Monitoring techniques

While CCS has been demonstrated at a number of sites throughout the world, there are still some technological issues that should be addressed. In particular, there is a demand

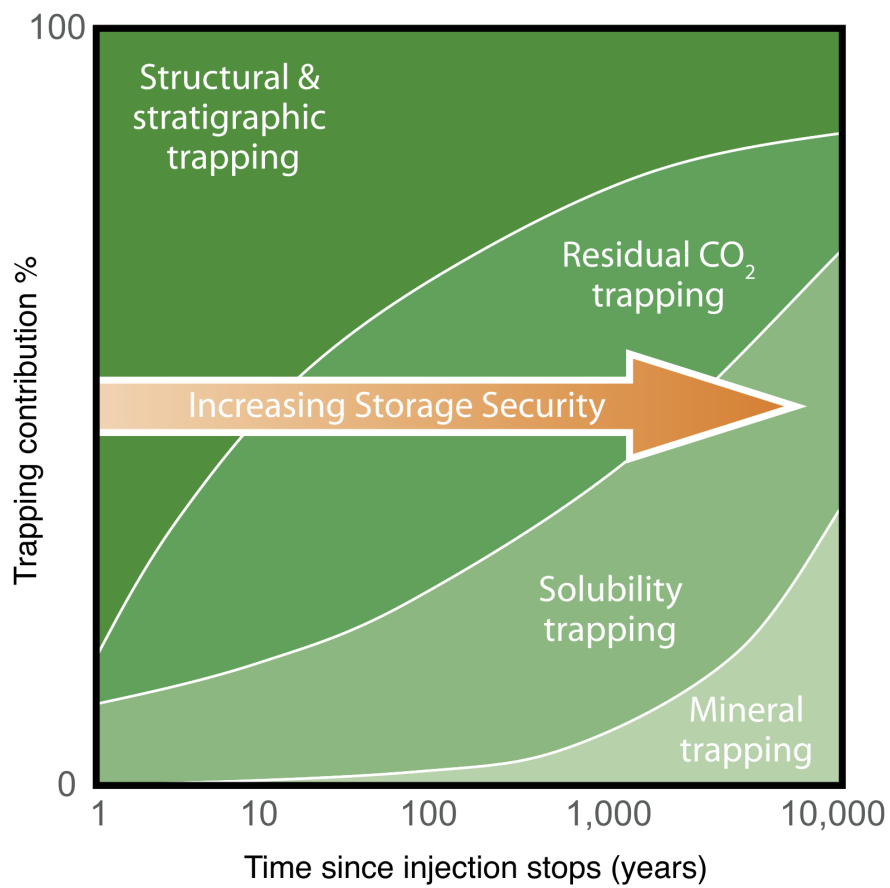


Figure 1.2: The predicted contribution of each mechanism to the overall trapping of CO₂ in a typical storage reservoir [1].

for a continuous, passive and cheap method of monitoring the CO₂ emplacement after its injection. This is important as a means of demonstrating that the subsurface CO₂ is effectively contained in the formation it was injected into. It is particularly important during the early phases of storage, since migration of the subsurface CO₂ is more volatile and its movement may be unpredictable. The following subsections will discuss existing monitoring methodologies in the context of CCS sites that are currently operating or have recently finished.

Seismic surveys

A seismic survey uses a controlled source of seismic energy, such as a small explosion or pressure released from an air-gun, to illuminate subsurface structures, typically with downward propagating waves. The reflected signal is then detected by clusters of geophones at the surface and interpreted as a spatial image. A geophone consists of a spring mounted magnet which moves in a magnetic coil attached to the fixed frame of the instrument. The relative motion provides a small voltage and current which constitutes the detected signal [38]. An extensive program of seismic monitoring has been taking place at Sleipner field since 1994 [39, 2, 4, 30]. At this site, CO₂ has been injected at a depth of ~ 1 km below sea level at the base of a sandstone reservoir which is $\gtrsim 200$ m thick. To interpret seismic signals, the acoustic properties of the reservoir are calculated based on the physical properties of the rock. This data typically comes from well logs - direct measurements of the subsurface, which is accessed using a vertically drilled borehole. The important parameters to obtain include the reflection coefficients of CO₂-saturated rock and water-saturated rock as well as the speed of the seismic waves and acoustic impedance through the sandstone storage layer as a function of CO₂ saturation. These can be calculated using the Gassmann equations [40], and indeed this is the procedure that was followed to interpret seismic data from Sleipner field [2]. Figure 1.3 shows the effect of the CO₂ subsurface distribution on the seismic signal at Sleipner field. The three figures in the upper panel show a cross-section of the reservoir from surveys undertaken before injection (1994) and then at two subsequent times post-injection. The y -axis shows ‘two-way-time’ - the time it takes for the seismic signal to propagate through the subsurface and back to the seismometer. The red and yellow areas represent changes in seismic amplitudes, which indicate the presence of individual CO₂ accumulations trapped beneath thin (~ 10 m) layers of impermeable shale rock. The thin region labelled as ‘C’ that runs from the top to the base of the sandstone is the CO₂ injection pipe and the black dot represents the injection point. After injection, the CO₂ plume is clearly visible and is driven upwards by buoyancy

forces until it reaches the shale cap rock layer at the time of 1999 survey and continues to migrate laterally. Recent studies indicate that total plume area, which continues to grow, reached 3.1 km² by 2008 [30].

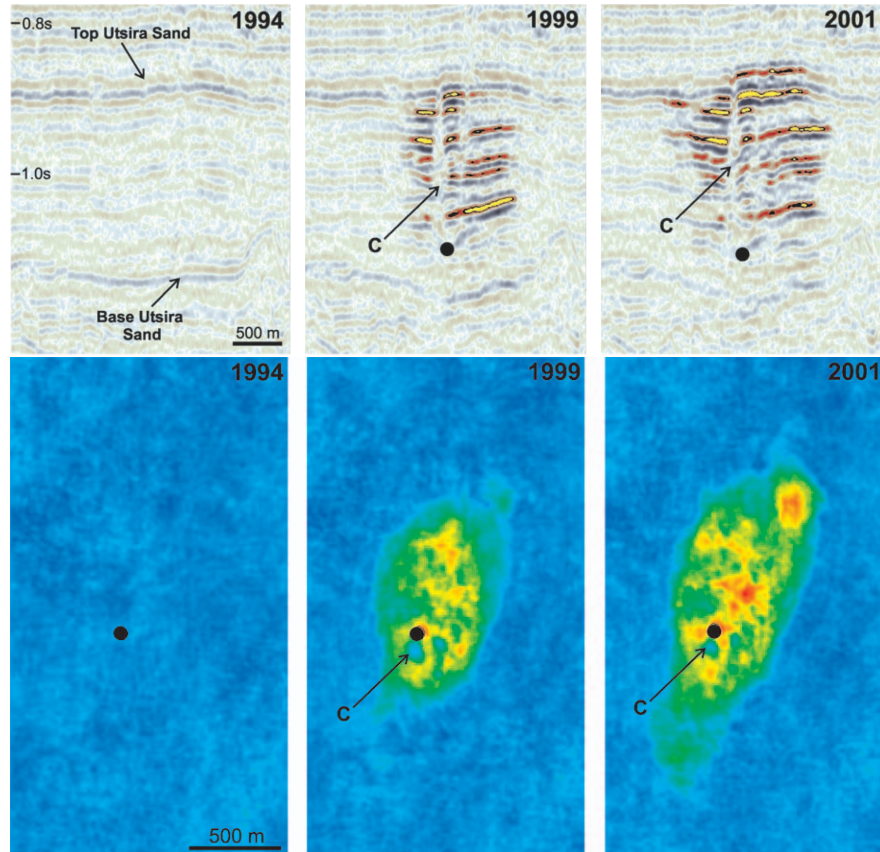


Figure 1.3: Seismic snapshots showing the presence of CO₂ in the Utsira sandstone formation at Sleipner field [2]. The three plots in the upper panel show a cross-section of the reservoir from seismic surveys undertaken in 1994 (before injection), 1999 and 2001. The y -axis shows ‘two-way-time’ (TWT) - the time it takes for the seismic signal to propagate through the subsurface and back to the seismometer - and the colour scale shows seismic amplitude, with the red/yellow areas denoting a negative reflection coefficient caused by the presence of CO₂. The bottom panel shows the lateral extent of the plume from the same three seismic surveys. In these three plots, the colour scale shows the integrated reflection amplitudes in a TWT window from 0.84 to 1.08 s. The blue regions correspond to low reflectivity and the red regions correspond to high reflectivity.

Gravimetry

The distribution of CO₂ in a storage reservoir can also be established using gravimetry. This technique measures changes in the Earth’s gravitational field, which are caused by

variations in the mass distribution of the subsurface. Gravimetric surveys have been carried out at Sleipner field using land-based gravimeters that were specially adapted to take measurements from the sea-bed [4, 41, 42]. Three surveys were taken in 2002, 2005 and 2009 at fixed locations above the storage region.

The gravimeters used in the surveys measure a piezoelectric signal that is induced by the small displacement of a mass attached to a zero-length spring housed inside a portable detector. The zero-length spring has a restoring force at all non-zero lengths, i.e. if all external forces are removed, the spring would collapse to zero length. If a mass is suspended in the horizontal position, as shown in Figure 1.4, the moment forces due to the mass and the restoring force of the spring are equal and opposite for all values of θ . During operation, a second spring is used to restore the beam to a horizontal position, which constitutes the measured signal. The technique allows a relative measurement of gravity on a resolution of a few μGal ($1 \text{ Gal} = 10^{-2} \text{ m s}^{-2}$). Figure 1.5 shows the difference in local gravity at 30 benchmark points between two surveys carried out in 2002 and 2005. The changes in gravity are attributed to three sources; (i) the displacement of fluids by less dense supercritical CO_2 that has been injected into the Utsira formation, which is the signal of interest, (ii) water flow and hydrocarbon production in the deeper lying gas reservoir and (iii) vertical depth changes of the seafloor caused by sediment removal. The effect of (ii) on the gravity measurements is quantified using reservoir simulations and data from hydrocarbon gas production wells and (iii) is filtered out using high-precision measurements of the sea-floor displacement between each survey.

Using gravimetry data from the three surveys, and the geometry of the CO_2 plume based on seismic data, the density of the region that the plume occupies in the reservoir is $\rho_{\text{plume}} = 720 \pm 80 \text{ kg m}^{-3}$ [42]. If no CO_2 has dissolved in the formation fluids, the plume comprises solely immiscible CO_2 that has displaced other formation fluids. In this scenario the density of the in-situ CO_2 $\rho_{\text{CO}_2} = \rho_{\text{plume}}$. However, if a fraction α of CO_2 has dissolved into the existing reservoir brine, the density of the plume region can be expressed as:

$$\rho_{\text{plume}} = \rho_{\text{CO}_2} / (1 - \alpha) \quad (1.1)$$

Based on measurements of the temperature and pressure of the storage formation and the CO_2 at the point of injection, the average density of CO_2 in the Utsira formation has been calculated as $\rho_{\text{CO}_2} = 675 \pm 20 \text{ kg m}^{-3}$. Then, a limit on the fraction of CO_2 that has dissolved into the reservoir can be calculated using the simple relationship

between ρ_{plume} and ρ_{CO_2} from Eq. (1.1). Using a maximum value of $\rho_{\text{plume}} = 800 \text{ kg m}^{-3}$ and a minimum value of $\rho_{\text{CO}_2} = 655 \text{ kg m}^{-3}$ gives an upper bound of $\alpha < 18\%$.

Although the calculation above discusses the specific case of Sleipner field, data from gravimetric surveys at any site can, in principle, be used to make similar determinations. This highlights the complimentary of multiple monitoring methods for monitoring carbon storage projects. The dissolution of CO_2 results in an acoustically homogenous subsurface that does not cause a seismic reflection, and is therefore invisible to seismic surveys. However, seismic data in combination with gravimetric surveys allows a constraint on the dissolved fraction of CO_2 and its rate of change to be calculated.

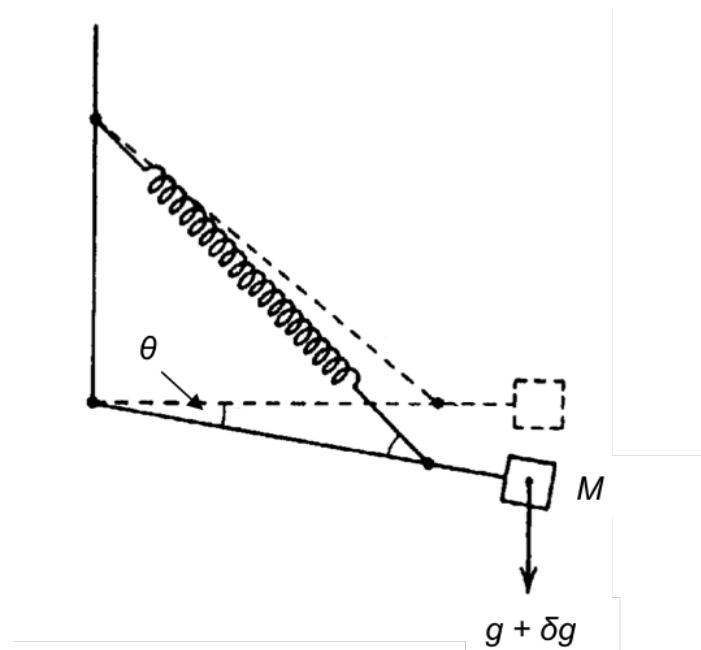


Figure 1.4: The operating principle of a zero-length spring. A change in gravity, δg , causes the mass M to move from the horizontal, but all moment forces remain balanced and the system is in equilibrium for different values of θ . During operation, a second spring is used to bring the mass M back to the horizontal and provide a measurement of δg . Figure adapted from [3].

InSAR

InSAR (Interferometric Synthetic Aperture Radar) is an imaging technique that maps the surface displacements caused by the injection of fluids (CO_2) into the subsurface. SAR data is obtained using successive pulses of radio waves that illuminate a target scene. The reflected pulses are recorded by a moving antenna, usually on board an aircraft or satellite, and signal processing techniques are used to combine the readings

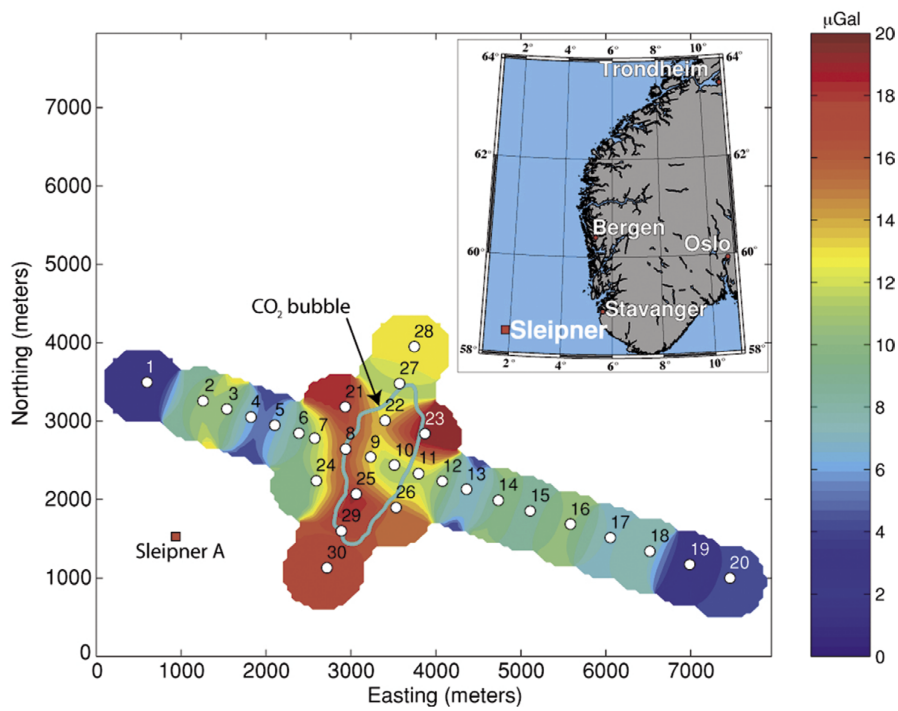


Figure 1.5: The difference in gravimetry measurements between a survey of 30 benchmark points taken in 2002 and 2005 [4]. The outline of the CO₂ plume is based on seismic data.

from multiple antenna locations. The use of InSAR for monitoring CO₂ injection was pioneered at the In Salah storage project in Algeria. Radar images from the European Space Agency of two satellite paths passing over the In Salah site were used. The data consists of 25 M pixels that cover an area of 100 km × 100 km above the storage site. In the analysis, which is presented in [5], the radar signal is used to identify so-called permanent scatterers (PS), a subset of the pixels that return stable reflections over a large sample of images. This allows corrections to be made to the data for atmospheric and orbital effects. Subsequently, the changes in distance between a fixed reference point in space and the PS - the *range change* - can be computed. A time series of radar images gives the *range velocity* for each PS, which is shown in Figure 1.6. The location of three injection wells, which are labelled as KB-501, KB-502 and KB-503, are superimposed onto the map. There are clear decreases in the range velocity in the vicinity of the wells, which correspond to surface uplift caused by the presence of CO₂ deep underground.

Other techniques

Table 1.1 shows a list of monitoring methods that have been employed at the three demonstration projects discussed above: Sleipner, In Salah and Weyburn field. 3D seismic, gravimetry and InSAR have already been discussed in detail. The following list provides an overview of the other monitoring techniques:

- **Micro-seismic**

The detection principles involved in micro-seismic surveys are similar to large surveys, but are undertaken over a smaller area. The source and receiver may be placed underground, such that measurements are taken across wells that are physically drilled through the storage region. Passive surveys, in which geophones measure micro-earthquakes induced by movements of CO₂ in the subsurface, are also possible.

- **Electromagnetic surveys**

These surveys rely on the change in resistivity of the subsurface due to the presence of CO₂, which has a lower conductivity than other formation fluids, such as brine, that it displaces in the reservoir.

- **Geochemical sampling**

By collecting fluid samples from boreholes within the storage region, the presence of CO₂ can be inferred from changes in pH or the concentrations of certain minerals such as carbonates and silicates.

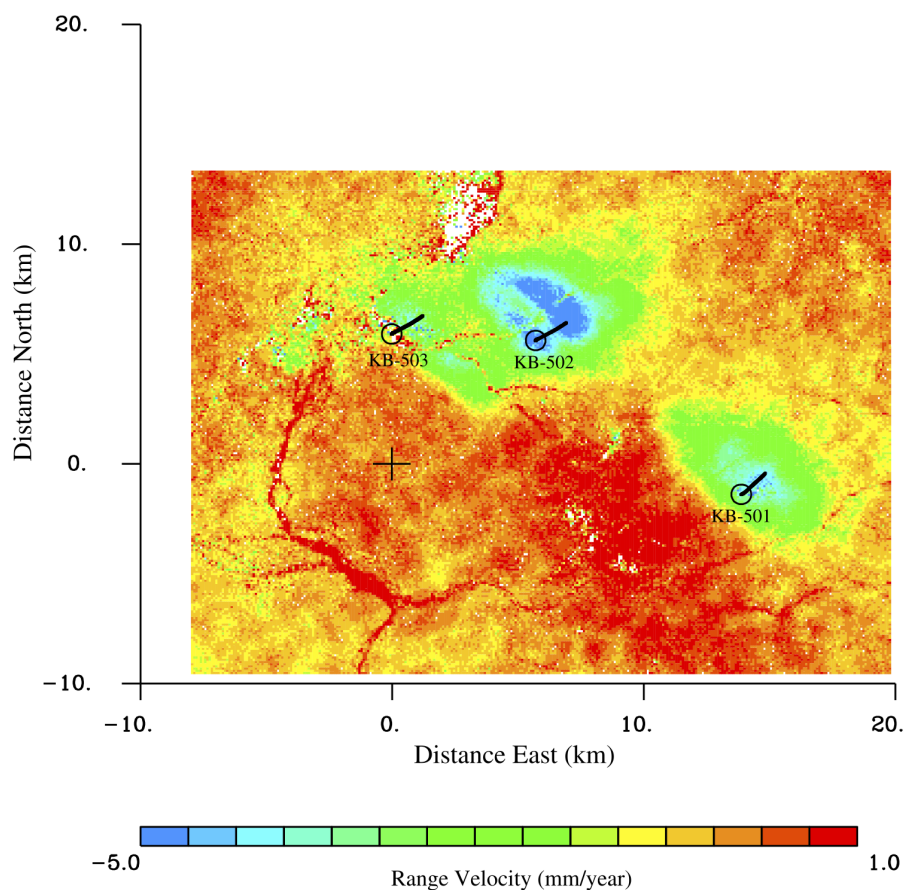


Figure 1.6: InSAR map showing the ‘range velocity’ - the rate of change in the distance from a point on the surface of the Earth to a fixed reference point in space - in the vicinity of the In Salah storage site [5]. Three injection wells (KB-501, KB-502 and KB-503) are superimposed onto the image. The effect of surface uplift, signified by negative range velocities, around the injection wells indicates the presence of CO₂ in these regions.

Table 1.1: Carbon storage monitoring techniques that have been used at three CCS demonstration projects (used = ●, not used = ○) [20].

Monitoring method	Sleipner	In Salah	Weyburn
3D seismic	●	●	●
Micro-seismic	●	○	●
Gravimetry	●	●	●
Electromagnetic surveys	○	●	○
Geochemical sampling	○	○	●
Soil-gas	○	●	●
Tracers	○	●	○
Core sampling	○	○	●
InSAR	○	●	○

- **Soil-gas**

For storage repositories based on-shore, the monitoring of soil gas can provide evidence of leakage. The concentration of CO₂ before injection begins defines a baseline survey against which subsequent measurements are compared

- **Tracers**

Tracers - chemical compounds that can be easily detected, even in small quantities - are injected into the subsurface with the supercritical CO₂ to give a "fingerprint" of the passage of the mixture through monitoring wells.

1.2 Cosmic rays

The purpose of the work presented in this thesis is to investigate the feasibility of using cosmic-ray muons to monitor CO₂ storage in a geological formation. In this section the production of cosmic-ray muons will be described. This will provide a necessary introduction to the work presented in later sections of this thesis.

Primary cosmic radiation refers to particles with stellar origins that arrive at the top of the Earth's atmosphere from outside of the solar system. As observed at the top of atmosphere, these cosmic rays consist mostly of nuclei (98%) and electrons (2%). The majority of the nuclei are hydrogen (87%) and helium (12%), with the remaining 1% in the form of heavier elements [7]. The energy spectrum of primary cosmic rays follows a power law of the form:

$$\frac{dN}{dE} \sim E^{-\gamma} \quad (1.2)$$

with the spectral index $\gamma \simeq 2.7$ for energies up to around 10^{15} eV. A compilation of measurements of the primary spectrum in this energy range is shown in Figure 1.7.

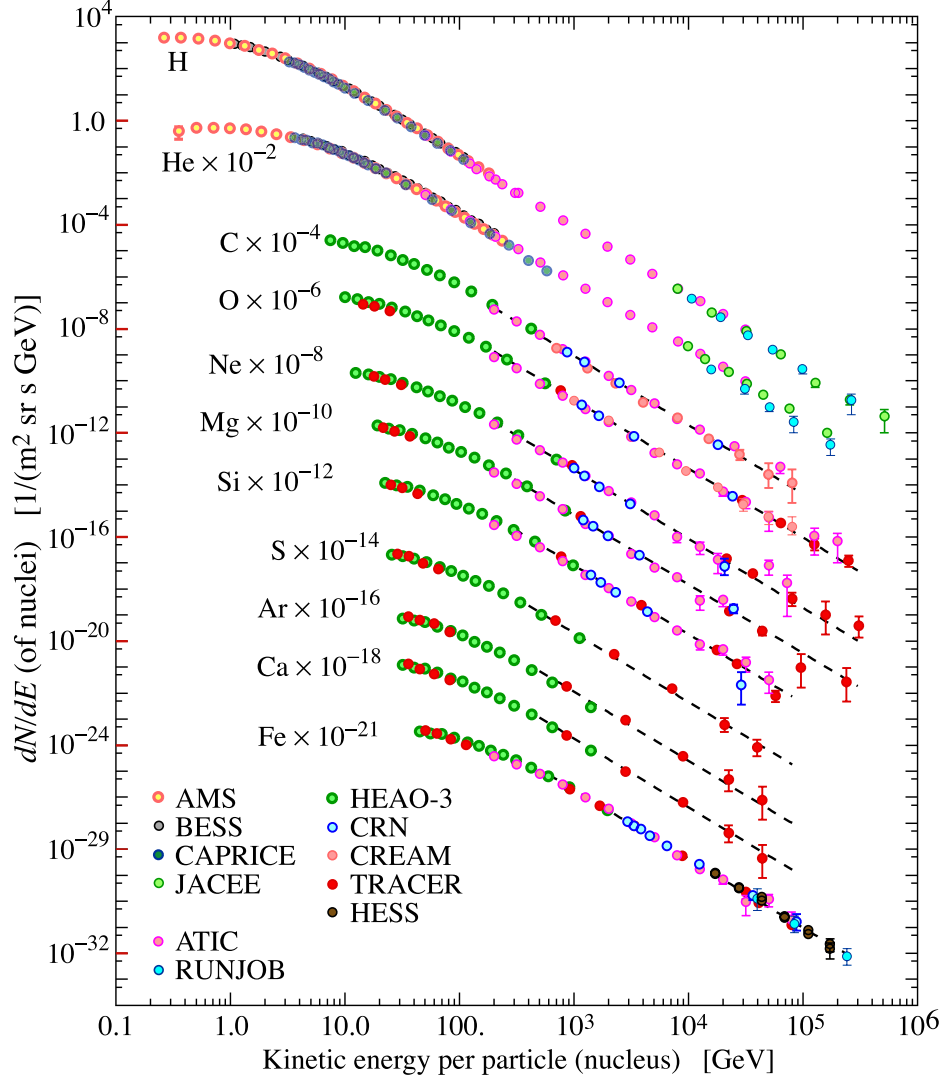


Figure 1.7: Measured energy spectra of individual components of the primary cosmic ray spectrum [6].

The interactions of primary cosmic rays with atmospheric nuclei produce a number of secondary particles. At high energies ($\gtrsim 10$ GeV), the de Broglie wavelength of a proton is much less than separation of nucleons inside atmospheric nuclei. Consequently, an incoming proton will interact with individual nucleons, producing neutral and charged mesons. The nucleons involved in the interaction may be expelled from the nucleus, resulting in an unstable excited state that ejects spallation fragments in the form of other nuclei, protons and/or neutrons. These products, as well as pions, kaons and

other mesons can then go on to induce further nuclear reactions in hadronic cascades. Pions have very short lifetimes, so as well as interacting in the atmosphere they will also decay. Neutral pions decay into two high energy gamma-rays ($\pi^0 \rightarrow 2\gamma$), which quickly convert into an electron-positron pair in the field of atmospheric nuclei ($\gamma \rightarrow e^- + e^+$). High-energy electrons and positrons emit photons via bremsstrahlung, and the two processes (pair production and bremsstrahlung) continue in succession to form an electromagnetic shower. Charged pions are also unstable, releasing muons as they decay:

$$\begin{aligned}\pi^+ &\rightarrow \mu^+ + \nu_\mu \\ \pi^- &\rightarrow \mu^- + \bar{\nu}_\mu\end{aligned}\tag{1.3}$$

There are analogous decays for other charged mesons such as kaons. At high energies $\gtrsim 10$ GeV, the Lorentz factor (γ) of muons is large and the resulting time dilation effect of special relativity enables them to reach the surface before they decay. Lower energy muons are likely to decay in-flight, producing electrons and positrons that can then go on to produce further low-energy electromagnetic showers:

$$\begin{aligned}\mu^+ &\rightarrow e^+ + \nu_e + \bar{\nu}_\mu \\ \mu^- &\rightarrow e^- + \bar{\nu}_e + \nu_\mu\end{aligned}\tag{1.4}$$

Figure 1.8 shows a diagram depicting the interaction of a primary cosmic ray in the atmosphere and the subsequent production of secondary cosmic ray particles.

1.2.1 Muons at the Earth's surface

The spectrum of primary cosmic rays follows a power-law, and consequently the spectrum of pions, kaons etc. also has this form. The muon spectrum is more complex, since the charged mesons will interact in the atmosphere, losing energy before they decay. In addition, most muons are produced high in the atmosphere, and will therefore undergo energy losses before reaching the Earth. A parameterisation proposed by Gaisser [43] gives an approximate formula for the muon spectrum at sea level:

$$\frac{dI_\mu}{dE_{\mu 0} d\Omega} \approx \frac{0.14 \times E_{\mu 0}^{-\gamma}}{\text{cm}^2 \cdot \text{s} \cdot \text{sr} \cdot \text{GeV}} \times \left\{ \frac{1}{1 + \frac{1.1E_{\mu 0} \cos \theta}{115\text{GeV}}} + \frac{0.054}{1 + \frac{1.1E_{\mu 0} \cos \theta}{850\text{GeV}}} \right\}\tag{1.5}$$

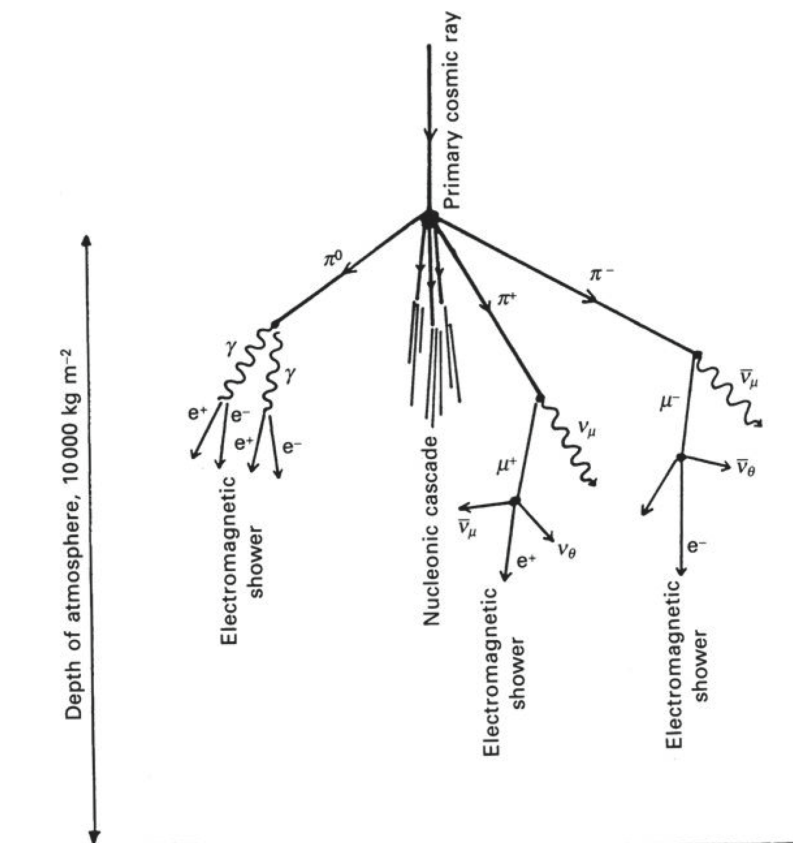


Figure 1.8: Diagram showing the interaction of a primary cosmic ray with nuclei in the Earth's upper atmosphere and the production of secondary cosmic rays in the form of muons, neutrinos, electromagnetic showers and hadronic cascades [7].

where $\frac{dI_\mu}{dE_{\mu 0}d\Omega}$ is the differential muon intensity at sea level, $E_{\mu 0}$ is the muon energy at the surface (in GeV) and θ is the muon zenith angle at the surface (valid for $\theta < 70^\circ$ where the curvature of the Earth can be neglected). Gaisser proposed a spectral index $\gamma = 2.7$ [43]. The first term inside the parentheses describes muons produced from pion decay, and the second term describes muons produced from the decay of kaons. Specifically, the values of 115 GeV and 850 GeV are the critical energies of these two types of particles, which is defined as the energy at which the probability to decay is equal to the probability of interaction at the height of a decay. This term is a function of muon zenith angle, θ , because at larger angles high energy pions will traverse less column density of the atmosphere before they decay, thus producing higher energy muons. The average muon energy at large angles is increased further by the fact that, once they are produced, low energy muons traverse more of the atmosphere and have a greater probability to decay than those at angles closer to the vertical. Figure 1.9 shows the measured muon spectrum at the surface for two angles ($\theta = 0^\circ$, $\theta = 75^\circ$). The line at $p_\mu \gtrsim 250$ GeV shows the parameterisation of Eq. (1.5) for vertical muons ($\theta = 0^\circ$).

Eq. (1.5) can be modified to take into account additional muon processes and the curvature of the Earth:

$$\frac{dI_{\mu 0}}{dE_{\mu 0}d\Omega} \approx \frac{0.14 \times A \times (E_{\mu 0} + \Delta E_{\mu 0})^{-\gamma}}{\text{cm}^2 \cdot \text{s} \cdot \text{sr} \cdot \text{GeV}} \times \left\{ \frac{1}{1 + \frac{1.1(E_{\mu 0} + \Delta E_{\mu 0}) \cos \theta^*}{115 \text{GeV}}} + \frac{0.054}{1 + \frac{1.1(E_{\mu 0} + \Delta E_{\mu 0}) \cos \theta^*}{850 \text{GeV}}} + R_c \right\} \times P_d. \quad (1.6)$$

The definition of the new parameters in Eq. (1.6) and their origins are as follows:

- The observed zenith angle on the ground, θ , is different from the zenith angle at the production of the muon in the atmosphere θ^* . The relationship between the two can be expressed as $\cos \theta = \sqrt{1 - 0.99 \cdot (1 - \cos^2 \theta^*)}$.
- $\Delta E_{\mu 0} = 2.06 \times 10^{-3} \cdot (1030 / \cos \theta - 120)$ is a modification to the muon energy to account for energy loss in the atmosphere.
- P_d is the probability a muon will *not* decay in the atmosphere. According to [44] this can be expressed as a^b where $a = \frac{120}{1030 / \cos \theta^*}$ and $b = \frac{1.04}{\cos \theta^* \cdot (E_{\mu 0} + \Delta E_{\mu 0} / 2)}$.
- R_c is the ratio of prompt muons to pions. Prompt muons are those coming from the decays of charmed particles. These are produced together with pions and

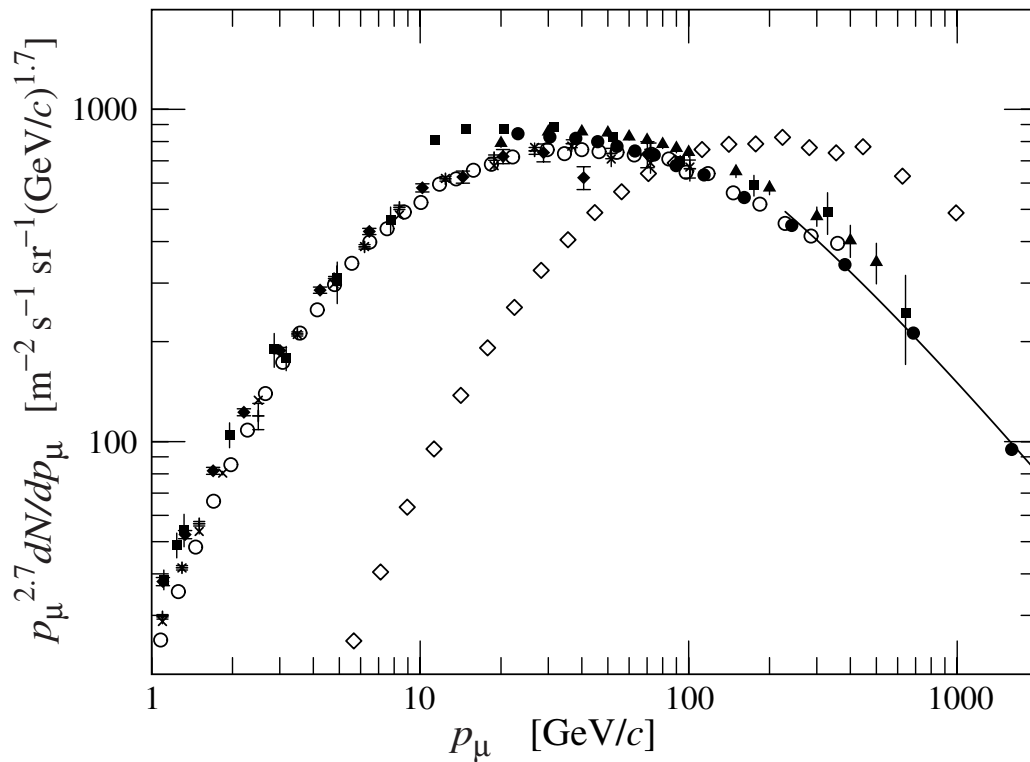


Figure 1.9: The spectrum of muons at the surface of the Earth measured at two angles from the vertical, $\theta=0^\circ$ (\blacklozenge , \blacksquare , \blacktriangledown , \blacktriangle , \times , $+$, \circ , \bullet) and at $\theta=75^\circ$ (\diamond). The symbols represent measurements from different experiments, as shown in [6] and the references therein.

kaons, but have much shorter lifetimes and decay immediately. The prompt muon spectrum is therefore the same as the primary cosmic ray energy spectrum. An upper limit on R_c of 2×10^{-4} was set by the LVD experiment [45], although the prompt muon flux does not contribute significantly to the intensities at large depths underground.

The normalisation factor A and the spectral index γ can be chosen to match experimental measurements of the muon spectrum. For shallow depths (< 1.5 km w. e.) following the normalisation proposed by Gaisser i.e. $A = 1$ and $\gamma = 2.7$ is recommended. For larger depths, experimental data is better fitted using a spectral index in the range 2.75 - 2.78. For depths of > 2.5 km w. e., which applies to many underground labs around the world (see Table 1.2), values of $A = 1.84$ and $\gamma = 2.77$ provide a good fit to the data. These values were obtained by the LVD experiment [44] based on muon measurements at Gran Sasso laboratory.

1.3 Muon distribution underground

The transport of muons through materials and their distribution underground is important for a number of tasks. For muon tomography of CO₂ storage sites, the distribution and intensity of muons underground is used to infer changes in the density distributions of the overburden after injection [46]. Cosmic-ray muons in underground observatories have been used to study the composition and spectrum of primary cosmic rays, and have also been used to improve the description of the muon spectrum at sea-level, as discussed in Section 1.2.1. For experiments located underground that are searching for rare events, cosmic-ray muons and the muon-induced products are an important background. Neutrons, which are produced by muon interactions with rock or other materials in the vicinity of a detector, can produce low-energy (keV-MeV) recoils in detectors searching for dark matter that are indistinguishable from signal-like events. Other muon-induced particles may also obscure low-energy signals in neutrino-less double-beta decay ($0\nu\beta\beta$) experiments and other neutrino searches. At higher energies, GeV-scale neutrons can produce signatures similar to proton decay, and in experiments seeking to detect atmospheric neutrinos down-going muons can be erroneously reconstructed as neutrino-induced upward-going muons. Muon-induced backgrounds will be discussed in more detail in Section 1.5.2.

1.3.1 Muon transport through materials

As is the case for all heavy charged particles, muons lose energy as they traverse materials. Since muons are charged particles, they will interact via the electromagnetic force with nuclei and atomic electrons in a medium. Ionisation energy loss is the process where energy is transferred from the passing muon to atomic electrons, and depending on the proximity of the muon the absorber atom will either be excited or ionised. The Bethe-Bloch formula describes the mean rate of energy loss of muons due to ionisation and excitation:

$$- \left\langle \frac{dE}{dX} \right\rangle = 4\pi\alpha^2 N_A \frac{Z}{A} \frac{z^2 (\hbar c)^2}{m_e^2 v^2} \left[\ln \frac{2m_e v^2 \gamma^2}{I} - \frac{v^2}{c^2} - \delta(\beta\gamma) \right] \quad (1.7)$$

where $\alpha = 1/137$ is the fine structure constant, z is the charge of the incident particle in units of electric charge, $\gamma = 1/\sqrt{1 - \frac{v^2}{c^2}} = \frac{E}{m_\mu c^2}$ is the Lorentz factor of the propagating muon with velocity v , mass m_μ and energy E , $I \simeq 16 \cdot Z^{0.9}$ eV is the mean ionisation potential of an atom. With increasing energy, the electric field of a muon extends to larger distances and there is an enhancement in collisions with distant electrons. In Eq. (1.8) this contribution, which scales as $\ln(\beta\gamma)$, is truncated by the density correction term $\delta(\beta\gamma)$. This is because the electric field of the muon acts to polarise atoms in real materials, screening distant electrons from interactions.

Muons also lose energy through radiative processes. These represent discrete points of large energy loss, in contrast to the smaller but continuous losses via ionisation. In general, the total mean energy loss of muons can be written as:

$$- \left\langle \frac{dE}{dx} \right\rangle = a(E) + b(E)E \quad (1.8)$$

where x represents a path length (in units of g/cm²), $a(E)$ is the energy loss due to ionisation and $b(E)$ represents the fractional energy loss via three stochastic processes:

- **Pair-production**

Muons are charged particles and therefore interact via the electromagnetic force, which is mediated by a virtual photon. In the field of a nucleus within a material, the virtual photon associated with a muon converts into a real electron-positron pair.

- **Bremsstrahlung**

As a muon passes close to an atomic nucleus it decelerates and radiates a photon. The energy loss of the muon equal to the energy of the emitted photon.

- **Muon-nuclear interactions**

A virtual photon radiated by a muon can interact directly inside a nucleus in the material producing hadrons.

In general, both $a(E)$ and $b(E)$ in Eq. (1.8) have a weak dependence on energy. The total stopping power of muons on copper, showing the contributions from ionisation and radiative processes, is shown in Figure 1.10. For high energy muons, losses by radiative processes start to dominate. The energy at which ionisation and radiative energy losses are equal is the critical energy E_μ^c and its value depends on the material through which the muons are propagating. For rock, a material that is relevant for the upcoming discussion on the muon spectra underground, $E_\mu^c \sim 690$ GeV assuming a mean atomic number $\langle Z \rangle = 11$.

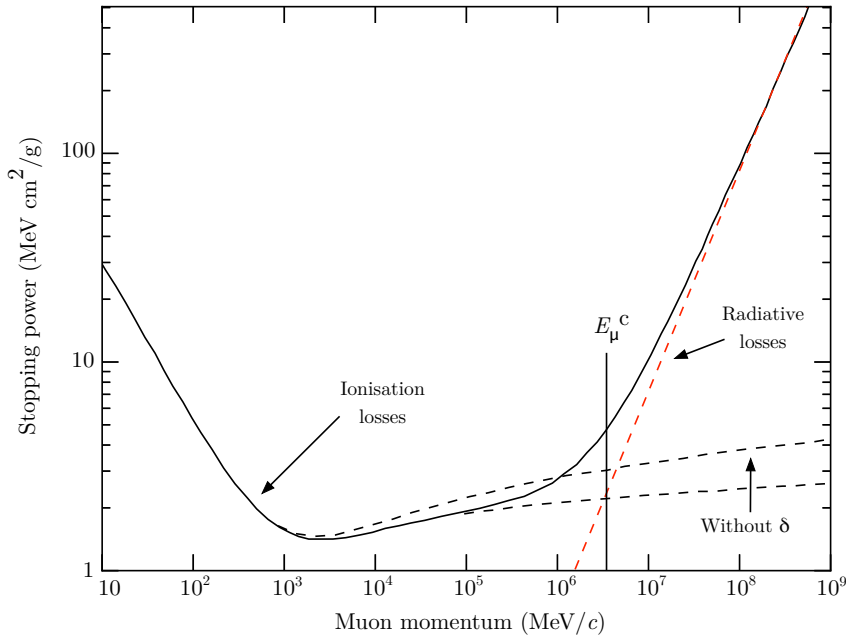


Figure 1.10: The stopping power of muons on copper, adapted from [6]. E_μ^c is the critical energy of muons, which is defined as the energy at which losses by ionisation and radiative processes are equal.

As well as losing energy, muons will also scatter during the pair production, bremsstrahlung and muon-nuclear processes. Muons are also deviated by elastic scattering from atomic nuclei via Coloumb interactions. In this type of scattering, the energy loss is negligible. Since muons encounter multiple nuclei when traversing a solid medium, the overall deflection from the original path is a culmination of all

the individual small angle deviations. For small deflections, the angular distribution is well described by a Gaussian. Less frequent ‘hard’ scatters, which result in larger deflections, produce non-Gaussian tails. The theory of Moliere [47] reproduces the angular distribution from multiple Coloumb scattering well. Computer codes that deal with the transport of muons through large thicknesses sometimes treat multiple Coloumb scattering using a Gaussian approximation [48].

1.3.2 Muons underground

Muons travelling to an underground site from the surface will undergo energy losses, as discussed in Section 1.3.1. As a muon loses energy it will either decay or be absorbed in the overburden material. As a result, the muon intensity underground decreases with depth.

A general formalism for the muon spectrum underground is given in Eq. (1.9). This expression convolves the spectrum at sea level $\frac{dI_{\mu 0}}{dE_{\mu 0}d\Omega}$, which is given in Eq. (1.6), and $P(E_{\mu}, X(\theta), E_{\mu 0})$ - the probability for a muon with an energy $E_{\mu 0}$ at the surface to have energy E_{μ} at a depth X ,

$$\frac{dI_{\mu}}{dE_{\mu}d\Omega}(E_{\mu}, \theta) = \int_0^{\infty} P(E_{\mu}, X(\theta), E_{\mu 0}) \frac{dI_{\mu 0}}{dE_{\mu 0}d\Omega}(E_{\mu 0}, \theta^*) dE_{\mu 0} \quad (1.9)$$

Computer codes are available to simulate the passage of muons through a large thickness of material to determine $P(E_{\mu}, X(\theta), E_{\mu 0})$. MUSIC (MUon SIMulation Code) [49, 8], PROPMU [50], MUM [51] and MMC [52], are codes that deal specifically with muon propagation taking into account the energy loss processes discussed in Section 1.3. Several codes exist because they were developed with different design goals and using different programming languages. Earlier algorithms, such as PROPMU, used simplified computational procedures due to limitations on CPU resources, while those developed at later times, such as MUSIC, were written to avoid these simplifications. In addition, new measurements of muon cross-sections became available which motivated new codes to be written, some with the flexibility to change these inputs. Figure 1.11 shows the vertical muon intensity as a function of depth in both water and rock based on the MUSIC code. The data points show measurements of the vertical muon intensity at different depths in rock and water. In addition to these codes, there are multi-purpose transport toolkits such as Geant4 [53] and FLUKA [54, 55], which have been shown to give comparable results. Figure 1.12 shows the energy spectra of muons E_{μ} with initial energy $E_{\mu 0} = 2$ TeV transported through $X = 3$ km of water using MUSIC, Geant4 and FLUKA.

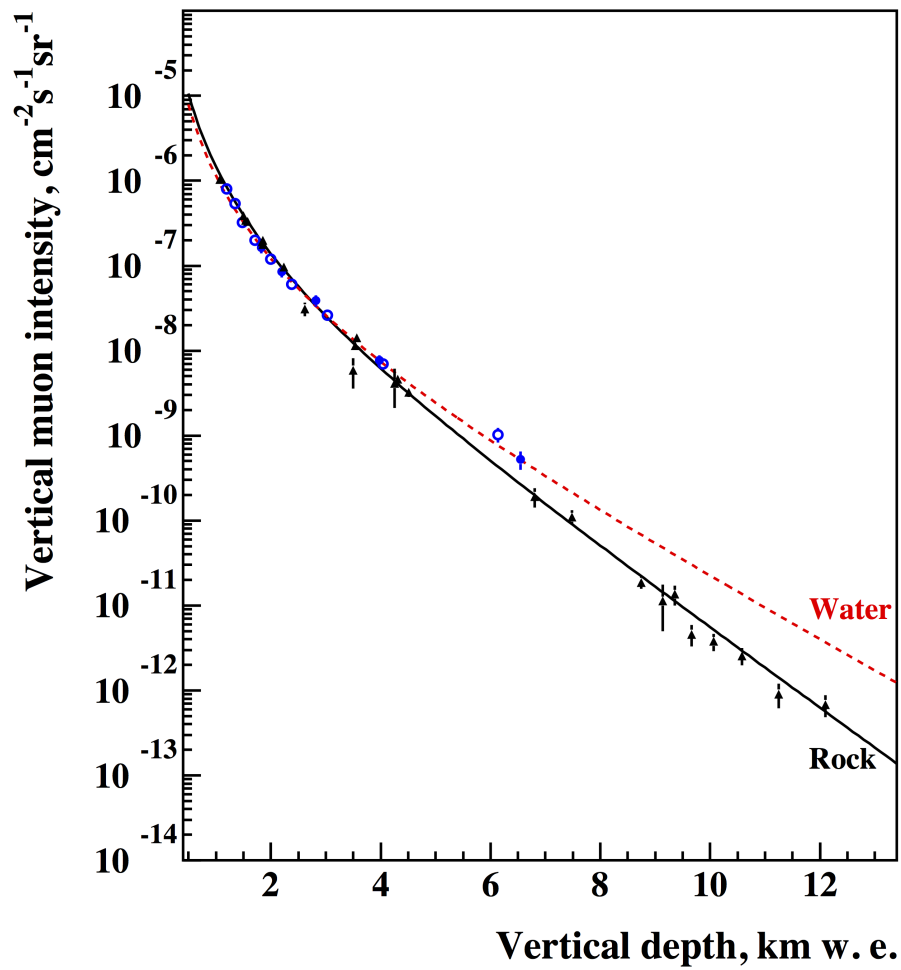


Figure 1.11: The depth-vertical muon intensity relation for standard rock and water (solid and dashed lines) as calculated using the MUSIC simulation code [8]. The data points for rock (filled triangles) are taken from from a collection of experiments [9]. The data points for water are taken from the Baikal [10] (open circles) and AMANDA [11] (filled circles) experiments.

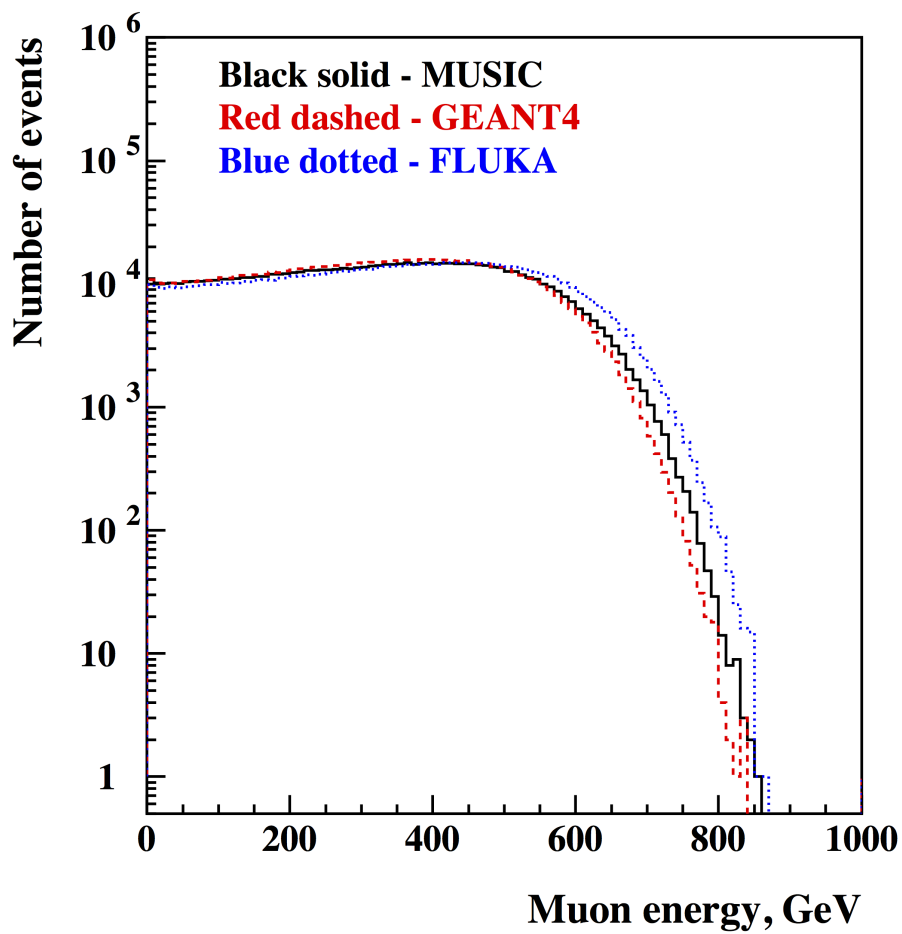


Figure 1.12: The energy spectra of 2 TeV muons transported through 3 km of water using MUSIC (solid curve), Geant4 (dashed curve) and FLUKA (dotted curve) [8].

1.4 Applications of muons

Cosmic-ray muons have been used in a number of scientific disciplines, primarily as a way to image the density distributions of large objects. This technique is nominally referred to as ‘muon tomography’, since multiple measurements of the muon intensity at different locations can be combined to build up a three dimensional image. Some sources use the term ‘muon radiography’ to distinguish applications that rely on muon absorption, in a similar way to X-ray radiography. For simplicity, in this thesis the term ‘muon tomography’ is used to refer to all applications that use the detection of muons for imaging purposes.

One of the first reported uses of muon tomography was in a search for hidden voids in the ancient pyramids [56]. Since then, it has been used to map density distributions in volcanoes to identify magma chambers [57, 58], in the exploration of rare-earth metals [59], and for the identification of illicit nuclear materials [60–62].

Recently, there has been interest in applying muon tomography to monitor carbon storage sites [46, 63]. The study presented in [46] suggests that the differences in muon intensities beneath a storage site that result from the change in density of a storage reservoir after CO₂ is injected are significant, and can be used to infer the emplacement of CO₂ in the subsurface. In Section 2.1 of this thesis, further study into the feasibility of muon tomography for this application will be described.

1.5 Backgrounds for underground detectors

Distinguishing signal events from background events is essential for all particle physics experiments. For muon tomography this is particularly important, since the technique requires a clear identification of muon signals to properly account for local changes in intensity or accurately reconstruct a scattering angle. As was noted in Section 1.3.2, the muon intensity underground falls quickly with depth, so muon detectors deployed for monitoring carbon storage sites will have strict requirements on the suppression of background signals. Other underground experiments such as non-accelerator neutrino detectors, direct dark matter searches and neutrino-less double beta-decay searches also require a full understanding of background sources and these should be mitigated where possible. For these experiments, signal events are especially rare. The latest limits on the cross-section for Weakly Interacting Massive Particles (WIMPs), for example, indicate that the event rate is $\ll 1$ event/day/kg [64].

Generally speaking, particle detection consists of a target material where an incoming particle interacts and deposits energy, producing some signal that is then detected by readout electronics and processed by a data acquisition system (DAQ) for further analysis. Given this setup, particles arising from sources of background may also be detected and be indistinguishable from signal events. The challenge then, is to design a detector that is sensitive enough to detect very rare processes that involve very small energy transfers while also rejecting an overwhelming number of background events.

The background particles of concern are high-energy (~ 100 keV - 3 MeV) γ -rays and neutrons, caused by interactions of cosmic-ray muons in the vicinity of the detector or local radioactivity. X-rays, low-energy electrons and α -particles are also troublesome if they are produced near to or inside the target volume. The strategies that are used to reject this background fall into two categories: discrimination and attenuation. The former is specific to the experimental setup, for example dark matter searches using two-phase noble liquid/gas detectors exploit the different scintillation/ionisation yields of electron and nuclear recoils. For some experiments, the expected signal will appear at certain energies, for example in neutrino-less double-beta decay ($0\nu\beta\beta$) searches, the signal of interest is produced by two electrons with a summed energy equal to the Q-value of the decay. Muon tomography for monitoring CCS sites is expected to identify muons with high efficiency due to the fact that they produce larger energy depositions than local radioactivity. The techniques for particle attenuation are, in principle, the same for all underground detectors although the requirements and specific arrangement will vary from one experiment to the next. Section 1.5.4 will discuss this in more detail. Common techniques involve shielding the target from the local environment, selecting radio-pure materials to be used for the detector construction and using special purification and cleaning procedures.

1.5.1 Cosmogenic backgrounds

At the surface of the Earth there is a significant flux of secondary cosmic-ray particles, produced in interactions of primary cosmic rays with the Earth's atmosphere. By going underground, an experiment can shield itself from most cosmic rays and operate in conditions with dramatically less backgrounds than are present at surface laboratories. Muons are the biggest worry as they are highly penetrating and account for over half of the total cosmic ray flux at the surface (~ 170 muons $\text{m}^{-2} \text{s}^{-1}$). Ultra-relativistic muons will not decay before reaching an underground site and their interactions with materials in the vicinity of a detector may produce dangerous secondary particles for high-sensitivity experiments, as discussed in Section 1.5.2. Atmospheric neutrinos

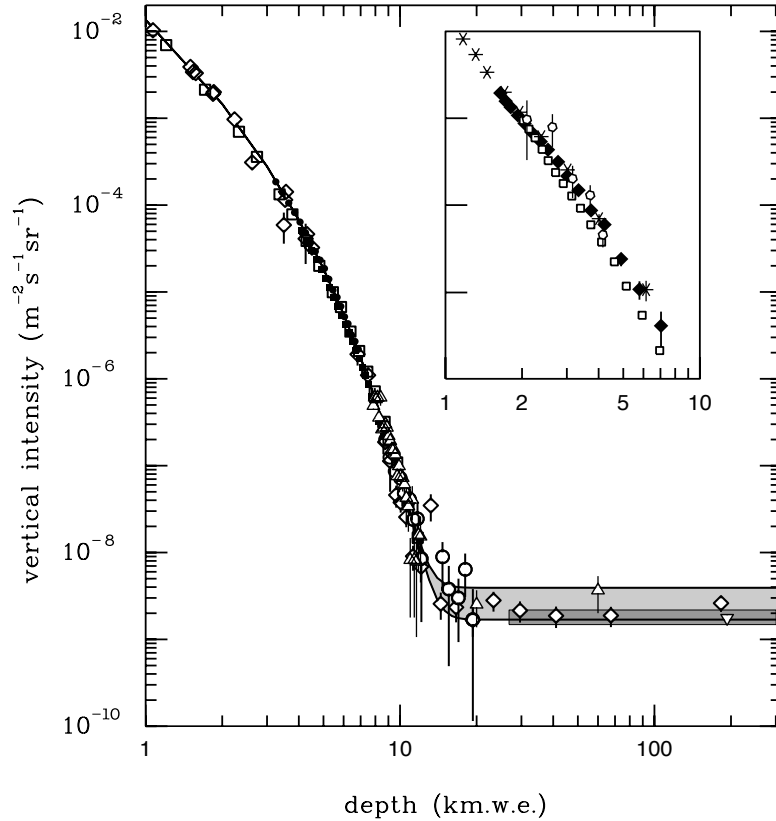


Figure 1.13: Vertical muon intensity as a function of depth (1 km w. e. = 10^5 g cm^{-2} of standard rock) [6]. The shaded area at depths > 15 km w. e. is due to neutrino-induced muons and the darker shading shows the muon flux measured by the Super-Kamiokande experiment. The insert shows vertical muon intensity vs depth for water and ice.

can also survive to large depths underground but because of their small interaction cross-section they do not give significant backgrounds. The vertical muon intensity as a function of depth is shown in Figure 1.13. Table 1.2 shows the depth and muon flux at several underground labs around the world.

1.5.2 Muon-induced backgrounds

Cosmic muons that survive underground and traverse a detector can be readily detected and identified as background events. High-energy muons can be a problem however, since they can produce secondary particles due to interactions in rock or other materials surrounding a detector. If the muon misses the detector, the associated secondary particles may produce signal-like events that cannot be rejected by a coin-

Table 1.2: The depth and measured muon flux at several underground laboratories. The references for the muon flux measurements are stated individually for each entry in the table. The depth information is taken from [21].

Laboratory	Depth (km)	Muon flux ($\text{cm}^{-2} \text{s}^{-1}$)
Kamioka	1.0	$(1.58 \pm 0.21) \times 10^{-7}$ [65]
Boulby	1.1	$(4.09 \pm 0.15) \times 10^{-8}$ [66]
Gran Sasso	1.4	$(3.14 \pm 0.08) \times 10^{-8}$ [67] $(3.20 \pm 0.03) \times 10^{-8}$ [68] [69]
SURF (4850 ft level)	1.5	$(5.31 \pm 0.17) \times 10^{-9}$ [70]
Modane	1.7	$(5.47 \pm 0.10) \times 10^{-9}$ [71]
SNOLAB	2.0	$(3.77 \pm 0.41) \times 10^{-10}$ [72]
Jinping	2.5	$(2.0 \pm 0.4) \times 10^{-10}$ [73]

cident muon track [74–78]. Muon-induced neutrons are particularly troublesome for certain high-sensitivity experiments, in particular WIMP dark matter detectors that cannot discriminate between single neutron interactions and WIMPs. The XENON100 experiment, for example, reported that muon-induced neutrons were the dominant nuclear recoil background for a 225 live-day dark matter search [79]. Despite having a much smaller contribution to the total underground neutron flux than those produced by local radioactivity, muon-induced neutrons have a much harder energy spectrum, ranging in energies up to several GeV. These fast neutrons can easily penetrate through passive shielding and interact in a detector. In fact, the neutron production cross-section for high-energy muons $\sigma_n \propto A^{0.8}$ meaning that high-A materials that are often utilised to shield a detector from external γ -rays can be a target for muon interactions.

There are several processes responsible for creating neutrons from high-energy muons:

$$\mu^- + X \rightarrow X' + n + \nu_\mu \quad (1.10)$$

$$\mu^- + p \rightarrow n + \nu_\mu \quad (1.11)$$

$$\gamma + X \rightarrow X' + n \quad (1.12)$$

$$\pi + X \rightarrow X' + n \quad (1.13)$$

where X and X' represent initial and final state nuclei. These interactions represent neutron production via nuclear reactions caused directly by muons - spallation (1.10) or negative muon capture on a proton in an atomic nucleus (1.11) - or their products - photons (1.12) and hadrons (1.13) produced in muon-induced electromagnetic or

hadronic cascades. The contribution of negative muon capture to the muon-induced neutron flux depends on the ratio of stopping-muons to through-going muons. The rate of stopping-muons has contributions from cosmic-ray muons that lose momentum travelling through rock and the production of low-energy secondary muons from photons in electromagnetic showers or interactions of primary muons via photo-nuclear interactions with atomic nuclei. Since low-energy muons do not survive to large depths underground, this ratio decreases with depth and is only significant at shallow depths ($\lesssim 100$ m w. e.). For deep sites, the rate of neutron production via muon-induced spallation - the disintegration of a nucleus due to the direct interaction of muons with nuclei - is significantly smaller than for hadronic and electromagnetic cascades.

In general, muon-induced neutron production depends on the depth of an underground site and composition of the overburden material. Several measurements of the muon-induced neutron flux have been made at underground sites and compared with simulations [75–78]. In general, there is good agreement between simulations using the Geant4 and FLUKA packages and data. For accurate simulations, the muon distribution at a particular location underground should first be obtained using muon transport codes such as those discussed in Section 1.3. In Section 2.2 a study of muon-induced backgrounds at the Sanford Underground Research Facility (SURF) will be described.

1.5.3 Radioactivity

Radioactive backgrounds are emitted during the decays of radioactive elements within or close to a detector. The decays in question can involve the transformation of a radioactive isotope into a stable nucleus via a single decay or via a chain of decays in which successive generations of radioactive nuclei are produced until a stable isotope is reached. Figure 1.14 shows an example of the later, whereby ^{238}U undergoes a series of 14 decays to reach a stable nucleus - ^{206}Pb .

There are three primary decay types; α -, β - and γ -decays. For α -decays the process can be written as:



where X and X' represent the chemical symbols of the initial and final state nuclei. β -decay involves the conversion of a proton into a neutron or a neutron into a proton within the nucleus:



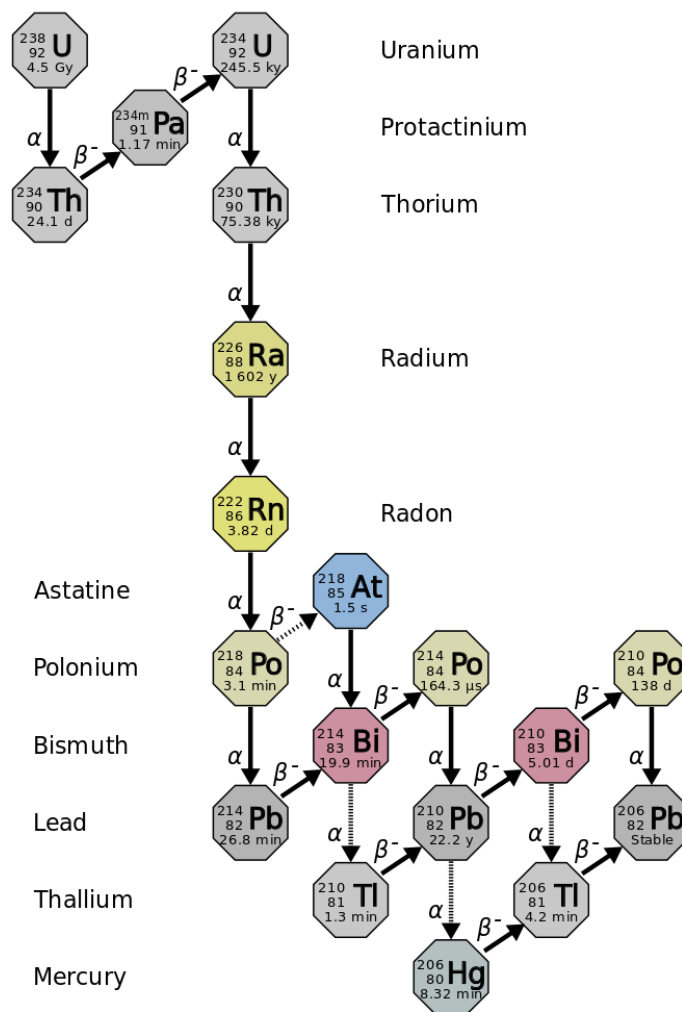


Figure 1.14: The ^{238}U decay chain. Figure taken from [12].

Most α and β decays result in an excited nuclear state that will decay rapidly to the ground state via the emission of one or more γ -rays. The exact energies of the decay products depend on the energy configuration of the excited nucleus. Excited nuclear states can also be produced by electron capture, in which the positive nucleus of an atom captures an orbiting electron. The nuclear de-excitation can be written as:



where X^* represents the excited nuclear species and X represents the ground state. Typically, the emitted γ -rays range in energy from a few tens of keV to a few MeV. Within the uranium and thorium decay chains, the highest energy γ -ray is 2.61 MeV, which accompanies the β -decay of ^{208}Tl into ^{208}Pb . Internal conversion is a competing process to γ -decay whereby a nucleus de-excites by transferring energy directly to an atomic electron, resulting in its emission from the atom. The resulting vacancy is occupied by an electron from a higher shell, resulting in the emission of X-rays or Auger electrons.

As well as radioactive decay, there is also the possibility of spontaneous fission whereby a heavy nucleus splits into two lighter nuclei with the emission of neutrons. Neutron production, which also includes contributions from (α, n) reactions on materials, will be discussed in more detail later in this subsection.

Decay laws and secular equilibrium

The decay of a sample of radioactive material containing N radioactive nuclei at time t is governed by the radioactive decay law:

$$-\frac{dN}{dt} = \lambda N \quad (1.18)$$

under the condition that no new nuclei are introduced into the sample. λ is the decay constant, the reciprocal of which is the average time that a nucleus will survive before it decays. λ is related to the half-life $t_{\frac{1}{2}}$, the time required for half of the nuclei in a sample to decay, by the equation:

$$t_{\frac{1}{2}} = \frac{\ln 2}{\lambda} \quad (1.19)$$

The assumption in Eq. (1.18), that no nuclei are introduced into the sample, is often invalid. Naturally occurring radioisotopes such as uranium (U) and thorium (Th) produce a chain of decays $1 \rightarrow 2 \rightarrow 3$ etc. where the product of each decay is a nucleus

that itself is radioactive. In this situation, the original isotope decays according to Eq. (1.18), but the concentration of daughter nuclei increases as a result of parent decays and decreases as a result of its own decay according to:

$$dN_2 = \lambda_1 N_1 dt - \lambda_2 N_2 dt \quad (1.20)$$

At $t = 0$, there are no daughter nuclei present and $N_2 = 0$. As the parent nuclei decays, the number of daughter nuclei increases while $\lambda_1 N_1 > \lambda_2 N_2$. As N_2 increases, so does the rate of the daughter decays until an equilibrium is reached i.e. $\lambda_1 N_1 = \lambda_2 N_2$ and therefore $\frac{dN_2}{dt} = 0$. Under these conditions the decay chain is in *secular equilibrium* and the activity $-\frac{dN}{dt} = \lambda N$ of each isotope is the same as the long-lived parent isotope. A general formula for the activity of the n^{th} isotope in a decay chain at some time t , expressed in terms of the decay constants (λ) and initial number of nuclei (N) of the preceding isotopes, is given by the Bateman equations [80]:

$$N_n(t) = \lambda_n \sum_{i=1}^n \left[N_i(0) \times \left(\prod_{j=i}^{n-1} \lambda_j \right) \times \left(\sum_{j=i}^n \left(\frac{e^{-\lambda_j t}}{\prod_{p=i, p \neq j}^n (\lambda_p - \lambda_j)} \right) \right) \right] \quad (1.21)$$

Figure 1.15 shows the activity of isotopes in the ^{238}U decay chain as a function of time according to Eq. (1.21) for the case where only nuclei of ^{238}U are present at $t = 0$ with an activity of 1 Bq. ^{238}U has a very long half-life (4.5×10^9 years), so its decay rate is effectively constant. As ^{234}Th and $^{234\text{m}}\text{Pa}$ have relatively short half-lives, 24.1 days and 1.18 minutes respectively, they reach equilibrium quickly as shown in Figure 1.15a. The rest of the chain is shown separately in Figure 1.15b because these isotopes take much longer to reach equilibrium (note the different time scales on the x -axis) due to the relatively long half-lives of ^{234}U ($t_{\frac{1}{2}} = 2.5 \times 10^5$ years) and ^{230}Th ($t_{\frac{1}{2}} = 8.0 \times 10^4$ years). The isotopes further down the chain are not shown in Figure 1.15b since their activities increase at effectively the same rate as ^{230}Th .

Background radiation from the environment (e.g. rock surrounding an underground detector) is often assumed to be in equilibrium since the effective age of the parent isotope is of the order of billions of years. Other radioactive sources, such as those found in materials used in detector construction, may be in disequilibrium because of the processes involved in manufacturing the components. Figure 1.16 shows the activities of isotopes on the ^{238}U decay chain as a function of time for two scenarios; the removal of 50% of the nuclei of (a) a short-lived isotope (^{222}Rn) and (b) a long-lived isotope (^{226}Ra). In scenario (a) the activity of all isotopes quickly returns to the equilibrium value of 1 Bq. In (b), the activity of ^{226}Ra increases very slowly because

of its long half-life. The short-lived isotopes further down the decay chain ($^{222}\text{Rn} \rightarrow ^{214}\text{Po}$) quickly fall into a new equilibrium with ^{226}Ra . ^{210}Pb , which is immediately after ^{214}Po in the decay chain, has a half-life of 22 years. It therefore has a much slower response to the break in equilibrium, and has an activity that roughly matches the top of the chain (all isotopes before ^{226}Ra) for the first few hundred days. Eventually, after $\gtrsim 100$ years, it reaches an equilibrium with ^{226}Ra .

Scenario (b) is an example of how changes in the concentrations of radioactive elements in a material can affect the activity of isotopes in the decay chain over very long time periods. The disequilibria that can occur means that background radiations from different parts of a decay chain should be considered independently, such that any variations in activity of can be properly taken into account. For example, in material screening campaigns that accompany low-background experiments, it is common practice for the activity of sub-chains within a decay chain to be reported separately. It is also important that background simulations are designed such that the activity of different parts of the chain can be normalised independently. This is will be considered in more detail in Section 3.1, where an event generator for radioactive decays will be described.

Neutron production

Neutrons from radioactivity are produced via spontaneous fission and (α, n) reactions. Spontaneous fission refers to the disintegration of a heavy nucleus into two lighter nuclei with the emission of neutrons. The process occurs for heavy nuclei and the final state nuclei are not rigidly determined, but statistically distributed over a range of medium-weight nuclei. ^{238}U is the only naturally occurring isotope that gives a significant flux of neutrons, but even in this case alpha decay is still much more frequent - the spontaneous fission branching ratio is 5.45×10^{-7} . Prompt γ -ray emission follows the emission of neutrons within ~ 1 ms after the fission event. The energy distribution of the neutrons follows Watt's spectrum:

$$N = N_0 e^{-aE} \sqrt{\sinh(bE)} \quad (1.22)$$

where N_0 is a normalisation constant obtained by integrating the spectrum over the total energy range and equating the resulting expression to the total neutron yield. The parameters a and b are dependent on the isotope undergoing fission.

Neutrons can also be produced when α -decays undergo (α, n) reactions in nearby materials. The process is written as:

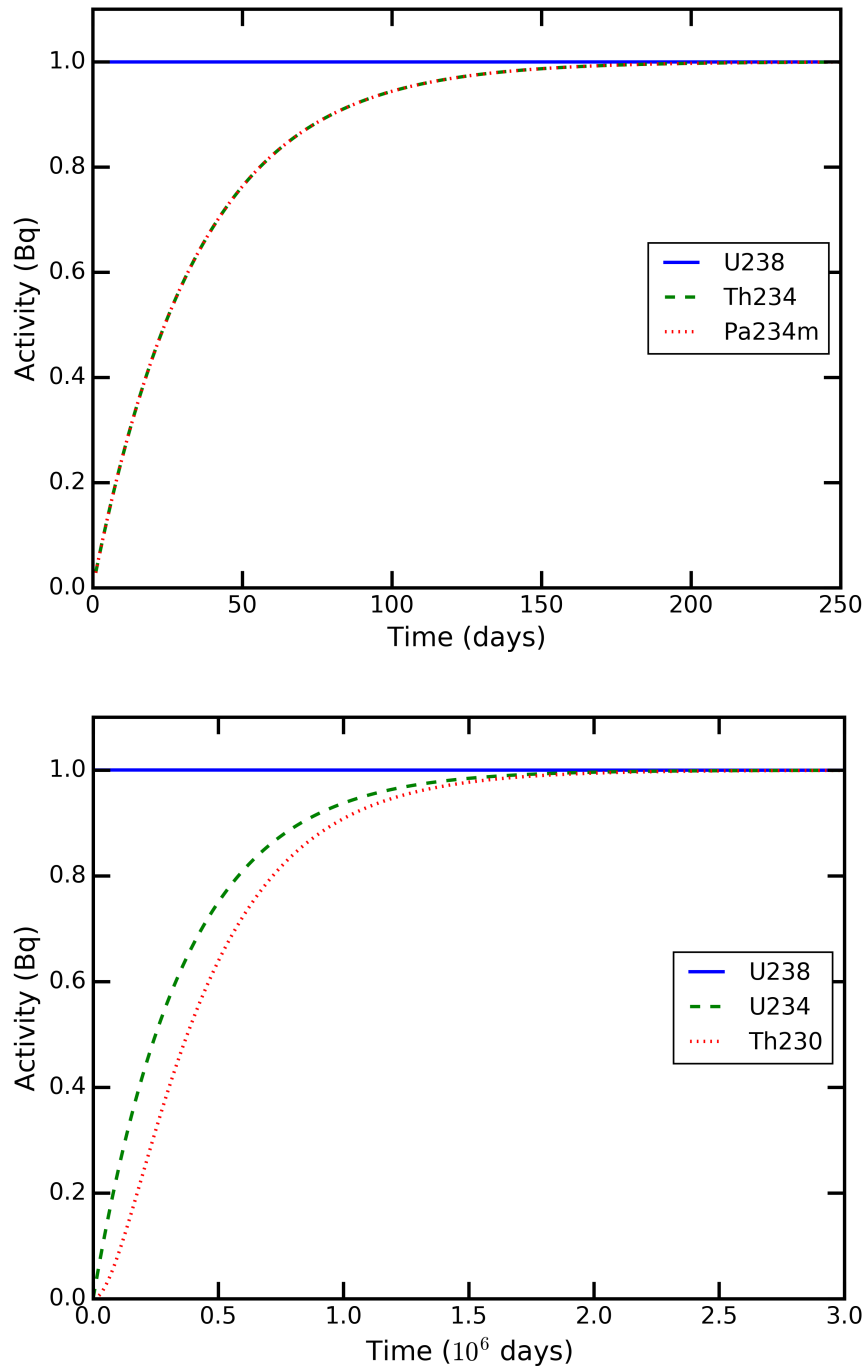


Figure 1.15: The activity of radioisotopes on the ^{238}U decay chain as a function of time assuming only ^{238}U nuclei are present at $t = 0$. In the top plot, ^{234}Th and $^{234\text{m}}\text{Pa}$, which immediately follow ^{238}U in the decay chain, are shown. In the bottom plot, significantly longer times are represented (note the different scale on the x -axis) for ^{234}U and ^{230}Th .

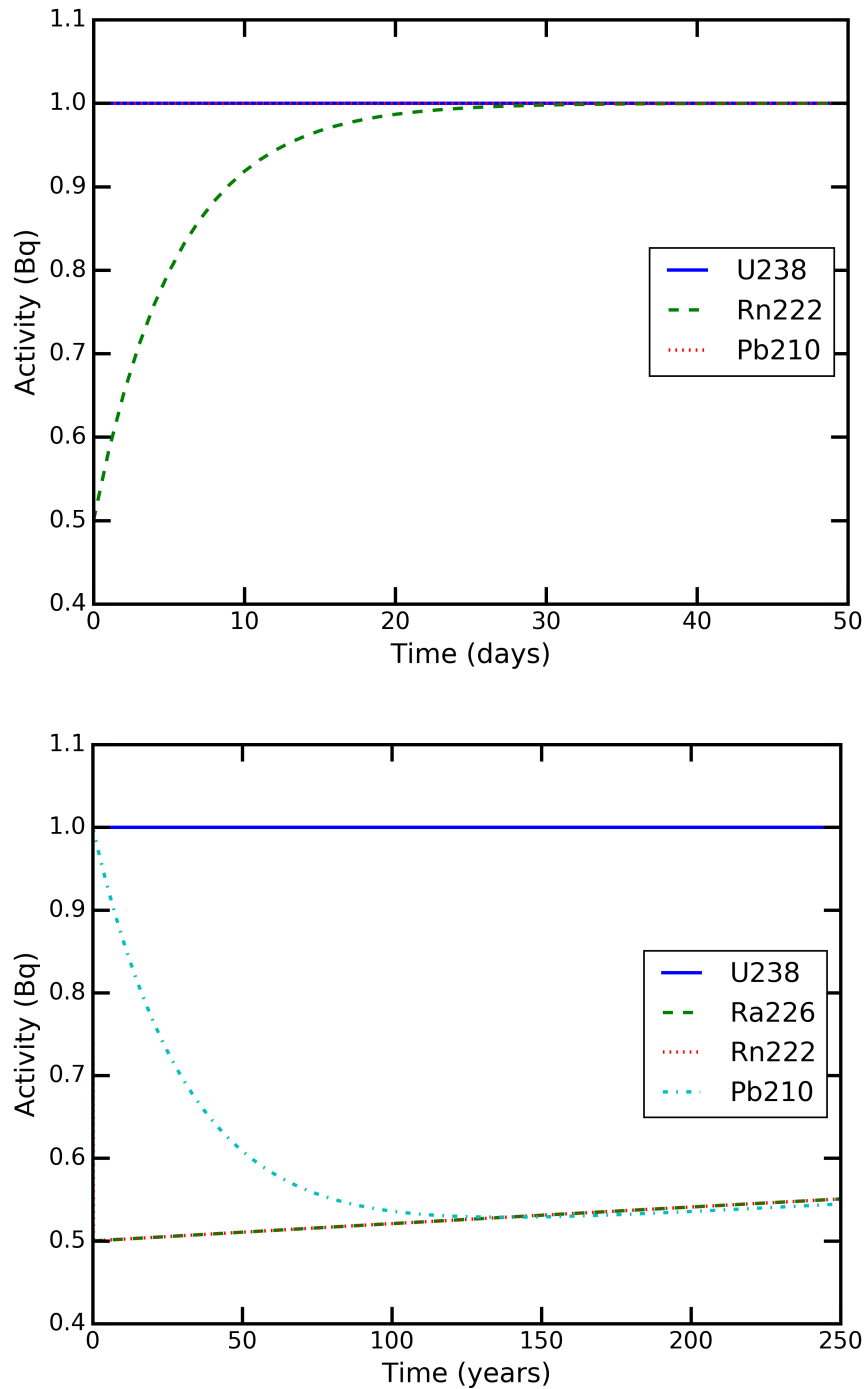
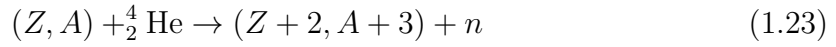


Figure 1.16: The activity of radioisotopes on the ^{238}U decay chain as a function of time, assuming that the chain is in equilibrium at $t = 0$, under two conditions; (a) the removal of 50% of the nuclei of ^{222}Rn (top plot) and (b) the removal of 50% of the nuclei of a long-lived isotope ^{226}Ra (bottom plot).



where (Z, A) represents a target nuclei with atomic number Z and atomic mass number A . When an α -particle encounters an atomic nucleus, the probability of a reaction is sensitive to the Coulomb barrier and the Q-value of the interaction. The Q-value is calculated as:

$$Q = (m_A + m_B - m_C - m_D)c^2 \quad (1.24)$$

where A and B represent the nuclei in the initial state and C and D represent those in the final state. If the Q-value is negative, the incoming α -particle should have a total kinetic energy in the centre-of-mass reference frame that exceeds $|Q|$ for the reaction to proceed. When converted to the laboratory frame, the minimum energy requirement is called the threshold energy. A positive Q-value indicates the reaction will release energy, but the reaction does not necessarily proceed in this case because of electrostatic repulsion that an α -particle needs to overcome to enter the target nucleus. An approximate form for the Coloumb barrier is:

$$E_c = \frac{Z_1 Z_2 e^2}{r_0 (A_1^{1/3} + A_2^{1/3})} \quad (1.25)$$

where $Z_1 = 2$, $A_1 = 4$, $e^2 = 1.44 \text{ MeV fm}$ and Z_2 and A_2 are the atomic number and atomic mass number of the target nucleus. Note that the two energy requirements imposed by the threshold energy and the Coloumb barrier are not additive.

The rate of (α, n) reactions is sensitive to the spectrum of α -particles coming from radioactive decay and the composition of the source material. Special codes have been developed to calculate the yields and spectra of neutrons coming from radioactive decays, taking into account both spontaneous fission and (α, n) reactions. These will be discussed in more detail in Section 3.3.7.

1.5.4 Shielding background particles

The passage of particles through materials is an important consideration for most underground experiments. Not only is it essential for understanding the response of a detector to a signal, but many experiments require a setup where a target material is shielded from an ambient background. The most worrisome source of background depends on the type of signal an experiment is seeking to observe. Plastic scintillators have been suggested as muon detectors for use in applying muon tomography to the

monitoring geological carbon storage projects [46, 63]. In this setup, X-rays and γ -rays from radioactive decays are the most worrisome background. For direct dark matter searches, neutrons that produce a single interaction in the target volume are indistinguishable from the nuclear recoil signature produced by a WIMP. The following sections discuss each major category of background radiations - neutrons, electrons, neutrons and γ -rays - and their passage through materials. The passage of α -particles and other heavy charged particles share much in common with muons, which was discussed in Section 1.3.1. α -particles from radioactivity are limited in energies to $\lesssim 10$ MeV, and at these energies they have a very small range in most materials. They are therefore only a concern if they are produced within a detector target.

Gamma rays

γ -rays undergo a number of different interactions during their transport through materials, each of which has an energy dependent cross section plotted in Figure 1.17 for a low- Z (carbon) and high- Z (lead) mass target. Unlike the behaviour of charged particles, all of these processes result in the partial or complete transfer of energy from the γ -ray in a single interaction. At intermediate energies of a few MeV the dominant process is Compton scattering, in which photons scatter from atomic electrons. Using the conservation of energy and momentum, it can be shown that the energy transferred to an electron, ΔE in such a collision is:

$$\Delta E = E - \frac{E}{1 + \frac{E}{m_e}(1 - \cos \theta)} \quad (1.26)$$

where E is the energy of the incident photon, $m_e = 0.511$ keV is the rest mass energy of the electron and θ is the angle of the scattered photon with respect to the incident photon trajectory. The cross section of Compton scattering is proportional to the density of electrons and therefore the density of the material. At low energies (< 1 MeV) and for high- Z targets, the atomic photoelectric effect is dominant. In this process, an incoming γ -ray is absorbed by an atom, and a photoelectron is ejected from an atomic shell. The total energy loss is the binding energy of the emitted photoelectron in its original atomic shell. The cross section of photoelectric absorption is proportional to $Z^{\approx 4.5}$. At higher energies, pair-production - the creation of an electron-positron pair from a photon in the electric field of an atomic nucleus - starts to dominate. The probability of pair production per nucleus is proportional to $Z^{\approx 2}$. It is clear, based on the energy loss processes described above, that high- Z materials are most effective in shielding a target from ambient γ -rays coming from radioactivity.

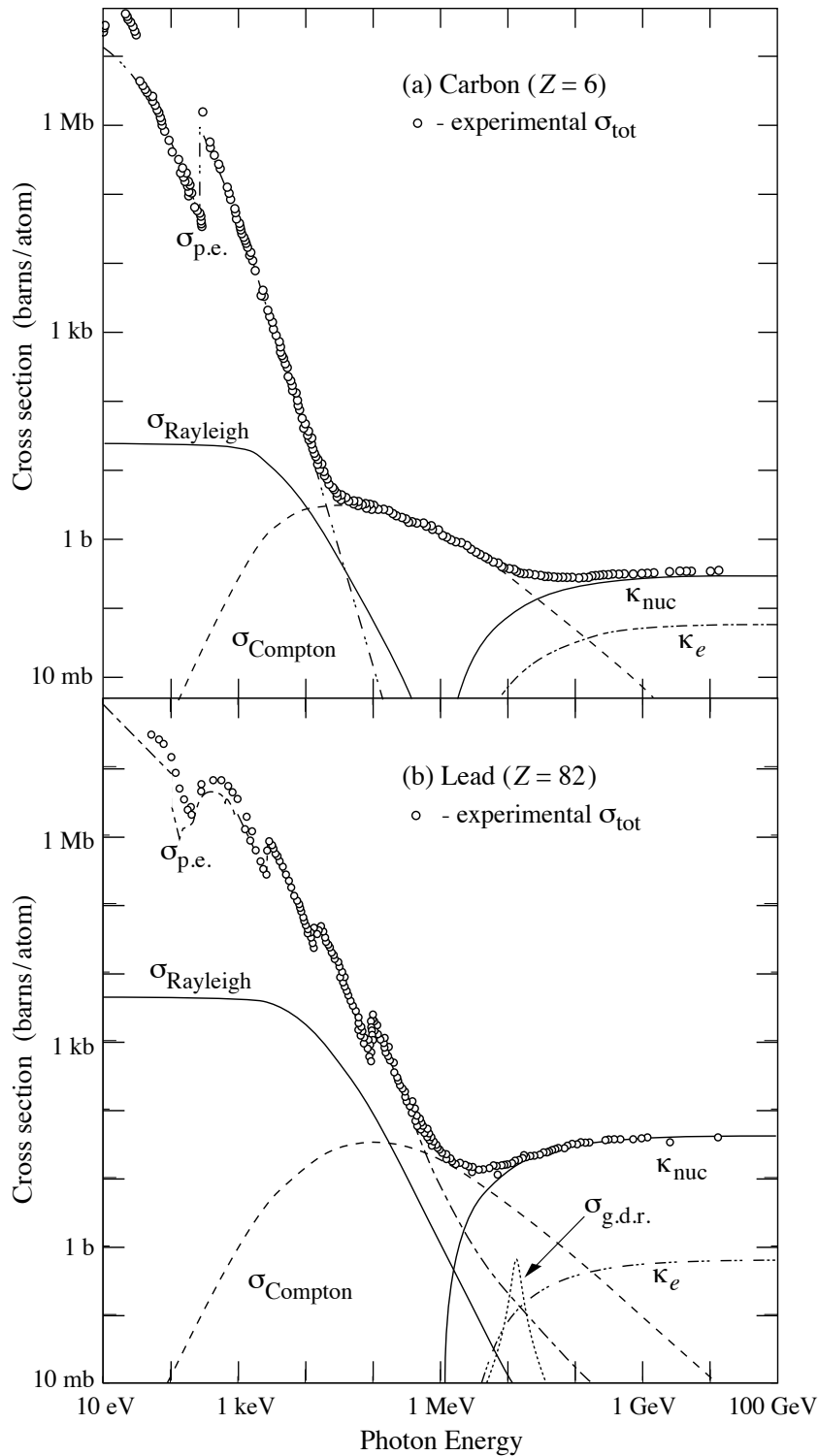


Figure 1.17: Total photon cross sections for two targets (carbon and lead) as a function of energy [6]. The contributions of the following processes are shown: $\sigma_{\text{p.e.}}$ = photoelectric effect, σ_{Rayleigh} = Rayleigh (coherent) scattering, σ_{Compton} = incoherent Compton scattering off an electron, κ_{nuc} = pair production (nuclear field), κ_e = pair production (electron field), $\sigma_{\text{g.d.r.}}$ = photonuclear interactions (Giant Dipole Resonance).

Neutrons

Fast neutrons undergo elastic and inelastic scattering as they travel through a material, and are moderated to thermal energies at which point they undergo capture on atomic nuclei. The energy loss for non-relativistic neutrons in an elastic scattering event is given by:

$$\Delta E = \frac{4m_n M_A E_n}{(m_n + M_A)^2} \cos^2 \theta \quad (1.27)$$

where m_n and M_A are the masses of the neutron and target nuclei respectively, E_n is the neutron energy and θ is the angle of incidence. By integrating Eq. (1.27) over all possible scattering angles the average energy loss is obtained:

$$\langle \Delta E \rangle = \frac{4m_n M_A E_n}{(m_n + M_A)^2} \frac{1}{2} \approx \frac{2A E_n}{(1 + A)^2} \quad (1.28)$$

where A is the atomic mass in atomic mass units. Low- A materials such as water or polyethylene are therefore most effective at shielding against neutrons. Neutrons from radioactivity are typically limited to energies of $\lesssim 10$ MeV whereas those from muon-induced interactions, discussed in Section 1.5.2, have much higher energies. An integrated veto system, which is able to tag neutrons that are not shielded, can therefore be used to suppress backgrounds further if required.

Electrons

Electrons lose energy via atomic excitation and ionisation, and can also emit bremsstrahlung photons. The range of electrons in materials typically used as targets in dark matter detectors is plotted in Figure 1.18. β -decay energies are typically of $O(\text{MeV})$, meaning electrons are shielded effectively by a few cm of the target material.

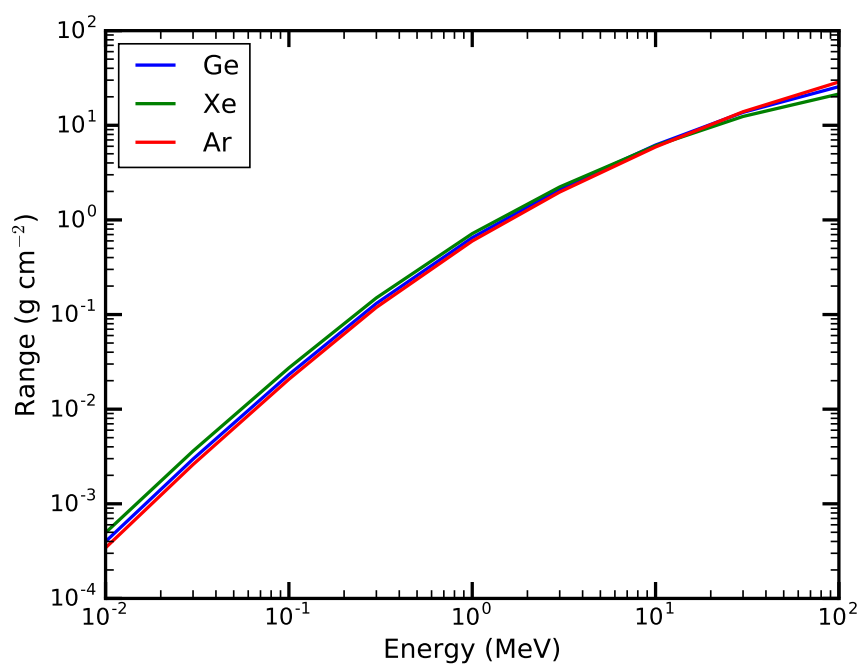


Figure 1.18: The range of electrons in xenon, argon and germanium as a function of incident energy calculated using data obtained from [13].

Chapter 2

Muon simulations

2.1 Muon simulations for carbon storage sites

In Section 1.1, carbon capture and storage (CCS) was introduced as a means of regulating atmospheric levels of CO_2 . A significant challenge related to CCS is the monitoring of CO_2 emplacement in the storage reservoir after its injection. For geological storage projects, the injected CO_2 will displace denser formation fluids, inducing changes in the density distribution of the subsurface. Muon tomography is a well-established technique that has been used to successfully map the density profiles of large objects by measuring variations in the flux of muons emerging from the target object [56, 58, 57]. Recently, it has been suggested as a monitoring method for CCS sites that could complement existing techniques such as repeat seismic surveys [46]. In this section, muon simulations for a detailed model of a geological CO_2 storage formation will be described. This work was undertaken as part of a collaboration, which was formed at the end of 2012, to investigate the use of muon tomography for carbon storage monitoring. The collaboration consisted of geoscientists from the University of Durham and NASA Jet Propulsion Laboratory, and physicists and engineers from the University of Sheffield and STFC Boulby Underground Science Facility. The project ended at the end of 2015 and was supported by grants from the Department of Energy and Climate Change (DECC), Premier Oil plc. and the Science & Technology Facilities Council (STFC).

2.1.1 Conceptual overview

Cosmic-ray muons can penetrate to large depths underground, with a probability that is fundamentally associated with the density of materials through which they travel. It

has been suggested that changes in density, and therefore the presence of CO_2 , can be inferred from variations in the muon intensity beneath a storage site. Furthermore, it may be possible to image the distribution of the CO_2 ‘plume’, and its subsequent growth over time, by measuring changes in muon intensity at certain angles.

For CCS monitoring, it is envisaged that an array of muon detectors will be placed inside specially drilled sidetrack boreholes - or ‘fishbone wells’ - beneath a storage site. This type of borehole geometry is commonly utilised in oil and gas exploration projects and can be achieved using drilling techniques and procedures developed in the hydrocarbon industry [81, 82]. Figure 2.1 shows an example of a setup that could be used for storage monitoring. This sketch is very approximate and the optimal setup will vary between storage sites. It may be possible, for example, to use existing wells at depleted oil/gas fields to house the muon detectors. The insert shows an example of the ‘fishbone’ structure, in which short sidetrack wells are drilled laterally from a mother bore.

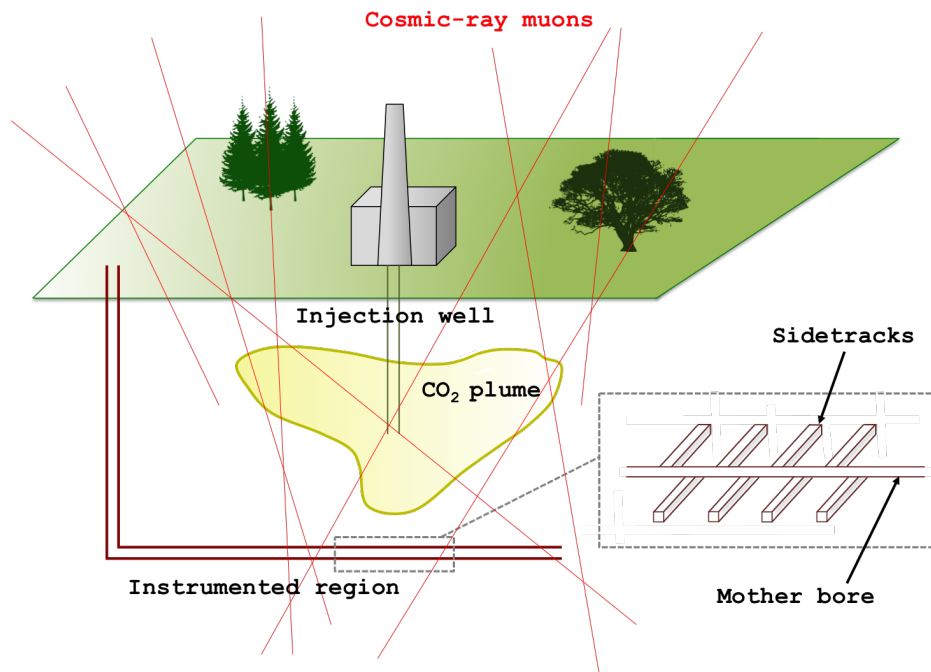


Figure 2.1: A sketch of the arrangement of muon detectors for monitoring CO_2 storage in an underground formation. Muons are detected beneath the injection region, using detectors that fit inside boreholes. In this representation, the detectors will be placed inside sidetracks that are drilled from a mother bore, as shown in the insert. The arrangement is similar for both on-shore and off-shore sites.

While several technologies are available for detecting muons, scintillators made of plastics are the most suitable detectors for this application. They are relatively

robust, cheap, can withstand high temperatures inside underground boreholes ($\sim 40\text{-}50\text{ }^\circ\text{C}$) and may operate autonomously for a number of years. Crucially, plastic scintillators can be designed with a small cross sectional area such that they can fit inside protective steel containers, which can then be placed inside boreholes. To fit inside a standard oil-well borehole, the containers would have an inner diameter of $\sim 20\text{ cm}$ and be sufficiently long to fit commercially available plastic scintillator bars. Since muons are charged particles, their interactions in the scintillator will produce a light signal that can be detected at both ends of the bar by the photosensors. The position of each muon ‘hit’ can be inferred from the time difference between the two signals, and a collection of bars coupled to a data acquisition (DAQ) system can be used to reconstruct a muon track. The collection of bars, each with a length of $\sim 100\text{ cm}$, then constitutes one borehole detector that is capable of both counting muons and measuring their trajectories. The muon angle in the plane perpendicular to the long side of the detector can be determined by the arrangement of bars that register a muon signal, whereas the muon angle in the plane parallel to the long side of the detector is determined by the positions of the hits along the bars. Tests on a prototype detector in a surface laboratory have been carried out to determine the position resolution along the length of a single scintillator bar [14]. In this study, a trigger setup was used to select muons incident at 10 cm increments along the bar. This arrangement allows the time difference between two pulses registered by photomultiplier tubes at either end of the bar to be determined and, simultaneously, the distance of the event along the bar. The time at which the height of each pulse drops to 20% of the peak value - the Constant Fraction Discriminant (CFD) - is shown in Figure 2.2a as a function of distance along the bar. The 1σ and 2σ bands refer to a Gaussian fitted to 1000 events collected at each position along the bar. Figure 2.2b shows the timing residual plotted against the fractional difference in signal amplitudes. It is clear that timing gives a better discrimination, although a combination of both quantities can yield higher resolution. Based on this study, it can be concluded that the position resolution along each bar is $\approx 10\text{ cm}$. Then, given the diameter of the detector, if a signal is identified in 5 separate scintillator bars by a passing muon, the angular resolution will $\sim 5^\circ$. The results presented in Section 2.1.6 will consider angular bins of at least 7° .

A previous study [46] has already suggested that the muon tomography is sensitive to post-injection density changes based on calculations of the muon intensity beneath a CO_2 storage reservoir. The goal of the simulations described here is to use a more detailed geological model that captures the non-uniformities in the rock layers of a typical storage site and the evolution of the reservoir density profile after injection

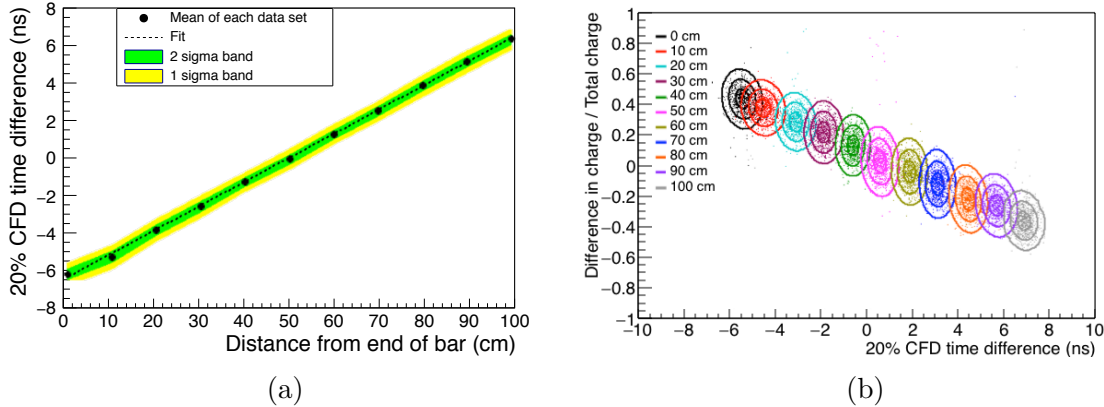


Figure 2.2: Left - the 20% CFD time difference as a function of distance along the bar. Each point represents the mean of 1000 events, and the green and yellow bands represent the 1σ and 2σ Gaussian deviations from this value. Right - the 20% CFD time difference and the fractional difference in signal amplitudes for each position along the bar. Each data point represents a single muon event, and the corresponding sigma contours for each cluster are overlaid. Both figures have been taken from [14].

begins. Several codes are available to transport muons, simulating their energy losses and eventual absorption or decay in the materials through which they are travelling. Codes that are built specifically for muon transport, such as MUSIC [49, 8], allow for faster computation times whereas multi-purpose transport codes such as Geant4 (GEANT = GEometry ANd Tracking) [53] provide more functionality for the construction of complicated geometries. As there is an intention to construct a detailed geometrical model of a geological repository, the Geant4 toolkit has been used to develop the framework for the simulations presented here. The essential components of the framework are (i) the generation of primary muons, which is described in Section 2.1.2, (ii) the geometry of the geological repository, which is described in Section 2.1.3, and (iii) the implementation of the physics models that describe the muon energy loss processes, which is described in Section 2.1.4.

2.1.2 Muons at the surface

In Section 1.2.1, the spectrum of cosmic-ray muons at the surface of the Earth was introduced. For these simulations, muons at the surface constitute the primary particles, and should be generated using the modified Gaisser's parameterisation introduced in Eq. (1.6). This is achieved using a stand-alone code that numerically integrates Eq. (1.6), giving a probability distribution function (PDF) $p(\theta, E)$ from which muons are

sampled. In reality, multiple distribution functions are defined; one as a function of θ , $f(\theta)$, and then multiple distributions for each θ value between θ_{min} and θ_{max} as a function of energy, $g_\theta(E)$.

Rewriting Eq. (1.6) as $\frac{dI_{\mu 0}}{dE_{\mu 0}d\Omega} = h(\theta, E)$, one can write the muon intensity as:

$$I = 2\pi \int_{E_{min}}^{E_{max}} \int_{\theta_{min}}^{\theta_{max}} h(\theta, E) \cdot \sin \theta \, d\theta dE \quad (2.1)$$

Note that the factor of 2π arises from the integral of the azimuthal angle ϕ over the limits $\phi_{min} = 0$ and $\phi_{max} = 2\pi$. Since $h(\theta, E)$ is a steep function and the integrations are performed numerically, it is convenient to rewrite Eq. 2.1 in terms of $l = \log(E)$:

$$I = 2\pi \int_{l_{min}}^{l_{max}} \int_{\theta_{min}}^{\theta_{max}} h(\theta, E) \cdot E \cdot \ln(10) \cdot \sin \theta \, d\theta dl \quad (2.2)$$

A Monte Carlo generator is used to produce muons according to the set of PDFs, $f(\theta)$ and $g_\theta(E)$. Since the energy spectrum of muons is dependent on θ , both parameters should be sampled simultaneously using two independent random numbers. As a validation of the muon sampling, the energy spectrum of muons from the generator is shown in Figure 2.3 for $65^\circ < \theta < 70^\circ$ and $160 \text{ GeV} < E < 1 \text{ TeV}$. This is in good agreement with the analytical form, derived directly from the modified Gaisser's parameterisation, which is also plotted. The generated zenith angle distribution is shown in Figure 2.4. At sea level, the angular distribution of muons is approximately $\cos^2(\theta)$ [6], so this function is also plotted for comparison.

After muons are generated, they are stored in a ROOT [83] file so that they may be read into the Geant4 code, event-by-event. The generator has also been integrated directly into the Geant4 code, which is more convenient for small-scale simulations but takes longer than reading from a file. For simulations involving high statistics, the option to read from a pre-generated file is used. The azimuthal angle (ϕ) is randomly distributed in the interval $[0^\circ, 360^\circ]$ and the position of each muon is sampled uniformly over the surface area of the geometry, as discussed in more detail in Section 2.1.4.

2.1.3 Geometry construction

The main motivation of these simulations is to study the sensitivity of muon tomography using a realistic model of a carbon storage site. This should include a detailed description of the typical geological features, specifically the stratigraphy, density and composition of the subsurface rock. Despite not being an option for CCS, a model of the geology in the vicinity of the Boulby Mine, located in Cleveland, United Kingdom, has been used for this study. The mine is located in the North East of England, as shown in

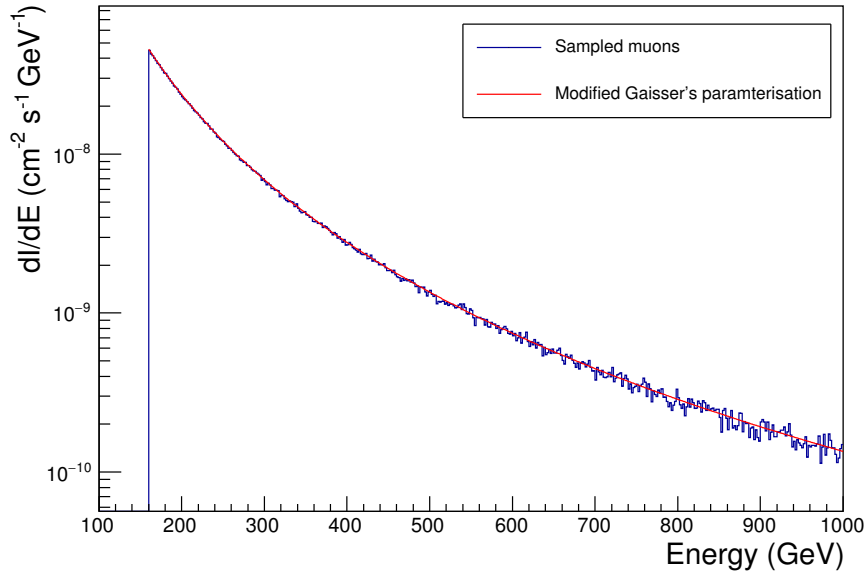


Figure 2.3: The energy of muons sampled with zenith angles $65^\circ < \theta < 70^\circ$ and energy $160 \text{ GeV} < E < 1 \text{ TeV}$ (blue) and the analytical distribution obtained using Eq. (1.6) (red). This provides a validation of the Monte Carlo code for sampling muons at the surface.

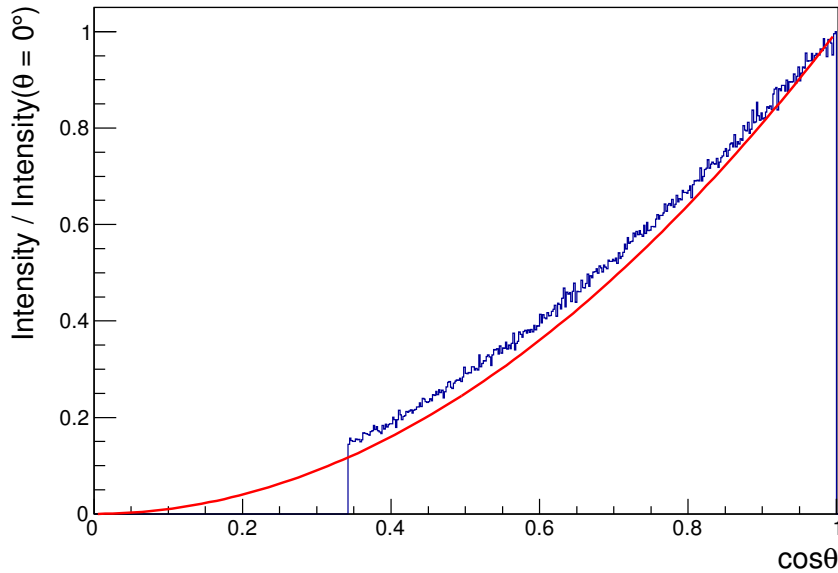


Figure 2.4: The $\cos(\theta)$ distribution of sampled muons (blue), where θ represents the zenith angle of muons, normalised to the vertical ($\theta = 0$) intensity. The red line shows a $\cos^2(\theta)$ distribution for comparison.

Figure 2.5, and extends out beneath the North Sea. It is the site of the STFC Boulby Underground Science Facility [84], which has hosted a number of low-background experiments and detectors, most notably the ZEPLIN dark matter experiment, a predecessor the LUX-ZEPLIN experiment that will be discussed in Section 2.2. The geology of the Boulby site is well understood, and is representative of a typical of a storage site; injection will be considered in a sandstone layer of rock which sits directly beneath an impermeable mudstone rock. An unfaulted geocellular model of the repository has been produced by geologists at the University of Durham (Prof. Jon Gluyas and Dr. Samantha Clark). The model consists of five rock layers, each of which are depicted in Figure 2.6 along with their bulk densities and simplified compositions. From now on these layers will be referred to as ‘L1’ through to ‘L5’ for convenience. Data from four seismic horizons, provided by Israel Chemicals Ltd UK, were used to construct most of the layers. The data corresponds to the top of L1 (the sea bed), the top of L4, the common horizon of L4 and L5 and the bottom of L5. The profile of the bottom of L1 and L2 are based on the estimated rock thicknesses from well data. A proprietary software product called JewelSuiteTM was used to import the seismic and well log data and produce a three-dimensional grid that describes the topology of each layer. The mean bulk density values and elemental compositions of each of the layers were calculated using paper compositional logs and provided as a separate data file.



Figure 2.5: A map of the United Kingdom showing the location of the Boulby Mine on the North East coast of England.

The geocellular model is exported as a corner-point grid - a format that is commonly used in geosciences to describe geological repositories. The corner-point grid consists of a set of straight lines or pillars running vertically through the geometry and nodes, which make up the corner-points of each cell, defined by their distances along the pillars. An example of the corner-point grid describing a simple geometry is shown in Figure 2.7. A python program was developed to convert the corner point grid into a collection of triangular and quadrangular based meshes. Each mesh represents the top/bottom of a layer of rock and is made up of a series of faces. For the triangular mesh, which describes the more detailed horizons, each face comprises 4 triangles that are defined by a central vertex and 4 corner vertices. For the quadrangular mesh, which describes all other horizons, each face is simply defined by the 4 corner vertices. A representation of the two types of meshes is shown in Figure 2.7. The faces of each cell are stored as a ROOT file and then imported into Geant4 for the geometry construction. Figure 2.8 shows a 3D representation of the repository after the conversion.

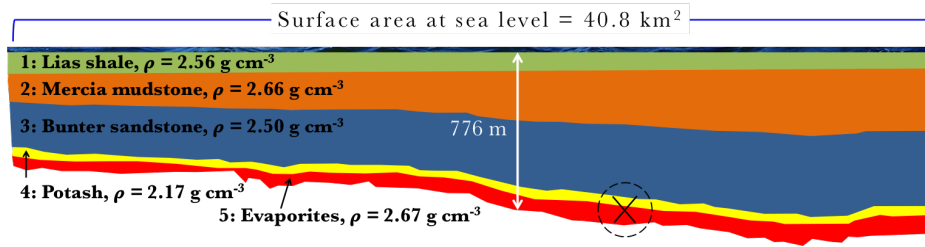


Figure 2.6: A 2D drawing of the geological repository showing the bulk density values (before injection) of the rock layers. X marks the location of the detector site used in this study.

The approximate location of the muon detectors considered in this study is shown in Figure 2.6 at a depth of 776 m below the sea bed. The depth of seawater vertically above the detector site is 32 m. Initially, the simulations record all muons that pass through a flat plane with a total surface area $A_{det} = 1000 \text{ m}^2$. This constitutes the total instrumented area, although in reality the area covered by muon detectors may be smaller and they will not be arranged to cover a flat plane. In Section 2.1.7, the effect of different detector arrangements on the muon detection efficiency will be investigated in more detail. This will provide a scaling factor for results that are obtained assuming a 100% muon detection efficiency over A_{det} .

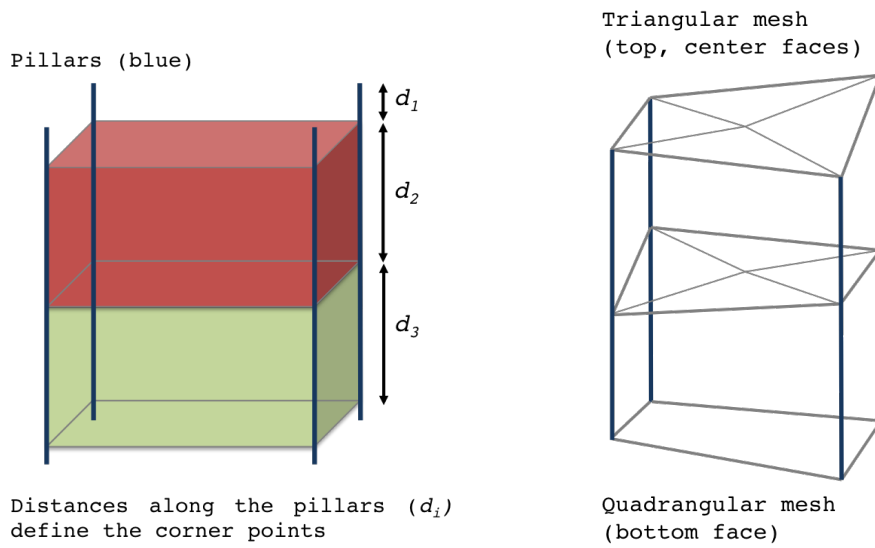


Figure 2.7: Left - a sketch of the corner-point grid geometry showing the definition of two cells, each with 8 corner points, defined according to 4 pillars and distances d_i along the pillars. Right - a representation of the triangular and quadrangular meshes used to describe irregular cells in the model.

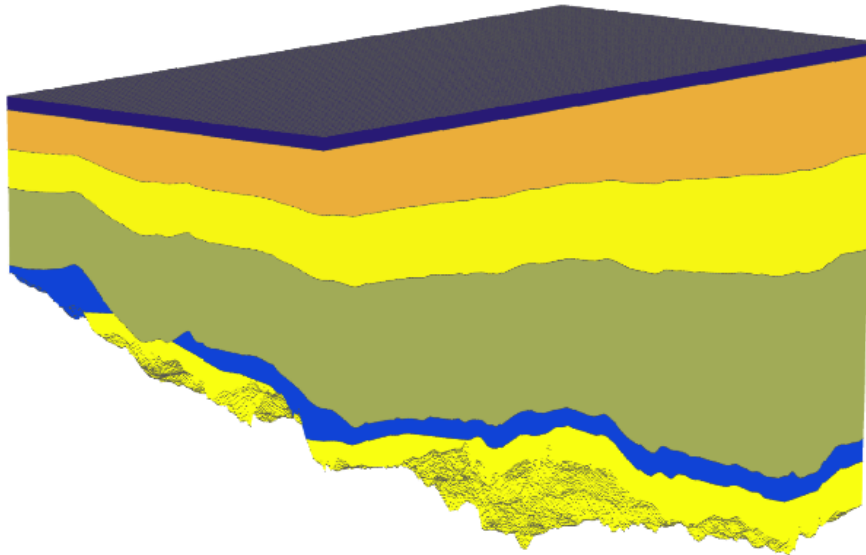


Figure 2.8: A 3D drawing of the geological repository for use in Geant4 after converting the corner-point grid into triangular and quadrangular meshes.

2.1.4 Code setup, validations and optimisations

The critical aspect of muon tomography for monitoring CCS sites is the change in muon survival probability, and therefore muon intensity, due to variations in the density profile of the rock overburden above a detector site. The simulations therefore rely on an accurate model of muon propagation and energy loss as they travel through the geological repository. Geant4 provides a description of the muon energy loss mechanisms in a pre-defined physics list called `shielding`. To test that these physics processes are correctly defined in the simulation framework developed for this study, muons are propagated through 3 km water equivalent (w. e.) of ‘standard rock’ - a material with atomic number $Z = 11$, atomic mass $A = 22$ and density $\rho = 2.65 \text{ g cm}^{-3}$. The distribution of surviving muons is then compared with the same simulation performed using the MUSIC code. The energy spectra and displacement along the x -axis ¹ are shown in Figures 2.9 and 2.10 and are in good agreement. The differences in Figure 2.9 at high energies has been observed in previous studies - as was shown in Figure 1.12, which is taken from [8] - and is understood to be a genuine difference between the two codes. The energy loss of muons, and therefore the energy spectrum, is sensitive to the density of the material whereas the displacement is dependent on the material composition.

One of the biggest challenges in transporting muons to a location deep underground using a multi-purpose transport code is the long computation times. Broadly, there are two strategies for improving the computing performance; (i) immediately throw away muons at the surface that cannot survive to the detector site and (ii) transport the remaining muons as efficiently as possible. Based on previous studies [49, 8] muons with an energy $E < 400 \text{ GeV}$ and zenith angle $\theta > 70^\circ$ will not survive to the depths considered here, and are therefore excluded from the simulation immediately. Of the remaining muons, all those that can pass through an area $A_{det} = 1000 \text{ m}^2$ at the detector location are recorded for further propagation. Given the constraint on θ , muons are generated uniformly over an area of approximately $4.5 \times 4.5 \text{ km}^2$ at sea level. This area is sufficiently large to account for all muons that, geometrically, can possibly reach the detectable area. This includes muons that undergo scattering during transport and finish with a position at the detector site, (x_{det}, y_{det}) that is displaced from the linearly projected position (x_{proj}, y_{proj}) . The distribution of $|r_{det} - r_{proj}|$, where $r_{det} = \sqrt{x_{det}^2 + y_{det}^2}$ and $r_{proj} = \sqrt{x_{proj}^2 + y_{proj}^2}$, for muons that have been propagated through the geometry of the repository is shown in Figure 2.11. While $4.5 \times 4.5 \text{ km}^2$ is required to account for all muons that can possibly reach the detector

¹In this setup the x -axis is perpendicular to the initial muon trajectory.

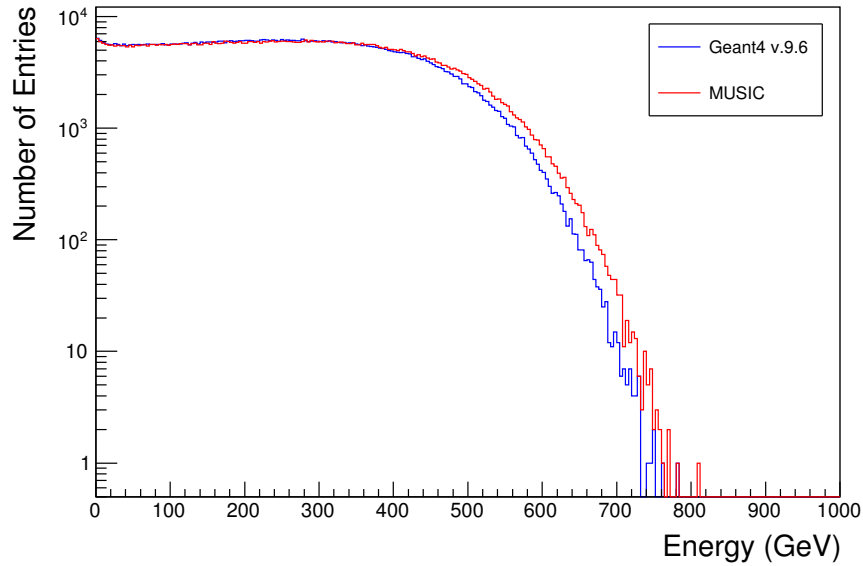


Figure 2.9: The energy spectrum of 2 TeV muons transported through 3 km w. e. in standard rock ($Z = 11$, $A = 22$) using the Geant4 v.9.6 (blue) and MUSIC (red) computer codes.

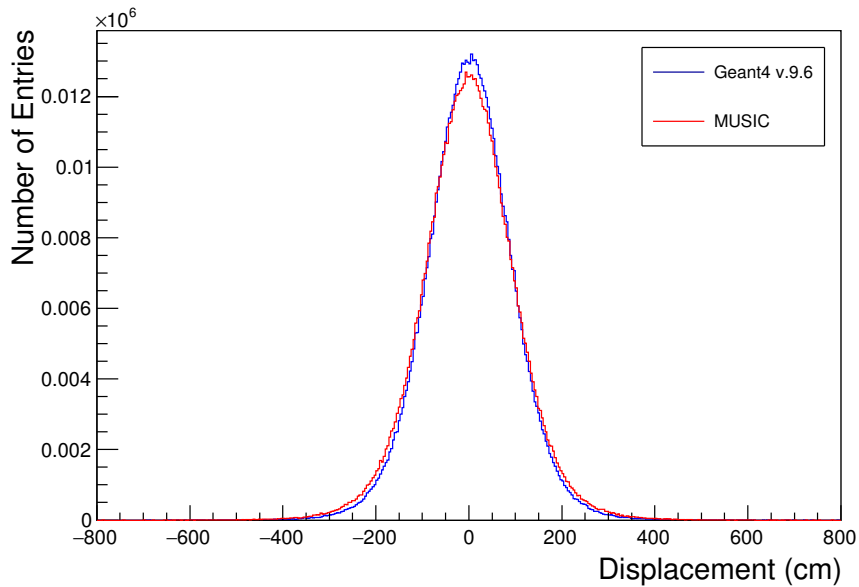


Figure 2.10: The displacement along the x -axis of 2 TeV muons transported through 3 km w. e. in standard rock ($Z = 11$, $A = 22$) using the GEANT v.9.6 (blue) and MUSIC (red) computer codes.

site, a large fraction of muons generated over this area will still pass outside of the detector region after accounting for their trajectories. As muons are generated at sea level using the generator described in Section 2.1.2, each muon is projected to the detector depth, and those falling outside of a $50 \times 50 \text{ m}^2$ area are thrown away. The fraction of muons surviving this initial geometrical cut, $\epsilon = 1.218 \times 10^{-4}$.

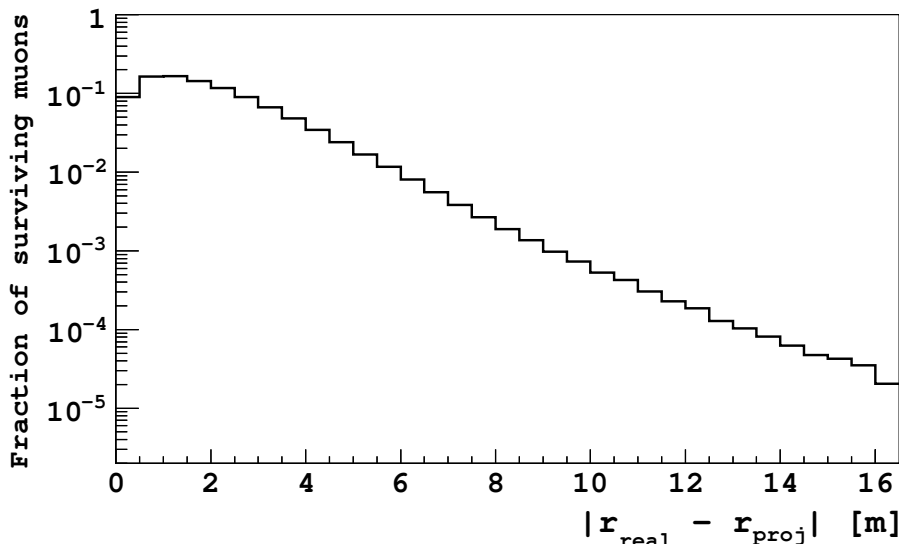


Figure 2.11: The distribution of $|r_{det} - r_{proj}|$ describing the displacement of muons measured with a radial position, r_{det} , from their projected radial position at the detector site, r_{proj} (calculated based on the muon trajectory at sea level) [15].

Since Geant4 is designed as a multi-purpose toolkit, it is the responsibility of the code developer to optimise particle transport given the specific requirements of the simulation. By default, Geant4 tracks all secondary particles produced by muon interactions in the rock but for studies related to muon tomography, only the energy loss of muons in these interactions is important. Therefore, all non-muonic particles are immediately removed from the simulation at the point of production. In addition, each time a muon loses energy in the simulation, its maximum survival depth is evaluated using a look-up table. The look-up table is populated using the MUSIC simulation code and defines a distance, d_{max} beyond which a muon with an energy, E , has a survival probability of less than 10^{-6} . MUSIC considers muon propagation through materials with a uniform density, so $d_{max}(E)$ is evaluated for a material with a density $\rho = 2.17 \text{ g cm}^{-3}$, which is the lowest density layer considered in this study. Any muon with a remaining distance $d_{prop} > d_{max}$ is removed from the simulation.

To test the simulation framework and the optimisations described above, a simple study is undertaken using initial muons produced by the generator introduced in

Table 2.1: Muon intensities and mean energies at a depth of 2 km w. e. for ‘standard rock’ using the Geant4 and MUSIC codes. The difference between the muon fluxes is due to different detector configurations - MUSIC records muons on a spherical surface whereas the Geant4 simulations use a flat surface.

	Muon intensity ($10^{-7} \text{ cm}^{-2} \text{ s}^{-1}$)	Mean muon energy (GeV)
Geant4	1.45	228
MUSIC	1.99	225

Section 2.1.2. The study considers the same ‘standard rock’ ($Z = 11$, $A = 22$ and $\rho = 2.65 \text{ g cm}^{-3}$) that was introduced previously, and a flat detector with an area $A_{det} = 1000 \text{ m}^2$ positioned at a depth of 2 km w. e. The flux of muons at the detector site is given by:

$$\psi_{\mu} = \frac{N_{det}}{N_{gen}/\epsilon} \frac{A_{gen}}{A_{det}} \psi_{\mu}^{surf} \quad (2.3)$$

where N_{gen} is the number of muons generated over an area $A_{gen} = 2.025 \times 10^7 \text{ m}^2$, $\epsilon = 1.218 \times 10^{-4}$ is efficiency of the geometric cut, N_{det} is the number of muons that are detected and ψ_{μ}^{surf} is the flux of muons at the surface. Muons at the surface were generated with energies $0.4 < E < 10^6 \text{ TeV}$, and zenith angles $\theta < 70^\circ$. Integrating Gaisser’s parameterisation, given in Eq. (1.6), over these ranges gives a surface flux $\psi_{\mu}^{surf} = 3.43 \times 10^{-6} \text{ cm}^{-2} \text{ s}^{-1}$. The muon intensity and average muon energy at 2 km w.e depth is presented in Table 2.1 alongside values obtained using the MUSIC code. The difference between the fluxes is understood to be related to configuration of the detector - MUSIC records muons on a spherical surface whereas the Geant4 simulations use a flat surface.

With the optimisations described above, it takes approximately 0.1 CPU seconds to transport each muon through the geometry. Muons are generated over a surface area $A_{gen} = 4.5 \times 4.5 \text{ km}^2$ and the flux of muons at the surface is $\psi_{\mu}^{surf} = 3.43 \times 10^{-6} \text{ cm}^{-2} \text{ s}^{-1}$. The efficiency of geometric cut ϵ , described in Section 2.1.4, is 1.218×10^{-4} and therefore the number of initial muons that correspond to 1 live year of statistics is:

$$N_{\mu} = \psi_{\mu}^{surf} \cdot A_{gen} \cdot \epsilon \cdot N_s \quad (2.4)$$

where $N_s = 3.16 \times 10^7$ is the number of seconds in a year. This equates to a total run time of $\sim 7.4 \times 10^4$ CPU hours. This is only manageable using a batch computing system, which allows several instances of the simulation to be run in parallel to reduce the overall time required for simulations. Each computing ‘job’ uses a statistically

independent set of initial muons, produced and stored using the generator described in Section 2.1.2. The output files, which are stored in a ROOT format, are saved to the local disk of each computing node and then transferred to a central data disk to be accessed later for further analysis.

2.1.5 Subsurface carbon dioxide distributions

To understand how the presence of CO₂ in the reservoir affects the muon intensity at the detector site, the expected bulk density changes of the reservoir need to be calculated and included in the model. To begin, a simple model is used in which the bulk density, ρ_{L3} , of the entire injection layer is varied from 2.500 g·cm⁻³ (the ‘no-CO₂’ scenario) to 2.478 g·cm⁻³ (the ‘nominal-CO₂’ scenario). An additional case was also considered where the bulk density changes to 2.463 g·cm⁻³ (the ‘extreme-CO₂’ scenario). The values of ρ_{L3} are provided by the Durham group based on the expected density changes in the Bunter Sandstone (L3 in Figure 2.6). This layer actually consists of interbedded sandstones and mudstones, with around 50% being formed of sandstone and 50% of shales. The average porosity of the shale $p_{shale} = 0.12$ and the sandstone $p_{sand} = 0.15$. The average bulk density is then calculated as:

$$\rho_{L3} = 0.5 \cdot ((1 - p_{shale}) \cdot \rho_{shale} + p_{shale} \cdot \rho_{brine}) + 0.5 \cdot ((1 - p_{sand}) \cdot \rho_{sand} + \Lambda \cdot p_{sand} \cdot \rho_{CO_2} + (1 - \Lambda) \cdot p_{sand} \cdot \rho_{brine}) \quad (2.5)$$

where $\rho_{shale} = 2.75 \text{ g cm}^{-3}$ and $\rho_{sand} = 2.67 \text{ g cm}^{-3}$ is the density of shale and sandstone rock, respectively, and Λ is the fraction of the sandstone pore space that is occupied by CO₂. The values for ‘nominal-CO₂’ scenario then correspond to $\Lambda = 0.5$ and the ‘extreme-CO₂’ corresponds to $\Lambda = 1$.

A more detailed numerical model of CO₂ injection and its subsequent diffusion through the geological repository has been developed by Darren Lincoln, University of Sheffield. The model describes the density evolution around the point of injection - the base of L3 for the geometry considered in this study - as a function of time. The model is based on the approach described in [85], [86] and [87]. When running muon simulations, it is convenient to break up the plume formations into discrete time intervals such that a fixed number of muons corresponding to the length of each interval are propagated through a stationary geometry. The radial extent of the plume, $r \propto \sqrt{t}$ [88], where t is the time since the start of injection. As such, the n^{th} time

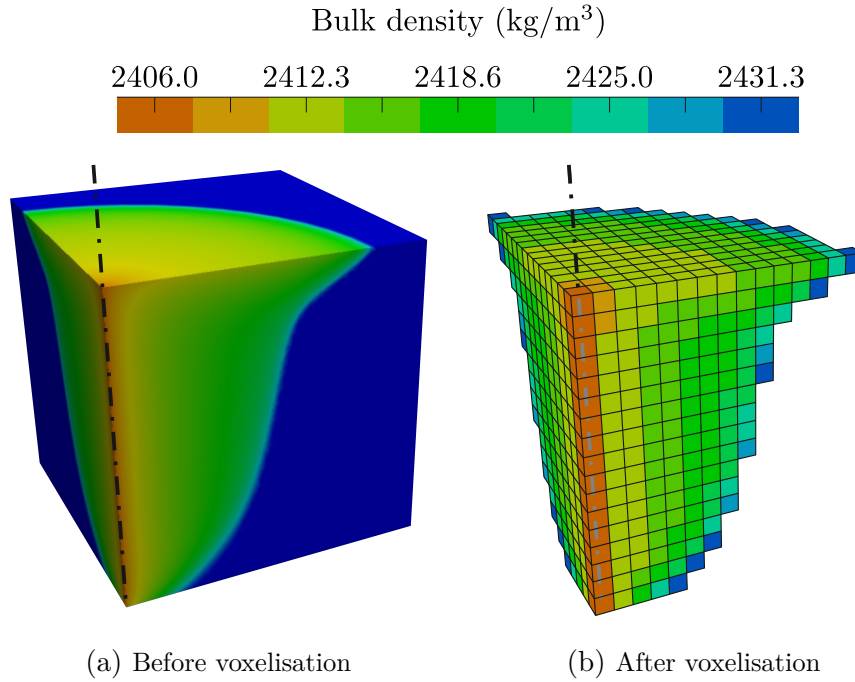


Figure 2.12: A quarter-symmetric rendering of the density profile of the injection region predicted after 64 days [15]. The output from the numerical model is shown in (a) and the corresponding voxelisation, which is overlaid onto the physical Geant4 geometry, is shown in (b). The injection point in both (a) and (b) is at the bottom of the dashed black line.

period represents $(2n-1)^2 \leq t$ (days) $\leq (2n+1)^2$ so that the radial extent of the plume increases linearly with $n = 1 \rightarrow 10$.

The model is implemented in the simulation geometry using the voxelisation capabilities of Geant4. A regular grid of cubic voxels, each $10 \times 10 \times 10$ m, is overlaid onto the finite element mesh that describes the density profile of the reservoir. The voxels are then parameterised using the composition and density outputs, which are interpolated from the mesh at the center points of each voxel. Figure 2.12 shows a quarter-symmetric rendering of the CO_2 saturated rock, as predicted by the model, 64 days after injection. The voxel grids for each time interval are subsequently superimposed on top of the geometry model in Geant4.

2.1.6 Analysis and results

In Section 2.1.5, two models were proposed to describe the changes in density of the subsurface after CO_2 injection. The pre-injection scenario is identical in both models, so the same simulation data can be reused for both analyses. The post-injection

scenarios rely on different muon simulations in which the physical parameters that describe L3 have been changed. For the simplest model, approximately 30 live days of statistics have been collected for both the ‘nominal-CO₂’ (density of the injection layer $\rho = 2.478 \text{ g cm}^{-3}$) and ‘extreme-CO₂’ ($\rho = 2.463 \text{ g cm}^{-3}$) scenarios. For convenience this will be referred to from now on as ‘model 1’. The detailed plume model, which will be referred to as ‘model 2’, considers the density distribution of the storage region up to 441 days after injection begins, and therefore muon statistics corresponding to this number of live days have been simulated. It is important to note that both models describe the specific case of CO₂ injection into the reservoir that has been chosen for this study. For other sites that have a different type of geology, depth and/or storage capacity the results may be different but the overall picture should remain the same. This will be discussed in more detail in Section 2.1.8.

The underlying parameter that is used to determine a change in density - and therefore the presence of CO₂ in the reservoir - is the muon intensity measured by the detector array. The muon count is subject to statistical fluctuations, and so the total number of muons observed before and after the CO₂ injection must be large enough to indicate a statistically significant change in the muon flux. There are also systematic uncertainties, not only related to the present study involving simulations, but also for real muon detectors. The description of the muon spectrum at the surface, the accuracy of the geocellular model, and the muon propagation in Geant4 all introduce systematic error on the muon count obtained from simulations for any given density scenario. However, the effects are present for all simulations, and will produce the same deviation from the ‘true’ muon count in two independent datasets. This is the case for all density values that are used in these studies to describe the CO₂ injection layer. One can therefore conclude that, when comparing the muon intensities in different scenarios to the baseline ‘no-CO₂’ measurement, taking the difference between the two muon counts will mean the systematic errors from both measurements will cancel.

Table 2.2 shows the calculated muon fluxes for ‘model 1’ in the pre-injection and two post-injection scenarios after the equivalent of ~ 8 days of muons are simulated. The errors on these intensity values are statistical, and do not take into account any systematic effects. Based on the predicted fluxes after 8 days, there is a clear, statistically significant change in the muon count for both scenarios, which indicates that the presence of CO₂ in the reservoir is resolvable.

Using the data obtained from the simulations of ‘model 1’, a more realistic picture of CO₂ emplacement can be mimicked by only considering muons in the post-injection

Table 2.2: The global muon intensity at the detector region for different bulk density values of the sandstone storage layer.

Scenario	Layer density (g cm ⁻³)	Flux (10 ⁻⁷ cm ⁻² s ⁻¹)
No-CO ₂	2.500	2.3143 ± 0.0019
Nominal-CO ₂	2.478	2.3527 ± 0.0019
Extreme-CO ₂	2.463	2.3682 ± 0.0019

scenarios that arrive at the detector site within a finite solid angle. As examples, two such volumes are considered and are defined as:

- **Narrow volume:** $28^\circ < \theta < 42^\circ$, $72^\circ < \phi < 144^\circ$, $d\Omega = 0.04$ sr
- **Wide volume:** $28^\circ < \theta < 56^\circ$, $72^\circ < \phi < 216^\circ$, $d\Omega = 0.29$ sr

where θ and ϕ are the muon zenith and azimuthal angles, respectively, at the detector site, and $d\Omega$ is the corresponding solid angle. For muons outside of these regions, a random Gaussian fluctuation is applied to represent the variations in muon counting.

Figure 2.13 shows the difference in muon intensity between the ‘no-CO₂’ scenario in comparison to the ‘nominal-CO₂’ and ‘extreme-CO₂’, scenarios for both narrow volume and wide volume injection cases. The plots are parameterised in terms of the number of statistical standard deviations between two independent muon counts, S , which is defined as:

$$S = \frac{|N_A - N_B|}{\sqrt{\sigma_A^2 + \sigma_B^2}} \quad (2.6)$$

where N_A and N_B are the number of muons collected at the detector site for two cases ‘A’ and ‘B’ and $\sigma_A = \sqrt{N_A}$ and $\sigma_B = \sqrt{N_B}$ are the associated statistical uncertainties. It is worth restating that the systematic uncertainties associated with N will cancel when taking the difference between the values for the two independent cases ‘A’ and ‘B’. In these figures, the muon zenith angle is plotted along the radius of the circles, and the azimuthal angle is plotted anti-clockwise from the direction pointing right. The density changes due to the emplacement of the CO₂ plume in the narrow volume and wide volume regions of the geometry appears clearly as a change in the intensity of muons arriving at the detector having passed through those regions.

Figure 2.14 shows the difference in total muon count integrated over all angles, ΔN_μ between the ‘no-CO₂’ case and the ‘nominal-CO₂’, and ‘extreme-CO₂’ cases for

Table 2.3: The muon flux, ψ_μ , at various time intervals T since injection and the associated significance S of the change in ψ_μ relative to the pre-injection scenario. The error values are statistical uncertainties in the muon count.

T (days)	Flux (10^{-7} cm $^{-2}$ s $^{-1}$)	S
1–9	2.3185 ± 0.0018	0.98
9–25	2.3236 ± 0.0013	3.9
25–49	2.3278 ± 0.0010	24
49–81	2.3302 ± 0.0009	32
81–121	2.3348 ± 0.0008	40
121–169	2.3382 ± 0.0007	48
169–225	2.3410 ± 0.0006	56
225–289	2.3426 ± 0.0006	64
289–361	2.3443 ± 0.0006	72
361–441	2.3461 ± 0.0006	80

muons detected with angles according the ‘wide volume’ definition defined above. Also plotted are the required values of ΔN_μ to achieve a 3σ , 4σ and 5σ significance. Both scenarios achieve $S > 5$ after a few days of exposure.

The muon simulation data obtained using ‘model 2’ uses a similar analysis strategy, whereby the presence of CO₂ is inferred directly from changes in muon intensity. The total muon intensity at the detector site, expressed in terms of the significance S given in Eq. (2.6), is given in Table 2.3 for each time interval since injection.

The angular distributions of S for ‘model 2’ are shown in Figures 2.15 and 2.16 for each successive time interval up to the total 441 days of simulated statistics. The plume distribution is visible over a background of statistical muon fluctuations after just 25 days.

2.1.7 Muon detection efficiency

An important assumption in the results presented here is that there is no background noise from instrumentation or local radioactivity. Adequate suppression of background signals can be achieved by requiring a minimum number of scintillator bars, N_{bar}^{hit} , to register a coincident signal. This condition will identify muons that traverse several bars, over the local background signals. A full study of the radioactive backgrounds for the borehole detectors will be presented in Section 3.2. The efficiency with which muons satisfy the trigger condition on N_{bar}^{hit} is dependent upon the arrangement of the scintillator bars within the container and the overall coverage of containers in the 1000

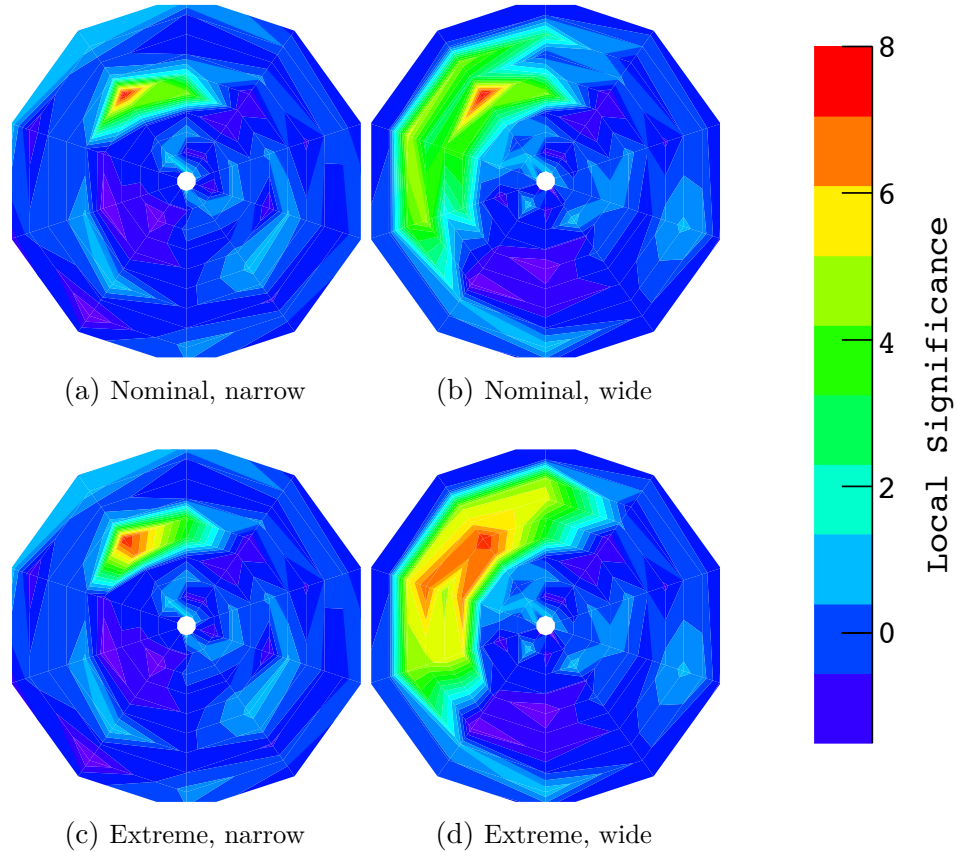


Figure 2.13: The change in muon count due to the constant injection of CO₂ parameterised as the significance factor, S . For the ‘extreme’ injection scenarios ~ 45 live days of statistics are shown and for the ‘nominal’ injection scenarios ~ 30 live days of statistics are shown. Each distribution shows S for muons detected with a zenith angle, θ (plotted radially) and azimuthal angle, ϕ (plotted anti-clockwise with $\phi = 0^\circ$ pointing to the right). In total there are 100 angular bins, with widths $\Delta\theta = 7^\circ$ and $\Delta\phi = 36^\circ$. A linear interpolation has been applied between adjacent bins.

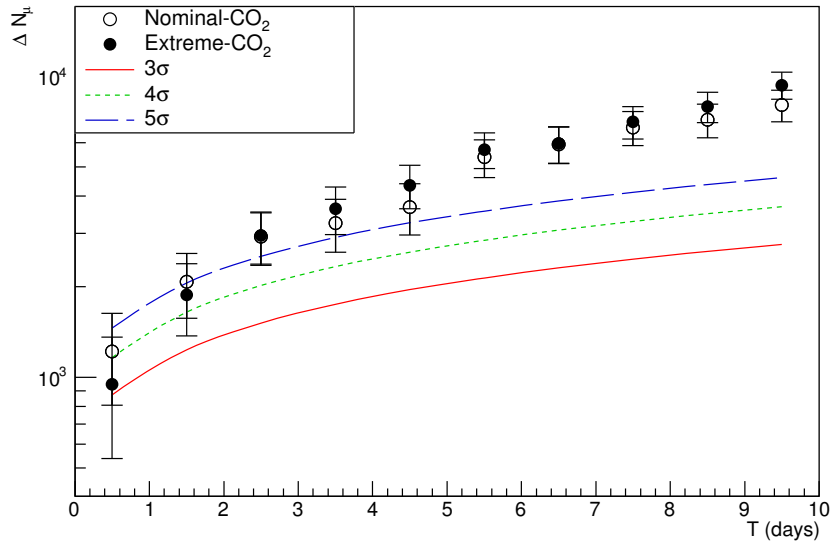


Figure 2.14: The difference in total muon count, ΔN_μ between the ‘no- CO_2 ’ and the ‘nominal- CO_2 ’, and ‘extreme- CO_2 ’ scenarios as a function of time since injection, T . The required values of ΔN_μ to achieve a 3σ , 4σ and 5σ value of S are also shown.

m^2 instrumented region considered in these studies. To quantify the acceptance of muons, A , two parameters F_{det} and N_{bar} are defined as the fraction of the 1000 m^2 detectable region that is covered by borehole detectors and the number of scintillator bars inside each borehole detector, respectively. Two values for each parameter are considered:

- F_{det} - ‘loose’ $\sim 50\%$, ‘tight’ $\sim 75\%$.
- N_{bar} - ‘loose’ = 16, ‘tight’ = 24.

The choices of F_{det} have the effect of scaling the total number of detected muons at the detector site. Possible arrangements of detector bars inside the containers for the chosen values of N_{bar} are presented in Figure 2.17. The acceptance, A of muons for each of these cases, is shown in Figure 2.18. The effect of the geometrical acceptance is to scale the results for S presented in Section 2.1.6 by a factor of \sqrt{A} .

2.1.8 Discussion

The results presented in Section 2.1.6 suggest that muon tomography can be successfully employed as a monitoring technique for a CCS site similar to the one considered in

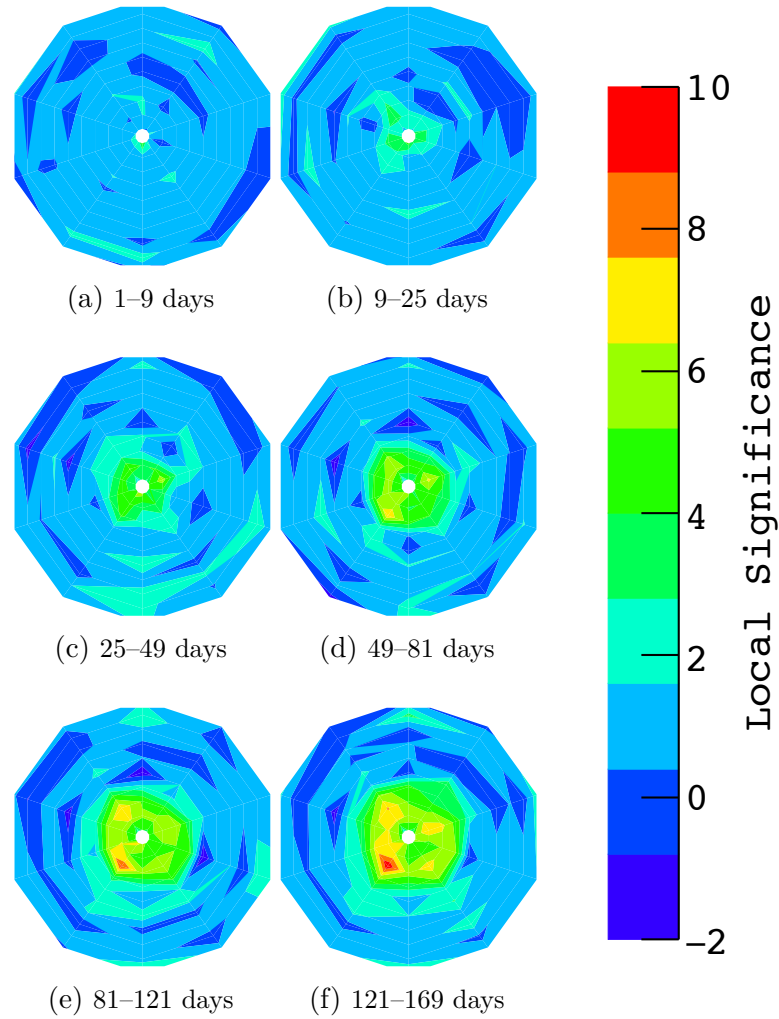


Figure 2.15: The change in muon count due to the constant injection of CO_2 parameterised as the significance factor, S . The caption for each contour plot shows the time interval since the start of CO_2 injection. Each distribution shows S for muons detected with a zenith angle, θ (plotted radially) and azimuthal angle, ϕ (plotted anti-clockwise starting from the right). In total there are 100 bins, with a bin width $\Delta\theta = 7^\circ$ and $\Delta\phi = 36^\circ$. A linear interpolation is made between adjacent bins.

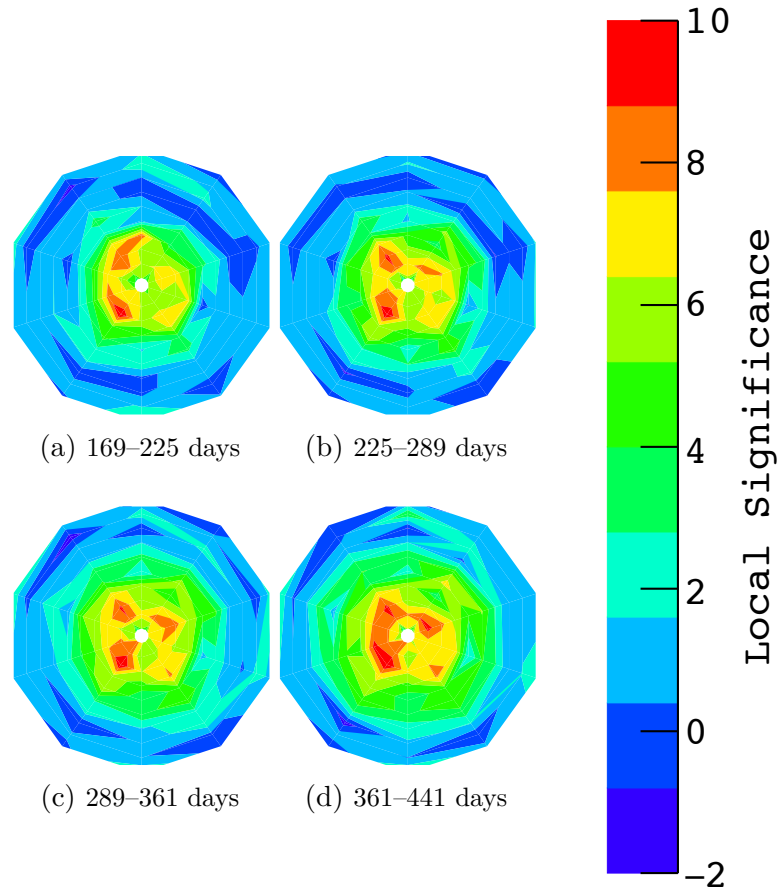


Figure 2.16: The change in muon count due to the constant injection of CO_2 parameterised as the significance factor, S . The caption for each contour plot shows the time interval since the start of CO_2 injection. Each distribution shows S for muons detected with a zenith angle, θ (plotted radially) and azimuthal angle, ϕ (plotted anti-clockwise with $\phi = 0^\circ$ pointing to the right). In total there are 100 angular bins, with widths $\Delta\theta = 7^\circ$ and $\Delta\phi = 36^\circ$. A linear interpolation has been applied between adjacent bins.

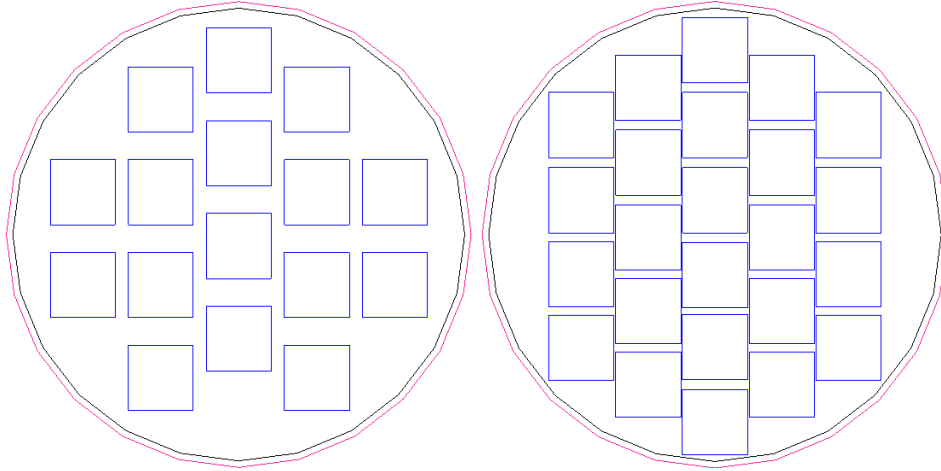


Figure 2.17: The arrangement of bars inside the borehole container that are considered for the efficiency calculations. The ‘loose’ packing (left) comprises 16 bars and the ‘tight’ packing (right) comprises 24 bars.

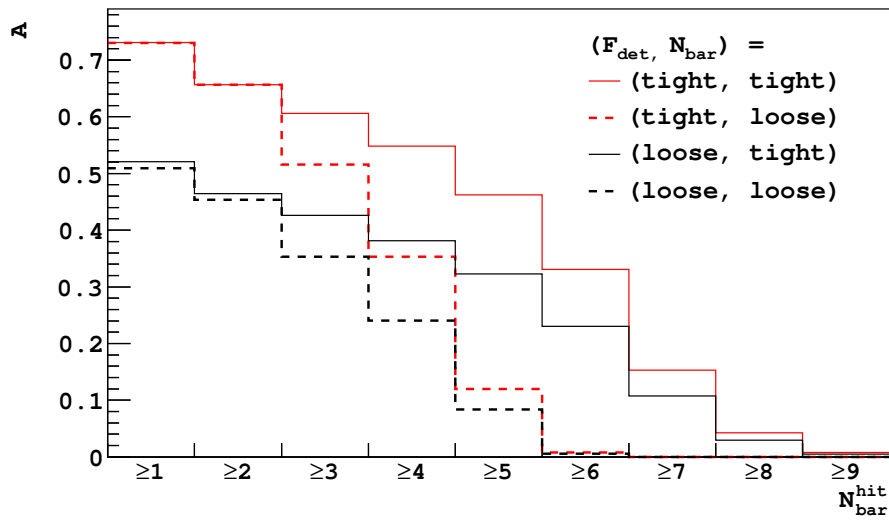


Figure 2.18: The acceptance, A , of muons that are recorded over the detector region for different combinations of the detector fraction, F_{det} , and the number of bars per detector, N_{bar} . A is plotted as a function of the number of bars that are traversed by a muon, N_{bar}^{hit} .

this study. Even if the acceptance of muons, discussed in Section 2.1.7, is only $\sim 5\%$, there is still a significant change in the global muon intensity due to CO_2 injection after 49 days. Additionally, it is clear from the contour plots presented in Figures 2.15 and 2.16 that CO_2 localisation to a small region is resolvable.

One of the biggest factors affecting the sensitivity of muon tomography is the depth of the detector array. For deep sites, the muon intensity will be lower and therefore longer exposure times are required to detect significant changes in the muon count. The site considered in this study is shallow; injection is considered at a depth of ~ 800 m and the thickness of the sandstone layer is ~ 400 m. The storage reservoir at Sleipner field is ~ 0.8 - 1.1 km below the sea bed and the depth of the water is ~ 110 m. This suggests a detector site which is ~ 400 m below that used in this study, which corresponds to a reduction in the muon flux of $\sim 85\%$ [8]. This would reduce the significance, S , in the results from Section 2.1.6 by a factor of ~ 0.39 , which does not drastically change the conclusions of this study.

2.2 Muon simulations for underground laboratories

While cosmogenic muons that survive underground are a signal for studies involving geological repositories, they are an important background for underground experiments seeking to observe rare events. The muons themselves may be readily detected and rejected, but their interactions in rock or other materials surrounding the detector may induce secondary particles that can mimic signal events. In this section, simulations of the muon-induced background for the underground laboratory at the Sanford Underground Research Facility (SURF) and the LUX-ZEPLIN (LZ) experiment will be discussed. It is important that the muon-induced background is quantified as accurately as possible using detailed simulations to understand whether a particular experiment, such as LZ, can reach its sensitivity goals using a proposed detector design. Having already built a model for transporting muons through a geological repository, a similar approach can be applied for the transportation of muons at an underground laboratory. For the studies presented in this section, it is convenient to split the simulation into two stages. In the first stage, muons are transported from the surface to the Davis campus², located 4850 ft underground at the Sanford Underground Research Facility

²The Davis campus is the same cavern that housed the Homestake experiment, which successfully detected and counted solar neutrinos for which Raymond Davis Jr. was later awarded the noble prize for physics. The cavern was also used for the LUX dark matter experiment.

(SURF). The procedure is similar to that described in Section 2.1, where the muon simulations were carried out for a geological repository. In the second stage these muons are transported through the remaining part of the cavern rock and the LZ detector geometry. The muons and all induced secondary particles are tracked and their interactions in the detector volumes are recorded for further analysis.

2.2.1 Underground muon spectrum at SURF

The initial transport of muons to an underground location is performed using the code MUSIC [49, 8]. MUSIC is a simulation code that deals specifically with the propagation of muons through large thicknesses of materials, accounting for muon energy loss due to four processes: ionisation, bremsstrahlung, electron-positron pair production and photonuclear interactions. This initial transport of muons neglects the fate of secondary particles, since they will be absorbed in rock before reaching the depth of the underground laboratory. The output of the MUSIC code is then combined with another code called MUSUN (MUon Simulations UNderground) [8], which is able to sample the muons at an underground location taking into account the muon spectrum at sea level and the configuration of the underground lab.

Muons with various initial energies have been propagated through the SURF rock using MUSIC. The average rock composition has been calculated as $\langle Z \rangle = 12.09$ and $\langle A \rangle = 24.17$ [22], where $\langle Z \rangle$ is the mean atomic number and $\langle A \rangle$ is the mean atomic mass number. MUSIC outputs the energy distributions as a function of distance travelled in the rock for muons with varying initial energies. In these simulations, the initial muon energies range from 100 GeV to 10^7 GeV and the distances range from 100 m w. e. to 15000 m w. e. The energy distributions are then convolved with the muon spectrum at the surface, which is given in Eq. (1.6), to generate three data files:

- **muint.dat** - the logarithm of muon intensity for different values of the zenith angle θ and azimuth angle ϕ in units $\text{cm}^{-2} \text{sr}^{-1} \text{s}^{-1}$.
- **musp.dat** - the muon energy spectra for different values of θ and rock thickness d .
- **depth.dat** - the slant depths from the surface to the underground location as a function of θ and ϕ . For SURF, this distribution has been provided by Martin Richardson, University of Sheffield [89]. It is based on a satellite-generated map

of the surface elevation of a $20 \times 20 \text{ km}^2$ region above the laboratory, which is shown in Figure 2.19.

The data files listed above are read in by the MUSUN code to sample muons on a geometrical surface that surrounds the detector geometry. The muon intensity, $I(\theta, \phi)$, for each angular bin is read from **muint.dat** file and the spectrum is integrated over solid angle and surface area. By iterating through each angular bin, a 2D cumulative distribution of the muon intensity as a function of θ and ϕ is then generated. A muon angle is sampled from this distribution, and the distance to the surface is read from the slant depth distribution contained in the **depth.dat** file. Finally, the muon energy is sampled from the **musp.dat** file for the selected angle and depth. What follows is a spectrum of muons at a depth (d), $I(E, \theta, \phi, d)$, that is specific to a particular underground location. Figure 2.19 shows the azimuthal distribution of muons for a spherical detector with a unit cross-sectional area. The peaks and troughs in the muon azimuthal distribution can be seen as corresponding troughs and peaks in the surface elevation of the region surrounding Davis cavern, which is shown in Figure 2.19. The ‘open cut’, an old open cast gold mine, is visible on the satellite map shown in Figure 2.19 and in the muon azimuthal distribution as a peak at $\phi \sim 170^\circ$. The distribution of muons for a specific cavern and detector configuration will be presented in Section 2.2.3. The vertical muon flux, as calculated by the MUSIC/MUSUN code, is $5.18 \times 10^{-9} \mu \text{ s}^{-1} \text{ cm}^{-2} \text{ sr}^{-1}$ and the total muon flux is $6.16 \times 10^{-9} \mu \text{ s}^{-1} \text{ cm}^{-2}$. These values should be treated with caution, since there may be significant uncertainties and variations in the composition and density of the rock overburden. Nevertheless, the value for the vertical flux is in good agreement with the measurement performed with the veto system of the Davis’ experiment [90]: $(5.38 \pm 0.07) \times 10^{-9} \text{ cm}^{-2} \text{ s}^{-1} \text{ sr}^{-1}$. Recently, the total muon flux was measured at SURF by the Majorana Demonstrator veto system [70]. The detector is at the 4850 ft level, which is the same depth as the Davis cavern, but is in a slightly different location. The total muon flux is $(5.31 \pm 0.17) \times 10^{-9} \mu \text{ s}^{-1} \text{ cm}^{-2}$. The discrepancy with the global flux value from MUSIC/MUSUN is $< 15\%$, which indicates the muon model produced for these simulations is reasonably accurate.

2.2.2 Muon generator for the LZ simulation software

Simulations to transport muons to an underground site are the first step in muon-induced background studies. In the second stage, the muon model obtained from these simulations needs to be passed to the software package used to generate events in a

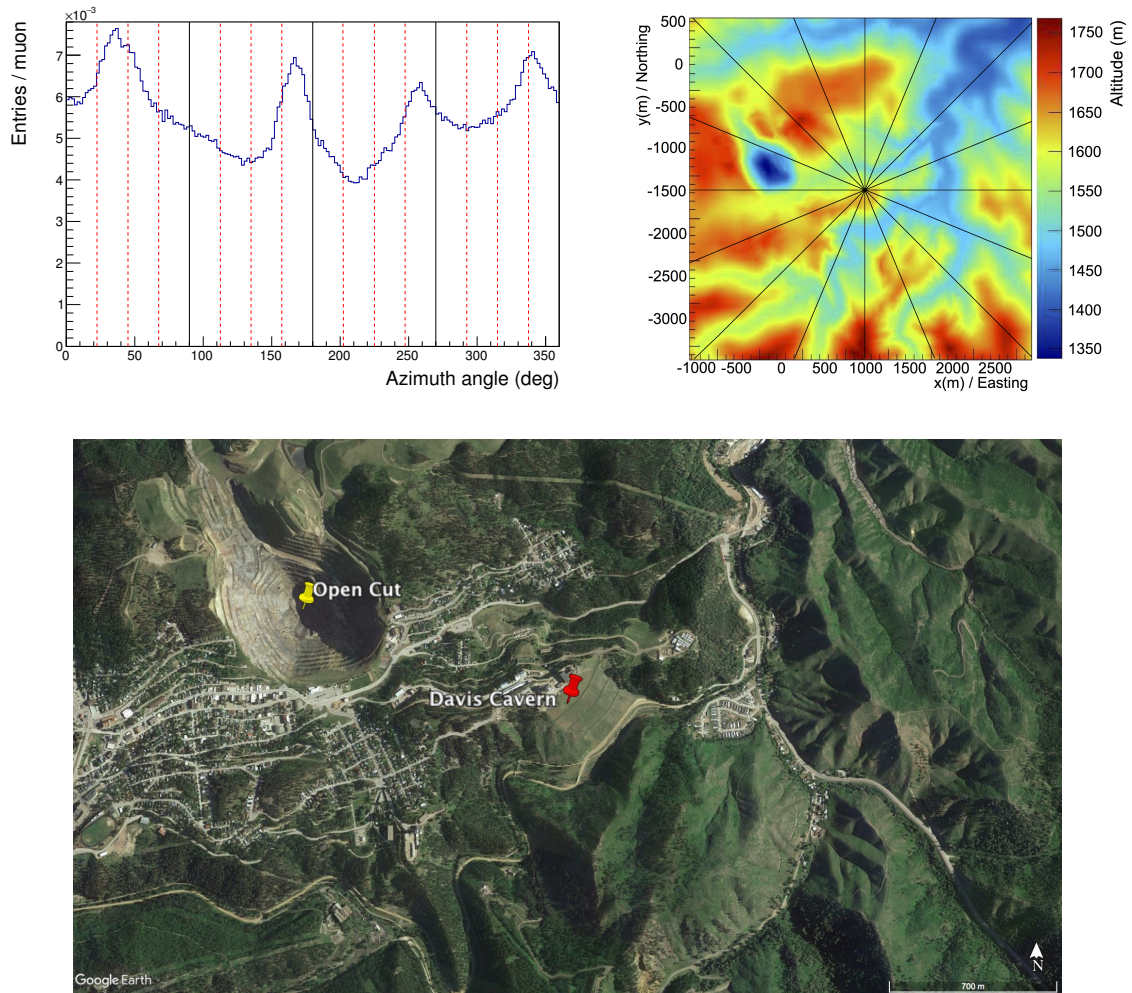


Figure 2.19: Top left - The muon azimuth angle ϕ distribution at the Davis campus integrated over θ . The vertical lines show 22.5° divisions for comparison with the surface altitude profile shown in in the top right. On this map, ϕ is defined counter clockwise with $\phi = 0$ at east (the direction pointing to the right). One can match, by eye, the peaks in the azimuth angle distribution with regions of low altitude in the surface map. Bottom - a satellite image of the region above the Davis cavern. The prominent feature on all three figures is the ‘open cut’, which appears as a blue region on the altitude map and as a peak in the azimuthal distribution at $\sim 170^\circ$.

detector. For simulations of muon-induced backgrounds for the LZ experiment, muons are generated and propagated through the detector geometry using the LZ simulation software. To date, two simulation Monte Carlo codes have been used for background studies; LUXSim [91] and its successor, BACCARAT. Both codes are based on C++ and are built on top of the Geant4 engine for transporting particles through materials. While the physics involved is essentially identical and similar to that used for geological repositories, BACCARAT is organised such that parts of the code that are specific to a particular experiment, such as the geometry, are independent from the ‘main’ code that deals with physics, inputs and outputs, event generation etc. In this way, BACCARAT has the flexibility to be used by different experiments that require the same approach to simulations for low background, rare-event searches. For example, BACCARAT can also be used to simulate muon and background events in geological repositories, but unfortunately the development and validation of the code came later when the simulations for carbon storage monitoring, described in Sections 2.1 and 3.2 of this thesis, had already been completed. BACCARAT and LUXSim have a ‘component-centric’ approach to simulating and recording events. At run-time, a user is able to distribute a particle source within any part of the detector geometry with a specified activity. This is best illustrated by the macro command used to invoke a particle generator:

```
/LUXSim/source/set A B C D E F
```

where A = geometry component (where the source is located)
 B = source type e.g. a radioactive isotope
 C = numerical activity
 D = units of activity
 E = energy (if generating a single particle e.g. a neutron source)
 F = energy units

Any number of sources can be simulated in a single run by writing the source command multiple times. Additionally, the user is able to assign record levels to different parts of the geometry. These record levels determine how much information is saved when a particle track passes through a geometry volume.

For the studies presented in this thesis, the original MUSUN code, which was written in Fortran, has been converted to C++ and implemented in the LUXSim and BACCARAT codes as a ‘particle generator’. While the component-centric approach of

the event generation in LUXSim and BACCARAT is especially useful for distributing radioactive sources throughout detector components, the setup is not suitable for particles that are generated independently of detector volumes e.g. cosmic-ray muons. Changes have been made to LUXSim and BACCARAT to accommodate a volume independent generator, allowing the positions of the muons to be determined directly from the MUSUN sampling code. In addition, as the underground muon flux is constant and independent of the contamination in other detector components, the requirement to set a source activity with the muon generator has been removed. To use the generator for a simulation, one simply needs to specify the number of muons that should be simulated. The appropriate normalisations, taking into account the flux of muons over the surface of the cuboid, can then be applied in post-processing based on the number of simulated events.

2.2.3 Validations

The best way to validate the implementation of the muon generator is to compare the initial spectra of muons with the results of running the original MUSUN code as a stand-alone program. Figures 2.20-2.23 show a comparison of energies, azimuthal angles, direction cosines and positions for 10^7 muons generated using the two codes.

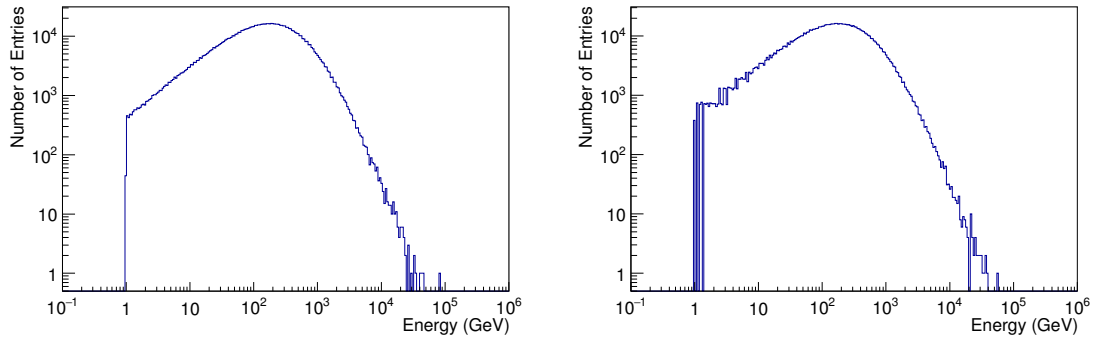


Figure 2.20: The energy spectra of muons generated in LUXSim (left) and the stand-alone MUSUN code (right). The apparent discrepancy at low energies (< 10 GeV) is an effect of binning on the output from MUSUN, which writes energies to the nearest 100 MeV.

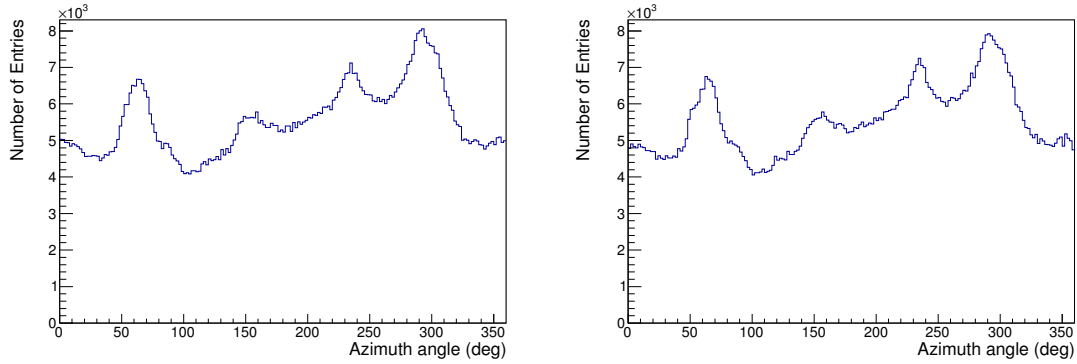


Figure 2.21: The distribution of azimuth angle ϕ for muons generated in LUXSim (left) and the stand-alone MUSUN code (right). This distribution takes into account a specific cavern configuration (see Section 2.2.4) and is therefore different from the distribution shown in Figure 2.19.

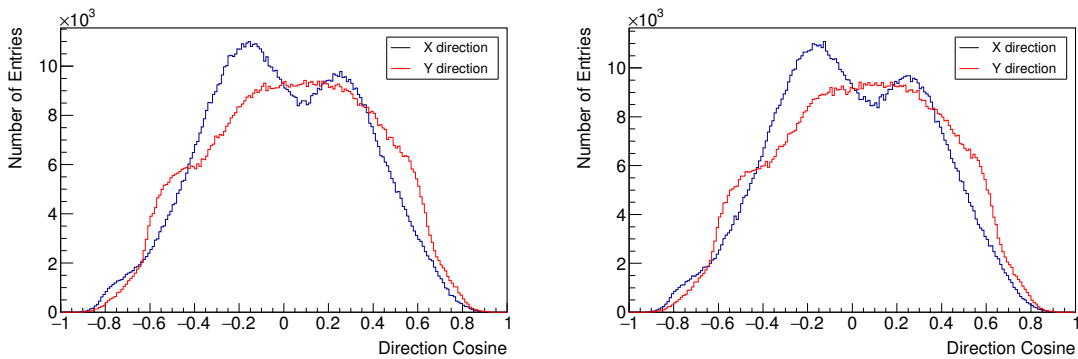


Figure 2.22: Direction cosines in the x -direction and y -direction of muons generated in LUXSim (left) and the stand-alone MUSUN code (right).

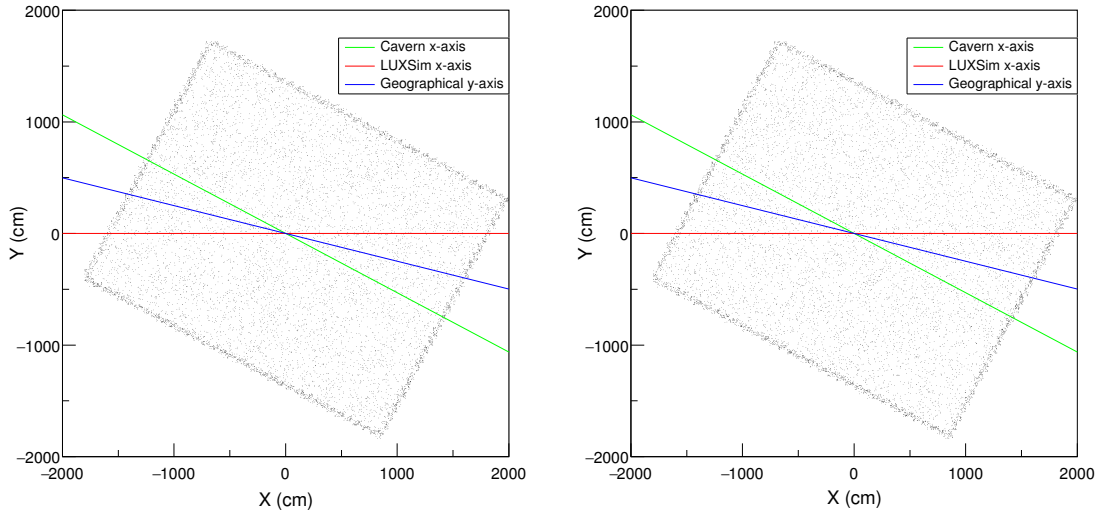


Figure 2.23: The x - y positions of the muons generated in LUXSim (left) and the stand-alone MUSUN code (right). Muons are sampled on the surface of a cuboid that sits outside the Davis cavern (see Section 2.2.4). The relative alignment of the cavern, LUXSim and geographical (North-South) coordinate systems are also shown.

2.2.4 Transport of muons through the detector geometry

The muon interactions that are responsible for generating background particles have previously been described in Section 1.5.2. For this study, muons comprise the primary particles, and muon-induced particles are produced by Geant4 as secondaries from interactions of muons within the rock. Since Geant4 provides different models to treat physics processes, it is important to select ones that will correctly describe the production of neutrons and other particles from muons. Several studies of muon-induced backgrounds have been performed using Geant4 and the results have been compared with available data [75–78]. In recent distributions of Geant4, a modular physics list called `shielding` has been made available for underground and low-background applications. For the simulations of muon-induced backgrounds described in this thesis, the physics list within the LUXSim code has been changed to invoke the processes provided by the `shielding` list. The muon photonuclear interaction - which is not constructed by default in `shielding` - is built and registered as an additional physics process. A full description of the physics models are available in [92].

The thickness of rock through which the muons should travel before emerging from the rock surface and entering the cavern is also informed from previous studies of muon-induced backgrounds performed in [75]. 5 m of rock on all sides and beneath

the detector and 7 m of rock on top gives enough material to account for all particles produced by the muon interactions. Given these requirements, the muon generator samples muons within the Davis cavern rock on the surface of a cuboid measuring $30 \times 24 \times 24$ m. These dimensions are informed by the size of the cavern itself, which is shown in Figure 2.24. The cuboid extends from -14 m to +16 m pointing south, -12 m to +12 m pointing east and -11 m to +13 m vertically, assuming a coordinate system that is centered in the middle of cavern. In the simulation geometry, the coordinate system is actually centered on the middle of the cathode wire that separates the forward field and reverse field regions of the liquid xenon Time Projection Chamber (TPC). The actual coordinates used in the muon generator are therefore shifted upwards by 4.25 m. A further complication is the rotation of the simulation coordinate system. Figure 2.25 shows the relative alignment of three coordinate systems: the cavern, the simulation geometry and geographical coordinates. The data files (**muint.dat**, **musp.dat** and **depth.dat**), which take into account the surface profile at the SURF location, are defined with respect to a geographical coordinate system i.e. north-south-east-west. Given that muons are sampled on the surfaces of a cuboid that are parallel to the cavern surfaces, a translation is made to the cavern coordinate system before the muon cumulative distribution function is generated. Then, for each event, an additional translation is made after a muon is sampled to ensure that the muon positions and directions are fed into LUXSim/BACCARAT according to the simulation coordinate system.

The total muon intensity over the surface of the cuboid from which muons are generated is 0.0609 s^{-1} . To obtain a statistically significant limit on the number of background events from muon-induced particles, the simulation live time should be many times greater than this. It is therefore expected that something of the order of 10^8 muons should be simulated. This requires significant computing resources; based on a preliminary simulation of 10^4 muons the processing time is approximately 0.4 CPU seconds per primary muon. Consequently, the HEP cluster at the University of Sheffield is used to run many instances of the same simulation in parallel. This is possible since, after the code has been compiled, the same LUXSim/BACCARAT executable can be run multiple times, each with a different macro file specifying run options such as output directory, random seed, number of events etc. Each simulation ‘job’ uses one of the worker nodes that make up the HEP cluster and at the end of the simulation the output files, which are saved to the local disk of each node, are transferred to a central data disk that is then accessible from a single desktop machine

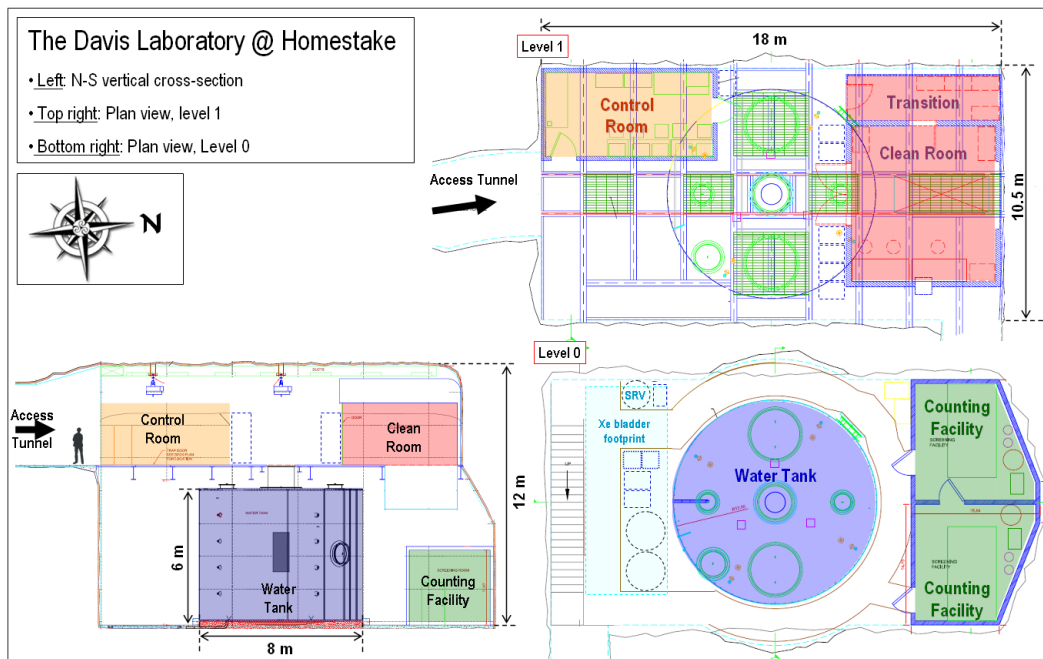


Figure 2.24: The layout of the Davis cavern at SURF. The size of the cavern is approximately 20 m running north-south and 14 m running east-west. The height is approximately 12 m. Note that the cavern is rotated approximately 14 degrees east from the north-south direction.

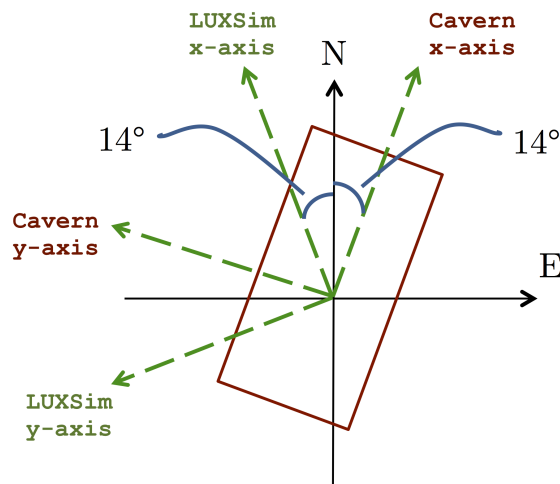


Figure 2.25: The alignment of the geographical directions with respect to the cavern coordinate system and the simulation - labelled 'LUXSim' - coordinate system. A representation of the cavern walls is marked out in red.

Table 2.4: Composition of the rock in the Davis Cavern according to [22].

Element	Abundance by weight (%)
Al	7.2
Ca	5.6
Fe	9.9
H	1.2
K	0.2
Mg	4.2
Mn	0.1
Na	2.1
O	48.4
P	0.03
Si	20.4
Ti	0.7

on the HEP cluster. In total, 2.3×10^8 muons have been simulated, which corresponds to ≈ 120 live years.

2.2.5 Adding cavern rock to the simulation geometry

Before transporting the muons through the detector geometry, the Davis cavern rock has been added to the simulation. As discussed in Section 2.2.4, the cavern measures $20 \times 14 \times 12$ m and should sit inside a cuboid of rock measuring $30 \times 24 \times 24$ m. The density of rock is 2.70 g cm^{-3} and the composition, which is also added to the simulation geometry, is summarised in Table 2.4. Figure 2.26 shows a visualisation of the cavern rock and water tank geometries. A steel pyramid volume, which will be present for the duration of the LZ experiment, is also shown. This pyramid was inserted into the rock during the construction of the LUX experiment to shield the detector from gamma-rays beneath the water tank.

2.2.6 LZ detection principles

Before discussing the analysis of the simulated data, it will be useful to give an overview of the LZ detector and the expected signals that will come from a WIMP interaction. The LZ detector is a two-phase xenon liquid/gas time projection chamber (TPC). Several experiments have utilised this technology for rare-event searches [64, 93–96] and the physics of particle interactions in these detectors has been studied and reviewed extensively [97–99, 18, 100]. The short summary that follows, which is intended to

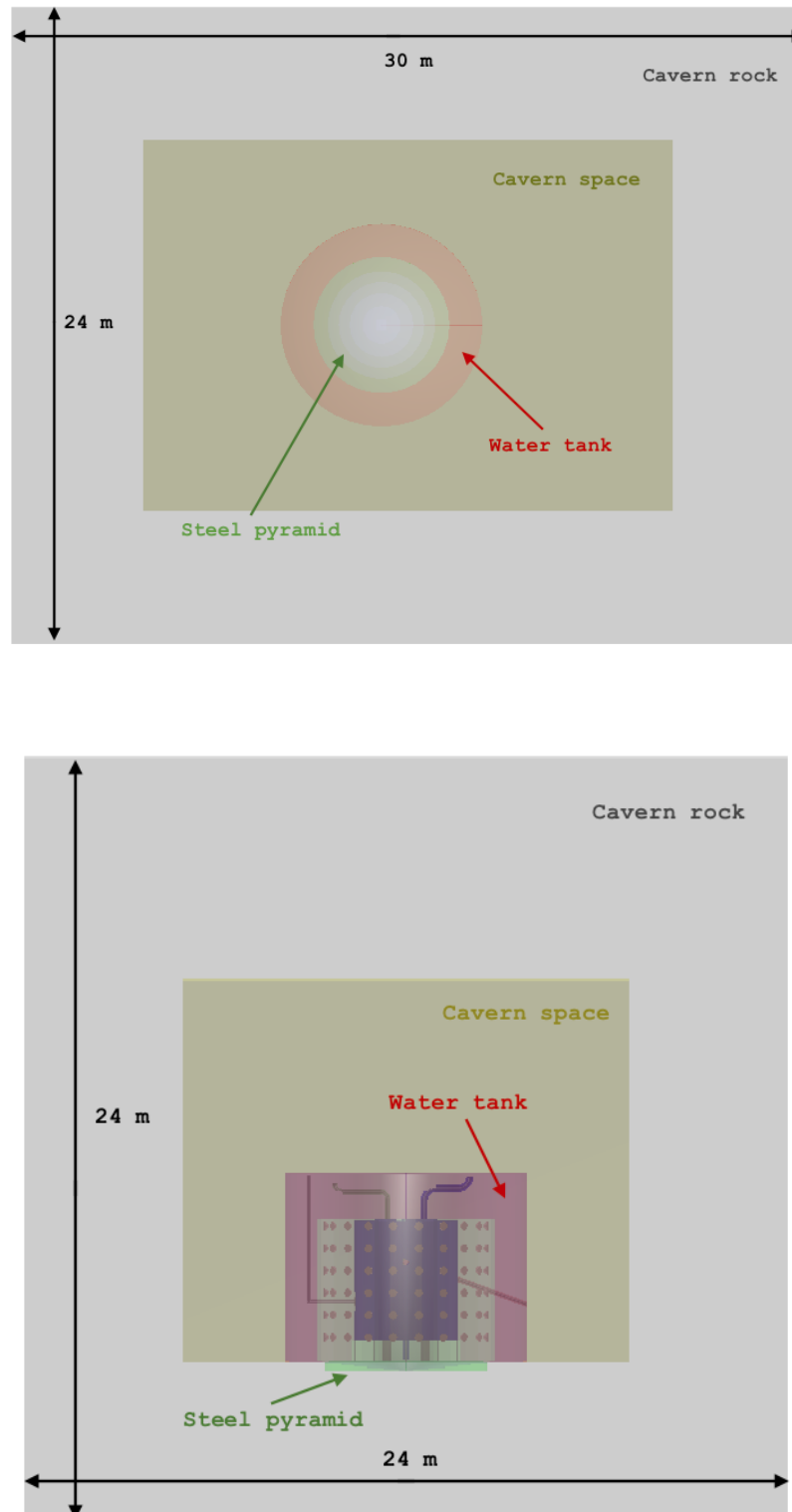


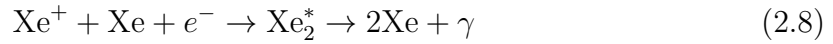
Figure 2.26: A visualisation of the simulation geometry showing a top-view (top figure) and a side-view (bottom figure) of the cavern rock (grey), the cavern space (yellow), the water tank (red) and the steel pyramid (green).

facilitate the description of the analysis procedures presented in Sections 2.1.6 and Section 3.3.5 of this thesis, is based on these references.

The aim of the LZ detector is to identify interaction sites within a target and determine as much as possible about the particle that produced the interaction. At low energies, when an incoming particle enters a liquid, it transfers its energy to an atomic electron or an entire atom, which subsequently recoils inside the target material. The former is referred to as an electron recoil (ER) and the later a nuclear recoil (NR). There are three ways in which this recoiling particle can then lose energy in the target medium; it can collide with atoms (generating heat), excite atoms (forming excitons) or produce electron-ion pairs via ionisation. The excited atom combines with a neutral atom to form a diatomic excited molecule, which subsequently produces scintillation photons as it de-excites:



The example shown here represents xenon (Xe) but the principle is the same for other noble elements that have been utilised in similar experiments, such as argon. Ionisation electrons may be extracted by an external electric field, but can also produce scintillation light if they recombine with positive ions:



The number of ionisation electrons (n_e) can be written in terms of the number of ionised atoms (N_i) and the recombination fraction (r) as:

$$n_e = (1 - r) \cdot N_i \quad (2.9)$$

Similarly, n_γ can be written as:

$$n_\gamma = N_{ex} + r \cdot N_i \quad (2.10)$$

where N_{ex} is the number of excited atoms produced in an interaction. In total, the number of detectable quanta that are produced in an interaction, $n_e + n_\gamma = N_{ex} + N_i$, is proportional to the amount of energy deposited. Given that liquefied noble gases have a band structure of electronic states, energy needs to be released in order to produce ionisation or excitation. Energy depositions can therefore be described as:

$$E = W \cdot (n_e + n_\gamma) \quad (2.11)$$

where E is the total energy deposited (less the energy lost to heat), and $W = 13.7 \pm 0.2$ eV [98] is the average energy required to produce a single excited or ionised atom. In reality, not all scintillation photons and ionisation electrons can be detected. The LZ detector, shown in Figure 2.27, shows the characteristics of a typical dual-phase liquid/gas TPC. It is designed to detect both the scintillation and ionisation signals from particle interactions in the liquid xenon. The prompt scintillation response - the ‘S1’ signal - is detected by arrays of photomultiplier tubes (PMTs) on the top and bottom of the TPC. The ionisation electrons are drifted by an electric field to the gas region at the top of the TPC, where they are extracted and undergo electroluminescence, producing a second scintillation light - the ‘S2’ signal - which is detected by the top array of PMTs. The S1 signal, in units of detected photons (phd) can be expressed as $S1 = n_\gamma \cdot g_1$, where g_1 is a factor that describes the geometric light collection efficiency of the detector and the PMT quantum efficiency. Similarly, the S2 signal can be expressed as $S2 = n_e \cdot g_2$, where g_2 describes the electron extraction efficiency and the number of photons detected per extracted electron. Values for g_1 and g_2 are obtained from detector calibrations, and this allows the total energy deposited in an interaction to be reconstructed from the measured S1 and S2 signals. Figure 2.28 shows the amount of S1 and S2 signal (normalised to energy) from several ER calibration sources deployed in the LUX detector [17]. This plot also demonstrates a corollary of Eq. (2.11); for a given energy deposition, more light production (higher n_γ) will mean less charge production (less n_e) and vice-versa.

In general, the relative size of the S1 and S2 signals is dependent on a number of factors; the type of interaction, its energy and the external electric field. This has been observed experimentally in a number of liquid noble detectors, as an example Figure 2.29 shows two populations of events arising from nuclear recoils (orange) and electron recoils (cyan) inside the LUX detector [18]. The LUX detector achieved an average $(99.6 \pm 0.1)\%$ discrimination of ERs and NRs based on the S1/S2 ratio at a 50% acceptance rate for nuclear recoils [64]. The electric field affects the sizes of the S1/S2 signal by decreasing the recombination fraction - in principle the applied field should be as high as possible so that the threshold energy for producing ionisation electrons that can escape recombination and produce an S2 signal is as low as possible.

The difference in charge and light yields for NRs and ERs is explained by the velocity of recoiling atoms with respect to electrons of the same energy. An atom with the same kinetic energy as an electron will have a smaller velocity due to its larger mass. It therefore loses energy via collisions with other atoms in the medium, which generates heat that is not detected in a TPC. Not only does this lead to an overall

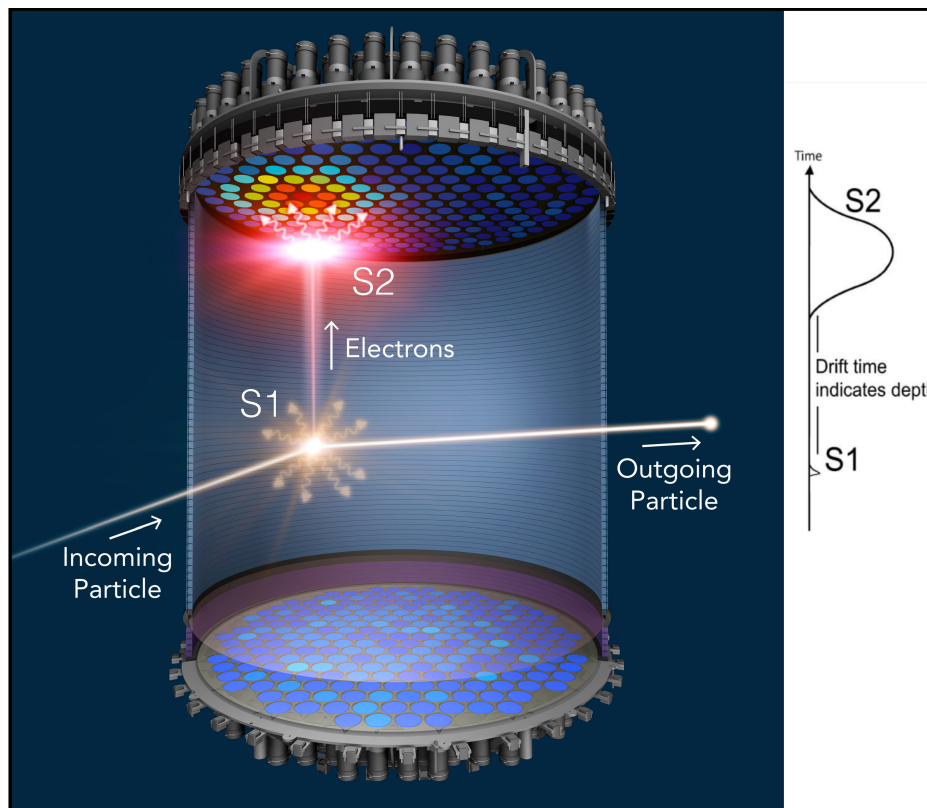


Figure 2.27: A representation of a particle interaction in the LZ TPC. An incoming particle produces prompt scintillation light ('S1') and ionisation electrons, which are drifted under the influence of an electric field to a gas region at the top of the TPC where they are extracted and undergo electroluminescence. The resulting photons are detected as a secondary pulse ('S2'). The time between these two signals indicates the depth of the event and the hit map on the top PMT array indicates the position in x - y . Figure adapted from [16].

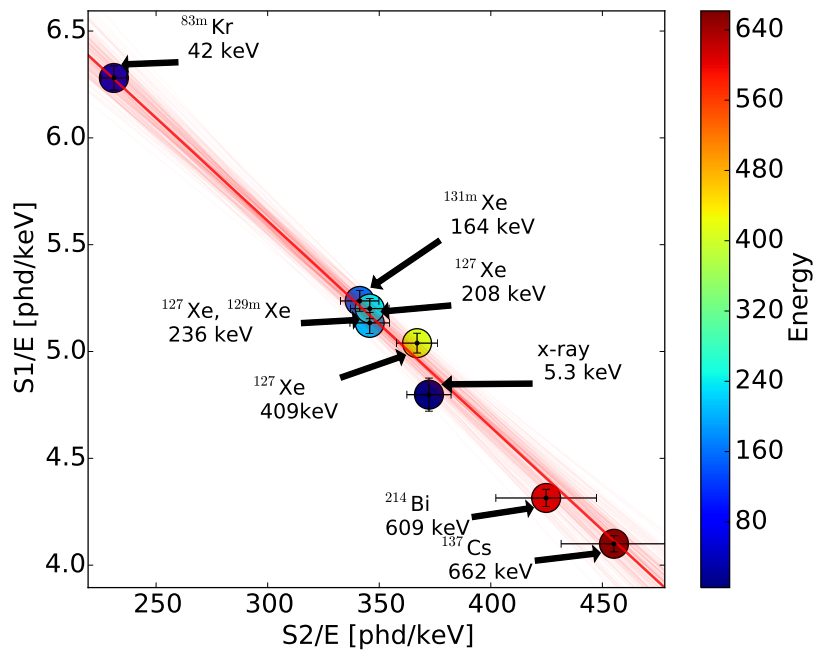


Figure 2.28: A plot of LUX calibration sources showing the anti-correlation between the amount of charge ('S2/E') and light ('S1/E') produced for each recoil event [17]. The units of 'S1' and 'S2' are detected photons (phd).

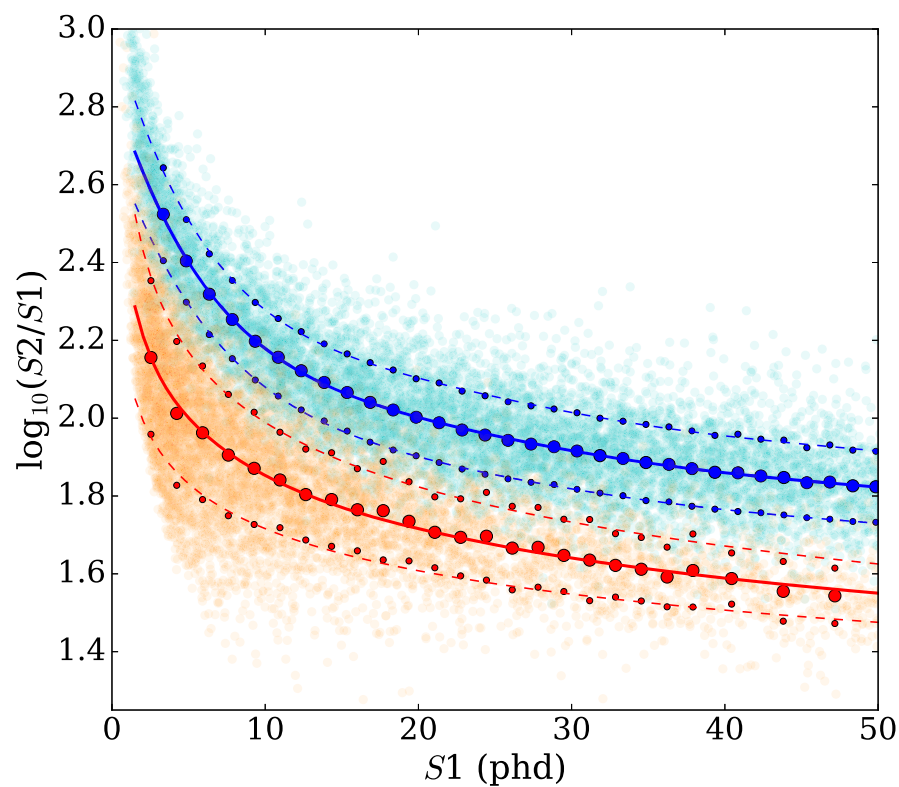


Figure 2.29: A discrimination plot of electron recoils (blue) and nuclear recoils (yellow) from calibration data [18]. The large filled circles show the mean of a fitted Gaussian and the small filled circles show the $\pm 1\sigma$.

quenching³ of the observable energy from nuclear recoils, but it also affects the fraction of $\frac{N_{ee}}{N_i}$, which is $O(0.1)$ for ERs and $O(1)$ for NRs. This manifests itself as a larger S2/S1 signal for ERs compared with NRs. Given the excellent discrimination power of liquid xenon, the analysis presented in later chapters will use truth information from Monte Carlo simulations to separate the two interaction types, ERs and NRs, based on the particle causing the interaction. While single NRs cannot be suppressed further, a 99.5% discrimination factor will be applied to the backgrounds from ERs - this is baseline for LZ [16].

In addition to the liquid xenon target, LZ will have of an outer detector (OD) and liquid xenon ‘skin’ - an optically segregated region of liquid xenon that is between the TPC and the inner cryostat vessel. All of these detectors will sit inside a water tank in the configuration shown in Figure 2.30. The OD is made up of a gadolinium-loaded liquid scintillator (Gd-LS) and together with the skin forms an integrated veto system that is able to tag and reject background events. If a WIMP scatters inside the central volume of liquid xenon, it will not be accompanied by a deposition of energy in the surrounding detector volumes because of its low interaction cross-section. Conversely, background events that can fake a WIMP signal will likely deposit some detectable energy in the central liquid xenon and the veto systems. Neutrons in particular are dangerous backgrounds since they produce nuclear recoils and are able to escape the TPC more easily than other background particles. The Gd-LS is designed to capture out-going neutrons and tag them as background. Gadolinium (Gd) is added to the scintillator to increase the neutron tagging efficiency - the abundances of isotopes in natural Gd and their corresponding thermal neutron capture cross sections are shown in Table 2.5. ^{157}Gd and ^{155}Gd have large cross sections, and the reaction releases several gammas with total energies of 7.9 MeV (^{157}Gd) or 8.5 MeV (^{155}Gd), which are subsequently detected by PMTs in the water tank. The remaining neutrons that are not captured by Gd are captured on hydrogen, releasing a 2.2 MeV gamma. The Gd also reduces the neutron capture time from $\sim 200 \mu\text{s}$ to $\sim 30 \mu\text{s}$, which helps reduce the overall dead-time of the detector.

³Due to the energy loss to atomic motion (heat) by nuclear recoils, only a fraction of the true recoil energy is observed in a liquid xenon TPC. It is useful to define two energy scales, measured in units of keV_{ee} , where ee stands for ‘electron-equivalent’ and keV_{nr} where nr stands for ‘nuclear recoil’. The conversion is approximately $E (keV_{ee}) = Q \cdot E (keV_{nr})$ where $Q \sim 0.25$.

Table 2.5: The abundances of isotopes of natural gadolinium and the thermal neutron capture cross-section for $Gd(n,\gamma)$ according to [23].

Isotope	Abundance (%)	Thermal capture cross-section (barns)
^{152}Gd	0.20	740
^{154}Gd	2.2	86
^{155}Gd	15	61 000
^{156}Gd	21	1.8
^{157}Gd	16	250 000
^{158}Gd	25	2.2
^{160}Gd	22	1.4

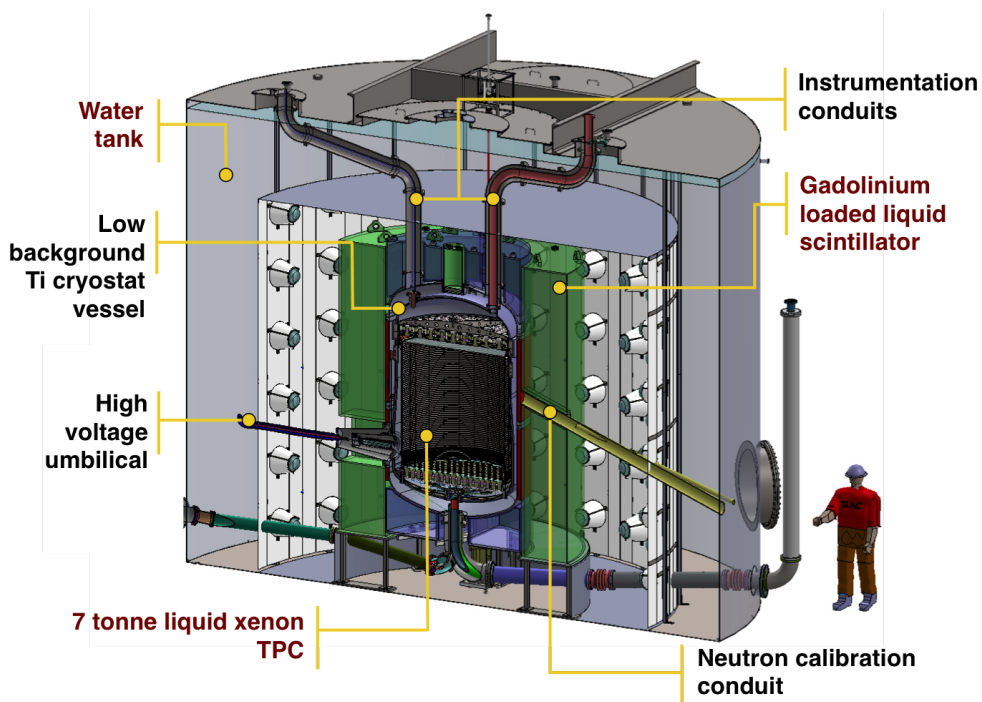


Figure 2.30: The arrangement of the LZ detector systems. Figure adapted from [16].

2.2.7 WIMP signals in LZ

The signature that direct detection experiments are seeking to observe is a nuclear recoil caused by the elastic scattering of a dark matter particle with an atom in the target material. The recoil energy spectrum is approximately exponential [101] - assuming a stationary detector in the galaxy it has the form:

$$\frac{dR}{dE_R} = \frac{R_0}{E_0 r} e^{-\frac{E_R}{E_0 r}} \quad (2.12)$$

where E_R is the recoil energy, R_0 is the total recoil rate, E_0 is most probable energy of a dark matter particle with mass M_D , $r = \frac{4M_D M_T}{(M_D + M_T)^2}$ is a kinematic factor for a target nucleus of mass M_T . Direct detection experiments are aiming to measure the recoil energy spectrum above some background. Given the shape of the spectrum, the greatest sensitivity to a dark matter signal is achieved by probing the smallest energy recoils possible. For M_D in the range 10-1000 GeV/ c^2 and assuming a galactic velocity of $10^{-3}c$, the recoil energies are in the range 0-100 keV. For the analysis presented in Section 2.2.8, an energy range of 1.5-6.5 keV for ERs and 6.0-30.0 keV for NRs is considered as the ‘region of interest’ for evaluating backgrounds. Below ~ 1.5 keV_{ee} or ~ 6.0 keV_{nr} the S1 signal has a less than 50% probability to be detected in the TPC. Above ~ 6.5 keV_{ee} the discrimination efficiency of ERs and NRs is high, so the ER background can be clearly identified whereas the NR background is suppressed due to an exponential form of the NR spectrum. For the purposes of comparing ER and NR backgrounds, an equivalent upper energy threshold (30 keV_{nr}) for NRs is used.

2.2.8 Post-processing and analysis

To understand the response of the LZ detector to the muon-induced background, the data is processed and analysed using a collection of ROOT-based C++ scripts. LUXSim collects information about each simulation event into a ‘record’, that is subsequently written to a binary file. After the simulation, this binary is converted to a ROOT file using a script called `LUXRootReader`. The script reads each block of data from the binary file and saves it into a ROOT ‘tree’, which comprises different ‘branches’ that represent parameters for each particle such as position, energy, particle type, interaction type etc. Due to the way in which LUXSim organises the events, one entry corresponds to a collection of particle interactions within a single volume for each event. As such, there may be multiple entries in the ROOT tree for each primary event. The ROOT file that is returned by the `LUXRootReader` script is processed further to group all interactions in all volumes occurring for the same event into a single entry. Some

additional processing occurs at this stage to reduce the size of the files. The following parameters are calculated for each event in each detector (scintillator, liquid xenon skin and the forward-field and reverse-field regions of the liquid xenon TPC ⁴) and written to a separate ROOT tree as a ‘reduced’ file:

- The energy-weighted position of events inside a volume, which is defined as

$$x = \frac{\sum_i x_i \cdot E_i}{\sum_i E_i} \quad (2.13)$$

where x represents each of the position coordinates (x, y, z) and i is an index for each individual energy deposition that makes up the event.

- The energy-weighted variance of the scatters, given by the formula

$$\sigma_x = \sqrt{\frac{\sum_i E_i \cdot \sum_i E_i (\mu - x_i)^2}{(\sum_i E_i)^2 - \sum_i (E_i^2)}} \quad (2.14)$$

where μ is the mean energy-weighted position for the event. As well as σ_z , the parameter $\Delta Z = Z_{\max} - Z_{\min}$ is also calculated as the difference between the maximum and minimum Z coordinate within an event.

- The time of the first energy deposition.
- The total energy deposition from nuclear recoils (those caused by the interaction of a neutron, proton or recoiling atom) and the total energy deposition from electron recoils (electrons, positrons or gammas). For simulations involving muons, the reduction code was edited to record the energy deposition from muons separately.

After the ‘reduced’ files are generated, they are processed through the main analysis program. Here, event selection cuts are applied to mimic those that will be applied in the real LZ experiment. The cuts are used to identify events that are indistinguishable from WIMP events, and therefore contributing to the background rate.

- The single scatter cut (SS) removes events that scatter multiple times in the liquid xenon TPC. WIMPs have a low interaction cross section with the target material and are therefore expected to scatter only once. This cut is based on the

⁴The TPC is broken down into two regions. The forward-field region defines the section of liquid xenon between a cathode and an anode, within which electrons drift upwards to the gaseous region of the detector. The reverse field region is between the cathode wire and the bottom of the TPC.

energy-weighted spatial distribution of the scatters, σ_x , as defined in Eq. (2.14). In LZ, the depth of the event (z) is determined by the time difference between the S1 and S2 pulses coming from an interaction in the TPC. This leads to a better resolution in this vertex compared with the radial position (r), which is determined from the hit map of the S2 signal on the top PMT array. In this analysis, events with $\sigma_r > 3.0$ cm or $\sigma_z > 0.2$ cm are removed as multiple scatters.

- A fiducial volume cut (FV), which removes events occurring outside of the central region of the liquid xenon volume. An event is rejected if the radial energy-weighted position $r = \sqrt{(x^2 + y^2)}$, where x and y are given by Eq. (2.13), is > 68.8 cm as measured from the center of the TPC or if the energy-weighted position in z , also given by Eq. (2.13), is < 1.5 cm or > 132.1 cm. z is measured from the cathode wire, which defines the bottom of the forward-field region of the TPC. This definition of the fiducial volume is chosen to maximise the ratio of signal to background events, and yields a total fiducial mass of 5.6 tons.
- A vetoes cut, which uses coincident signals in the liquid scintillator or liquid xenon skin to reject events in the TPC. If there is an energy deposition > 200 keV_{ee} in the liquid scintillator or an energy deposition > 100 keV_{ee} in the liquid xenon skin occurring within 500 μ s of an energy deposition in the TPC, the event can be rejected as not contributing to the background rate. These thresholds are chosen to reduce ‘dead-time’ - the period in which the LZ TPC is not sensitive to WIMP interactions because a coincident signal has been registered, above threshold, in the vetoes. Contributions to the dead time from radioactive decays, such as ^{14}C and ^{152}Gd in the scintillator, can be eliminated while maintaining a high efficiency for vetoing events that scatter once in the TPC.

2.2.9 Muon-induced background rate

In total, 2.3×10^8 muons corresponding to ≈ 120 live years have been simulated in LUXSim and analysed using the software described in Section 2.2.8. The energy spectrum of ‘electromagnetic’ events - those events that produce energy depositions due to electromagnetic interactions - that occur in the forward-field region of the liquid xenon TPC are shown in Figure 2.31. At high energies (up to 1 GeV), the energy deposition due to muon ionisation loss is visible as a broad peak in the spectrum at ~ 700 MeV. The energy spectrum up to a few MeV shows the electron-positron annihilation line at 511 keV, as well as an ‘edge’ at ~ 200 keV, below which the spectrum falls off sharply. This peak is caused by large angle ($\theta \sim 180$) Compton

scatters in materials surrounding the detector. For this case, the scattered photon will have an energy:

$$E' = \frac{E}{1 + \frac{2 \cdot E}{m_0 c^2}} \quad (2.15)$$

where E is the initial energy of the photon and $m_0 c^2 = 0.511$ MeV is the rest mass of the electron. For gammas with energies of several MeV, where Compton scattering is the dominant energy loss process, implies scattered energies of roughly the same energy at ~ 200 -250 keV.

Figure 2.32 is the combined energy spectra of events in the forward-field and reverse-field regions of the LZ detector at low energies (< 100 keV). The top plot shows energy depositions of all nuclear recoils, neglecting electromagnetic energy depositions. This spectrum shows both ‘pure’ and ‘mixed’ events - the later referring to those events that also occur with electromagnetic energy depositions due to pile-up. Between 6-30 keV_{nr}, there are 1.4 ± 0.2 ‘pure’ NR events in 1000 days before any event selections are made.

In the bottom plot of Figure 2.32, the spectra of events surviving each of the cuts described in Section 2.2.8 are shown. Table 2.6 shows the number of surviving events after each analysis cut is applied to the data. The initial selection of events between the energies of 0.1 - 100 keV_{ee} is chosen to compare with the energy spectra shown in Figure 2.32b. The threshold of 0.1 keV has been applied to remove physically erroneous events, caused by a bug in Geant4 that allowed very soft X-rays with sub-eV energies to propagate through the geometry without interacting and deposit energy in the liquid xenon. From Table 2.6 and Figure 2.32b, it is clear that most events at these low energies are single scatters that are occurring outside of the fiducial volume in the sacrificial layer of liquid xenon at the outermost edges of the TPC. Of the handful of events remain, all are removed by the LZ veto systems (the skin and outer detector). In this analysis the water tank, which has high probability to veto events by detecting Cherenkov light, has not been considered. In any case, there are no events surviving all cuts, which allows a limit to be set on the number of background events coming from muon-induced sources. Using a Feldman-Cousins approach [102], the upper limit for the total exposure is 2.44 muon events at 90% confidence level. The rate in 1000 days, which is the expected nominal exposure time for LZ, is simply $2.44 \times \frac{1000}{\tau}$, where $\tau = 4.36 \times 10^4$ days is the live time of the simulated muons. So, the total muon-induced background is < 0.056 nuclear recoil events for the total expected LZ exposure. This rate is subdominant to the other sources of background, as will be discussed in more detail alongside other environmental backgrounds in Section 3.3.8 of this thesis.

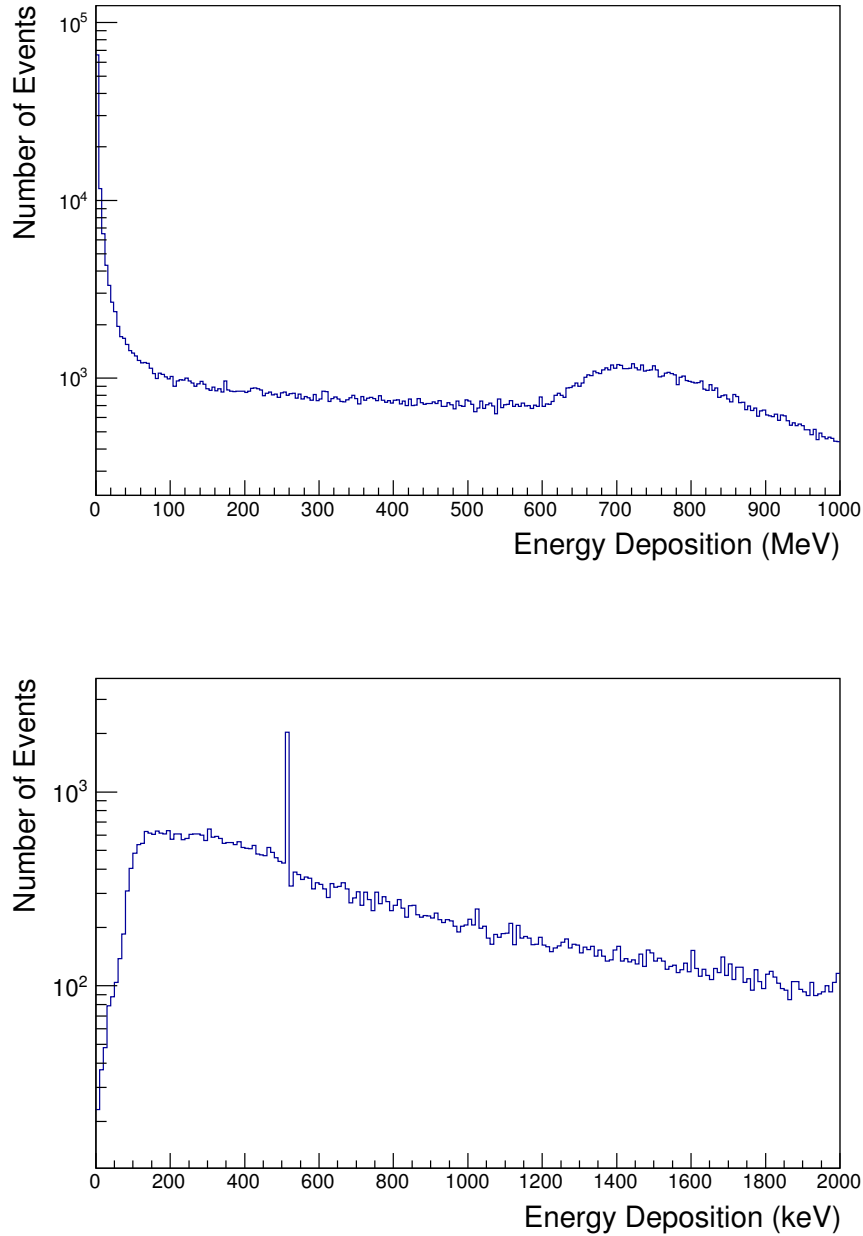


Figure 2.31: Energy spectra of all ‘electromagnetic’ events in the forward-field region of the liquid xenon TPC for high energies (above) and intermediate energies (below). The broad peak in the top plot is due to energy depositions from muon ionisation as they traverse length of the detector. In the bottom plot, the peak at 511 keV is caused by energy depositions of γ -rays produced from annihilation.

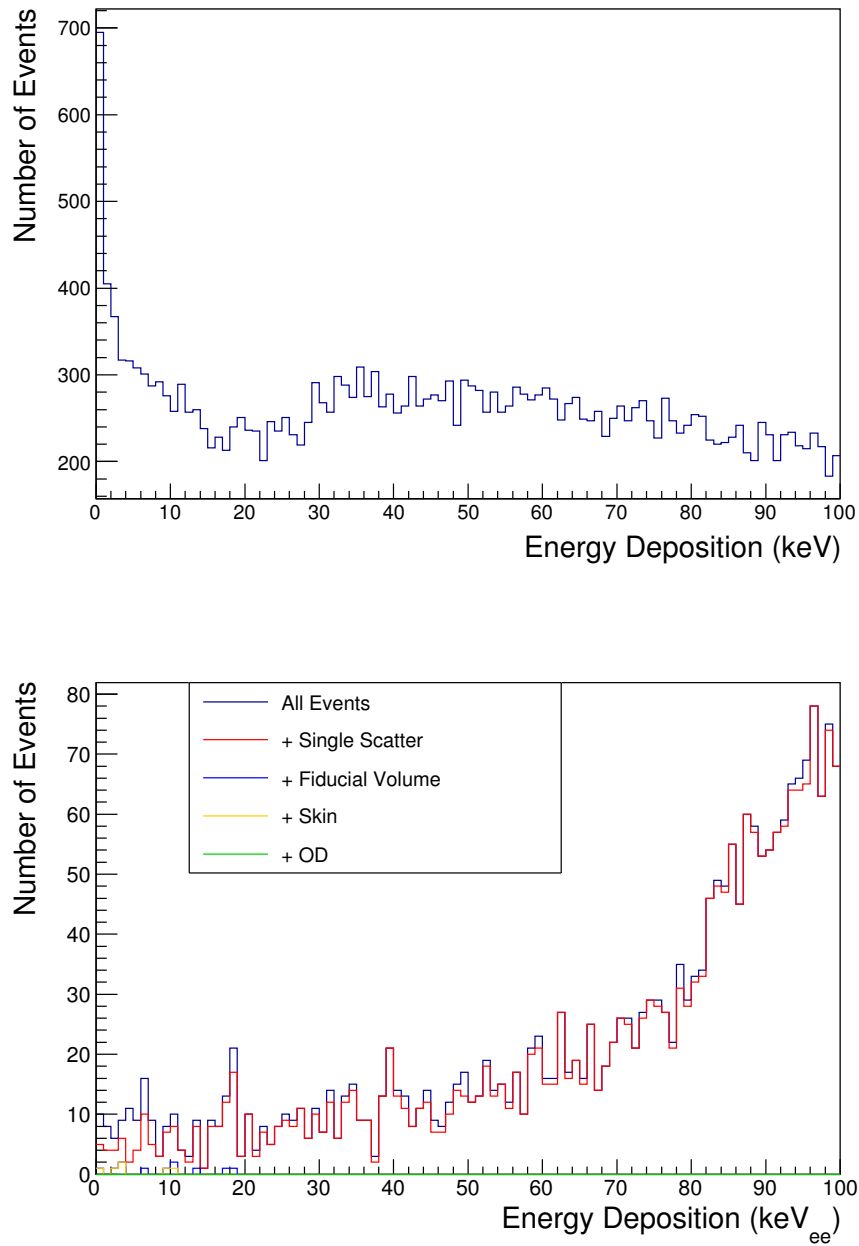


Figure 2.32: Energy spectra of muon-induced events in the forward-field and reverse-field regions of the liquid xenon TPC. The top plot shows energy depositions from nuclear recoils only, including both pure events (involving just nuclear recoils) and mixed events (involving nuclear recoils and electromagnetic energy depositions due to pile-up). The bottom plot shows events made up of energy depositions from both nuclear recoils and electron recoils. The spectra is shown for events surviving each of the analysis cuts described in Section 2.2.8

Table 2.6: Number of events surviving after each analysis cut for 2.3×10^8 muon events.

Cut	Number of surviving events
Region of interest (0.1 - 100 keV _{ee})	2235
+ single scatter	2128
+ fiducial volume	11
+ skin	6
+ outer detector	0

Chapter 3

Simulations of background radiations

3.1 Radioactive decay event generator

Many physics experiments, particularly those that rely on low-energy signals, require simulations of background radiations. The study of muon tomography as a monitoring technique for carbon storage sites, which was described in Section 2.1, assumes the elimination of background signals from local radioactivity. This is achievable, but successful implementation of the technology relies on detailed modelling of local radiations to understand how the detector should be arranged and what triggering conditions are required to identify muons with high efficiency. For underground experiments searching for rare events, the effects of radioactive contaminants in the detector and laboratory may be a limiting factor in their sensitivity. Accurate simulations are again required to understand the detector response to these sources. The input to these simulations comes from particle generators. A generator provides the products of a radioactive decay for a Monte Carlo program such as Geant4 [53] to transport the particles through a detector setup. In this section a radioactive decay event generator that has been developed for use in Geant4-based simulation packages will be described.

3.1.1 Simulations of radioactive backgrounds

Backgrounds from radioactive decay can come from a variety of radioisotopes, which may undergo a single decay or a chain of decays until a stable nucleus is reached. If events observed by a detector can be somehow attributed to these background sources, they may be rejected as not contributing to the signal rate. The goal of background

simulations is to quantify the rate of events from natural radiation that may obscure a potential signal. The background rate from a radioactive source depends on its activity, which is defined as the rate at which decays occur in a sample. If the background from a particular source with activity A_i is suppressed by a factor S_i , the rate of detected events B_{tot} from all sources combined is:

$$B_{tot} [\text{s}^{-1}] = \sum_i A_i \cdot S_i \quad (3.1)$$

The values of S_i for each source are determined by simulating radioactive decays, transporting particles through the detector materials and analysing the response of the detector to the background radiation. The survival probability S_i can be expressed as

$$S_i = \frac{N_{det}}{N_i} \quad (3.2)$$

where N_{det} is the number of detected events that are indistinguishable from signal-like events and N_i is the number of decays of the radioisotope from this source.

If A_i is large, there may be a pile-up of energy depositions from different parent nuclides occurring within the same event window. For most low-background experiments, the effects of detector pile-up are negligible and each individual radioisotope decay within a decay chain can be considered as an independent event. This is convenient for simulating radioactive sources since no prior knowledge of the activity is required and all normalisations can be applied after the simulation.

Conventionally, activities are expressed per unit mass of source material and the background rate can be quoted in units of events/kg/s. Eq. (3.1) can therefore be modified to take into account the mass of an individual source M_i and the mass of the detector target M_t :

$$B_{tot} [\text{kg}^{-1}\text{s}^{-1}] = \frac{1}{M_t [\text{kg}]} \cdot \sum_i S_i \cdot A_i [\text{Bq/kg}] \cdot M_i [\text{kg}] \quad (3.3)$$

where M_t is the mass of the detector target. For a chain of decays, Eq. (3.3) is still valid if the entire chain is in secular equilibrium (see Section 1.5.3). In this situation, the activity A_i of all isotopes on the chain will be the same. In reality the equilibrium may be broken due to manufacturing or natural processes, and the activities of sub-chains within the decay chain may be different. In this case, the decay chain can be still simulated in equilibrium, with an equal number of decays from each radioisotope, but the survival probability S_i^{sc} is determined for each sub-chain (or each isotope)



Figure 3.1: The event scheme for a ^{238}U decay chain using the default Geant4 setup. The event starts with the appearance of the parent isotope and terminates at the final stable daughter. The time of all tracks and steps are measured with respect to the appearance of the first isotope on the chain.

separately. The activity of each sub-chain, A_i^{sc} , then gives the normalisation factor to determine its contribution to the total background:

$$R_{det} [\text{kg}^{-1}\text{s}^{-1}] = \frac{1}{M_t [\text{kg}]} \cdot \sum_i \sum_{sc} S_i^{sc} \cdot A_i^{sc} [\text{Bq}] \quad (3.4)$$

3.1.2 Radioactive decay in Geant4

The Geant4 toolkit provides C++ classes to simulate the decay of radioactive nuclei. The model is described by data libraries taken from the Evaluated Nuclear Structure Data File (ENSDF) which provides information on nuclear half-lives, nuclear level structure for the parent or daughter nuclide, decay branching ratios and the energy of the decay process. The excited nuclear states that may be produced from an α - or β -decay may relax to the ground state, emitting γ -rays. This is described in Geant4 by a photon evaporation database that contains experimentally measured excited level energies, spins, parities and relative transition probabilities. As discussed in Section 1.5.3, a competing process to photon emission is internal conversion, which results in an ionised atom after the emission of an electron from an atomic shell. To take this into account, the photon evaporation database also includes the relative probabilities of γ -ray emission and internal conversion as well as the internal conversion coefficients for each atomic shell. X-rays and Auger electrons are subsequently produced via atomic relaxation according to the Livermore Evaluation Atomic Data Library (EADL).

To initiate a radioactive decay within Geant4, a user places a radioactive ion in the geometry, whereby it will undergo a single decay or multiple decays until it reaches a stable daughter radioisotope. In Geant4 this constitutes one event. Each event comprises particles tracks, and each track comprises steps where interactions, energy losses and energy depositions can occur and new particles can be spawned. The time of each step is measured with respect to the starting radioisotope on the decay chain. A representation of the Geant4 decay scheme for ^{238}U is shown in Figure 3.1.



Figure 3.2: The event scheme for a ^{238}U decay chain using the G4Decay generator. The decay chain is split into sub-events which correspond to the individual decays of the radioactive isotopes in the chain. The time of the tracks and steps are measured with respect to the appearance of daughter particles produced by the radioactive decay at the start of each sub-event.

3.1.3 Radioactive decay generator - ‘G4Decay’

While the definition of an ‘event’ varies between experiments, in general it is defined as a collection of particle interactions occurring within a given time window. If the time separation between two decays in a decay chain is larger than this time window, each sub-decay and the resulting interactions in the detector should be considered separate ‘events’. Furthermore, following the discussion in Section 3.1.1, the simulation should isolate each sub-decay from all other sub-decays coming from other decay chains that are present in the radioactive source. The scheme that is employed for the generator is shown in Figure 3.2, whereby the whole decay chain is split into individual events.

Splitting events

A user is able to input the atomic mass and atomic number of any radioactive isotope at run-time, and the generator automatically populates a list of radioactive isotopes in the decay chain. This has been achieved by writing a set of functions in the generator file that query the ENSDF data file and identify all radioactive isotopes on a decay chain. The list is then used to split events as Geant4 processes the chain of decays according to the algorithm shown in Figure 3.3.

To ensure multiple decay chains can be accommodated within the same Geant4 run, the list is updated at the start of a Geant4 event to represent the isotopes on the decay chain that will be simulated in that event. The list contains ID numbers of each isotope according to the Monte Carlo particle numbering scheme [6]. Under this numbering scheme, all energy levels of excited nuclear states are assigned the same ID. This can be problematic when trying to identify radioactive isotopes that decay directly from an excited state. In the ^{238}U decay chain for example, ^{234}Th undergoes β -decay to the excited states of ^{234}Pa . This decay is shown in Figure 3.4. 78% of these decays go directly to the 73.92 keV energy level, from which there is a β -decay

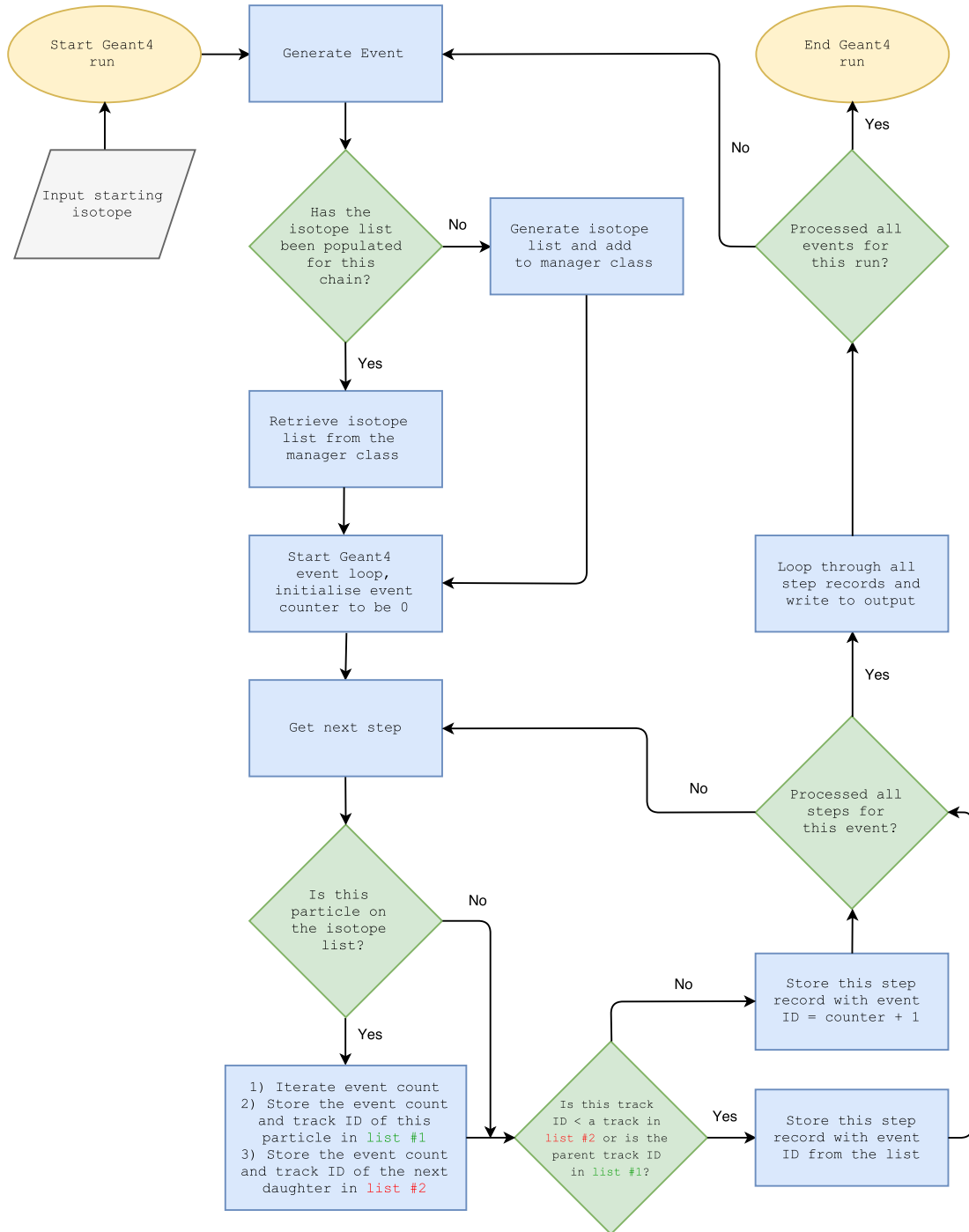


Figure 3.3: Flowchart showing the algorithm used in the G4Decay generator to split a decay chain into sub-events.

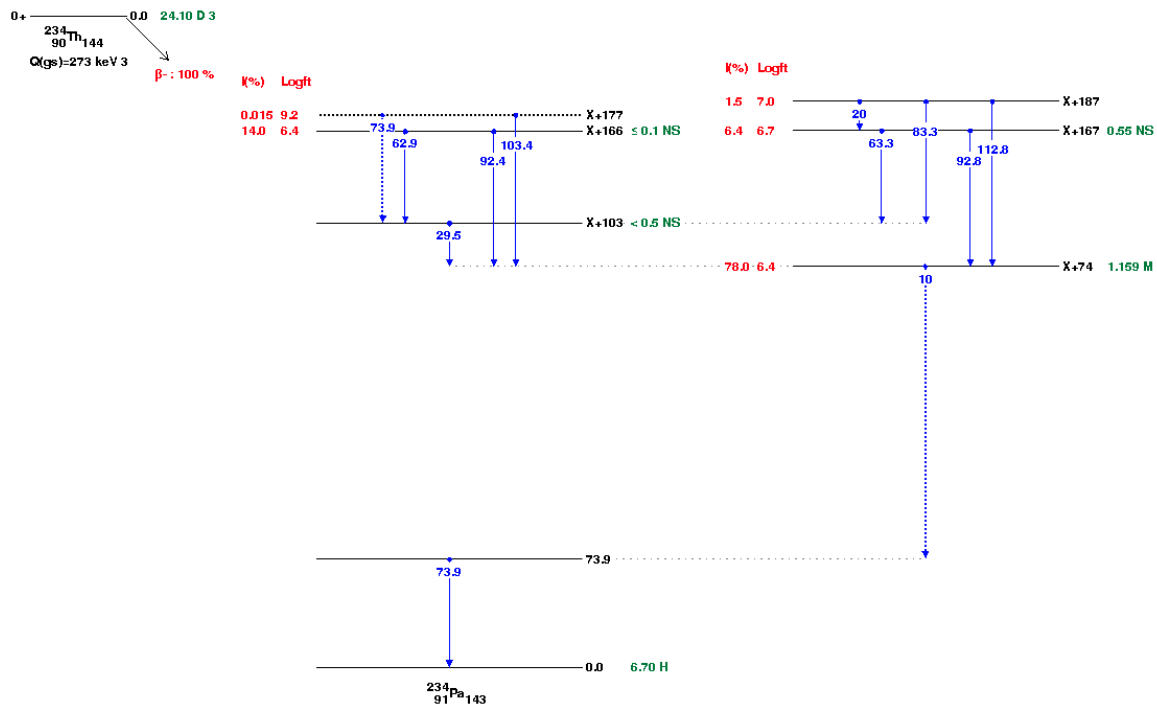


Figure 3.4: The β -decay of $^{234}\text{Th} \rightarrow ^{234\text{m}}\text{Pa}$. The energy levels of $^{234\text{m}}\text{Pa}$ are shown in black, as well as the energy (in blue) and intensity (in red) of each γ -ray from nuclear de-excitation. All excited states decay to the 73.92 keV energy level, from which there is a β -decay of $^{234\text{m}}\text{Pa}$ with a half-life of 1.16 minutes.

with a half-life of 1.16 minutes. 22% of the decays go to higher energy levels, all of which relax to the 73.92 keV level of $^{234\text{m}}\text{Pa}$, emitting γ -rays, conversion electrons, X-rays or Auger electrons. To ensure that all coincidences between particles within the same time window are grouped together, these particles should be in the same event as the β -particle from the decay of ^{234}Th . Subsequently, the 73.92 keV level must be uniquely identified and the event that starts with the β -decay of ^{234}Th should only terminate at the β -decay of $^{234\text{m}}\text{Pa}$. To uniquely identify a specific energy level, the list of radioactive isotopes also contains the particle lifetime. In this way, all events are guaranteed to start and end with a radioactive decay.

Timing resolution

An important consideration for this generator is the precision to which the time of the particle interactions is recorded. In the default Geant4 setup, time begins at the appearance of the parent radioisotope in the decay chain, and continues until the end of the Geant4 event which terminates once the final stable daughter product is reached.

The half-life of a long-lived isotope can be billions of years, for example ^{238}U has a half-life of 4.47 billion years and ^{232}Th has a half-life of 14.0 billion years. On these very large time scales, the limitations of standard data types start to become significant. A double floating point type has a precision of 16 decimal digits, and therefore after 1 billion years the timing resolution is 10 s. This would create an artificial pile-up of events for experiments where the physical detector systems are capable of resolving much smaller temporal separations. By resetting time to 0 for all of the daughter products of a radioactive decay, the time correlations within each individual sub-decay are maintained and the required timing resolution is achieved.

There are some physical phenomenon that may cause a real, physical pile-up of events. The shortest-lived daughter in the ^{238}U chain, for example, is ^{214}Po which has a half-life of 164.3 μs . For detector systems with a larger time window for an event, interactions from both ^{214}Po and its parent isotope ^{214}Bi will be detected within the same time window and therefore the same event. To account for this, isotopes with a half-life less than the response time of the detector system involved in the simulation are not added to the initial list of isotopes on the decay chain and are therefore automatically grouped into the same event as their parent isotope.

Validations

One of the requirements set out in Section 3.1.1 was for a chain of decays to be produced in equilibrium. The manner in which Geant4 simulates a decay chain ensures that for each user-defined event, 1 decay mode of each radioisotope within the chain will be simulated. Figure 3.5 shows the number of occurrences of an isotope in each decay tree for the ^{238}U and ^{232}Th decay chains using this generator. Since the ENSDF file contains information about the decay branching ratios, not all isotopes will appear in every decay tree. The relative probabilities of isotopes with parents that can decay by two modes in the ^{238}U and ^{232}Th are shown in Table 3.1.

Given that the chain is produced in equilibrium, it is possible to compare the energies and intensities of the gamma-lines generated in simulation against tabulated data. The National Nuclear Data Centre (NNDC) provides a database of decay data called NuDat [103], which contains intensities and energies for all γ -rays emitted in a decay via nuclear de-excitation. Figure 3.6 shows a spectrum of γ lines from nuclear de-excitation from all isotopes on the ^{238}U and ^{232}Th decay chains from both NuDat and a Monte Carlo simulation using the radioactive decay generator.

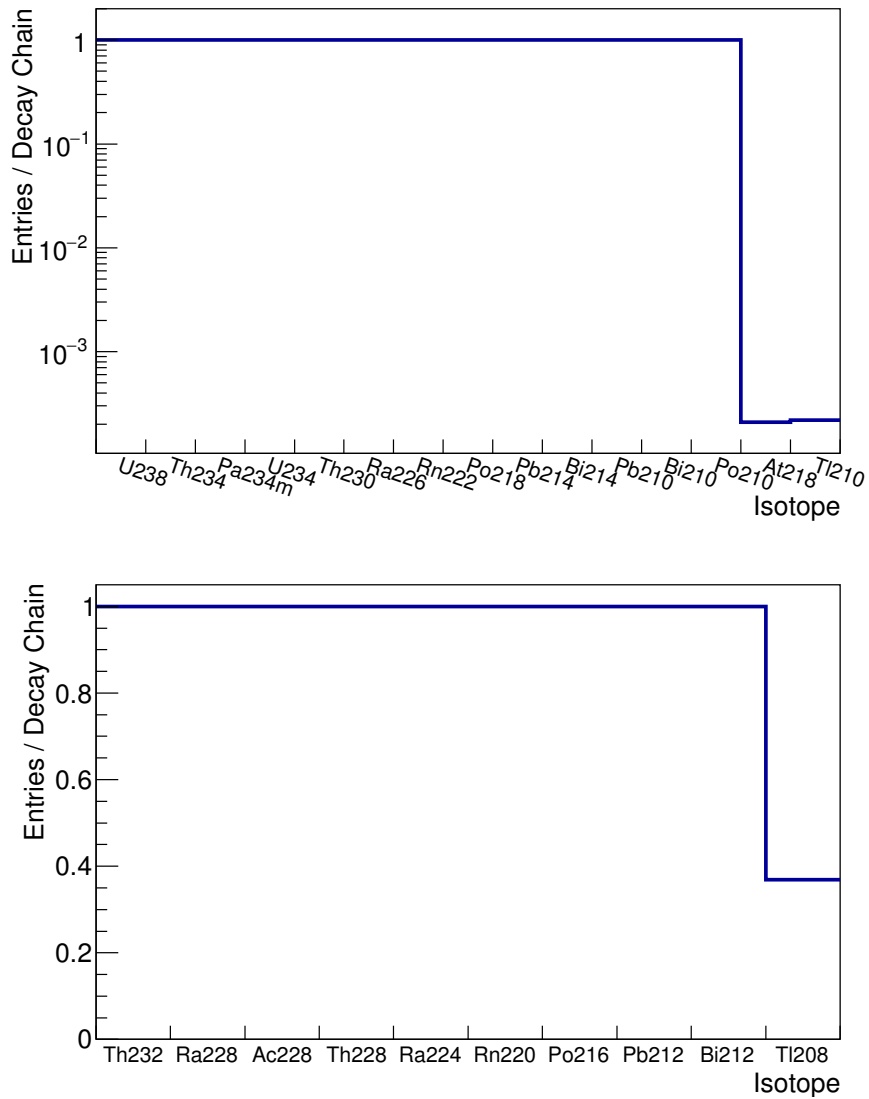


Figure 3.5: Number of occurrences of each radioisotope in each decay tree for the ^{238}U decay chain (top) and the ^{232}Th decay chain (bottom), based on $1 \cdot 10^5$ initial decays. In the top plot the occurrences of ^{214}Po are not shown because these events are automatically grouped with its parent isotope due to its short half-life. Similarly, in the bottom plot the occurrences of ^{212}Po are not shown.

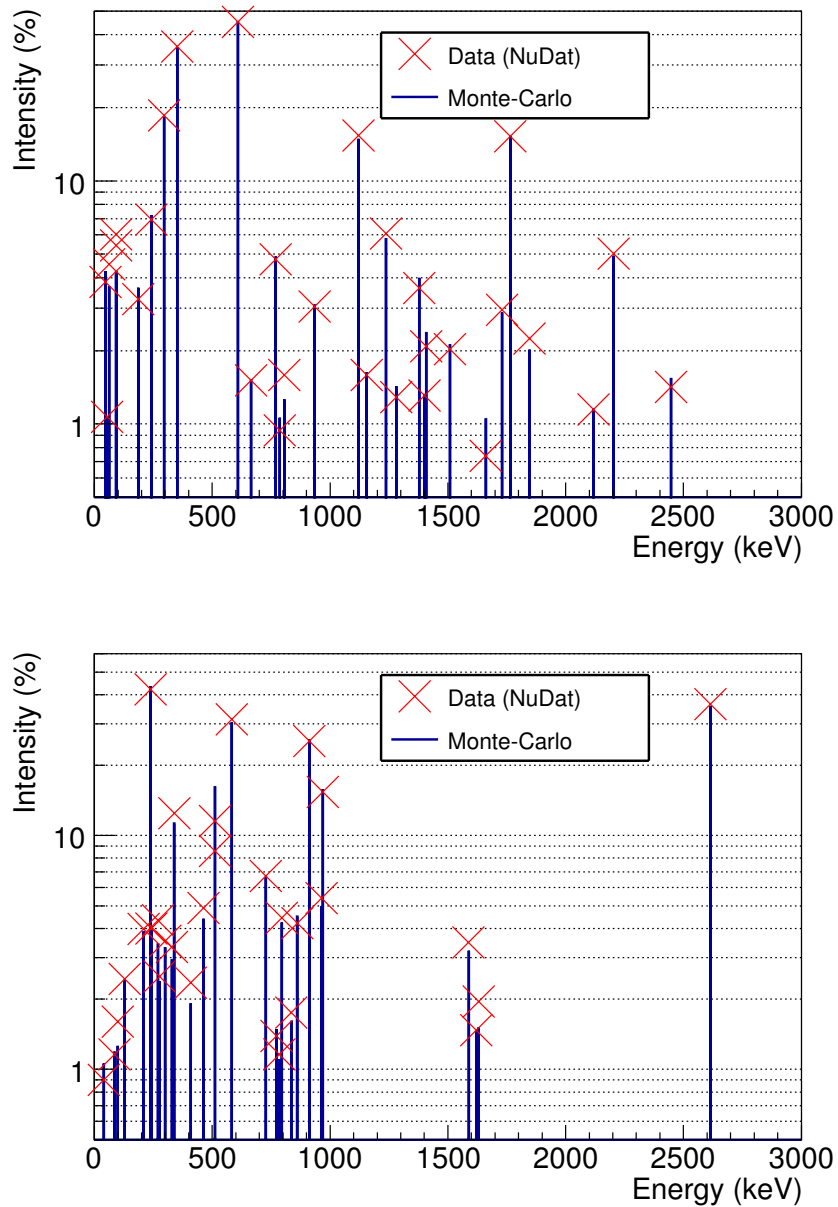


Figure 3.6: Comparison of γ -lines generated in a Monte Carlo simulation of 10000 decays using the G4DECAY generator (blue histogram) and data from the NuDat database (red markers) for the ^{238}U decay chain (top) and the ^{232}Th decay chain (bottom).

Table 3.1: Branching ratios of isotopes on the ^{238}U and ^{232}Th decay chains whose parent isotopes decay by two modes.

Decay chain	Isotope	Branching ratio
^{238}U	^{214}Pb	99.98 %
	^{218}At	0.02 %
	^{214}Po	99.98 %
	^{210}Tl	0.02 %
^{232}Th	^{212}Po	64.06 %
	^{208}Tl	35.94 %

3.2 Radioactive backgrounds for borehole detectors

The effectiveness of muon tomography as a technique to monitor carbon storage sites relies on the clear identification of muon signals above background noise. The dominant backgrounds will come from local radioactivity, in particular gammas rays from the ^{238}U and ^{232}Th , which have energies up to a few MeV. As was mentioned in Section 2.1.7, the radioactive background may be suppressed by requiring a number of coincident bar hits, N_{bar}^{hit} in order to identify a muon. There is also the possibility to distinguish muons by the total energy deposition in the bar. When traversing a scintillator bar, muons will deposit energy via ionisation energy loss, depositing $\sim 2 \text{ MeV g}^{-1} \text{ cm}^2$ of material. If the thickness of a typical scintillator bar inside a borehole detector is 2 cm, then the total energy deposition will be $\sim 4 \text{ MeV}$ for muons traversing the entire bar vertically, assuming the density of the scintillator material is 1 g cm^{-3} . This is higher than the end point energy of radioactivity, so in principle a trigger on signal size can be used to identify muons. In this section, simulations of local radioactivity from rock that surrounds a borehole detector will be presented. The goal of the study is to determine suitable values of N_{bar}^{hit} and an energy threshold E_{thres} that will remove all background signals.

3.2.1 Simulation setup

The Geant4 toolkit has been used to develop a simulation framework for this study. The detector geometry is made up of 20 plastic scintillator bars, each $2 \times 2 \times 100 \text{ cm}$ and arranged inside a cylindrical steel container. The container sits inside a cylindrical volume of rock, with inner radius $r_{in} = 11.2 \text{ cm}$, outer radius $r_{out} = 21.2 \text{ cm}$ and length $l = 100 \text{ cm}$. These volumes have been constructed inside of Geant4 and are shown in Figure 3.7. The setup is an example of a configuration that could be used for a

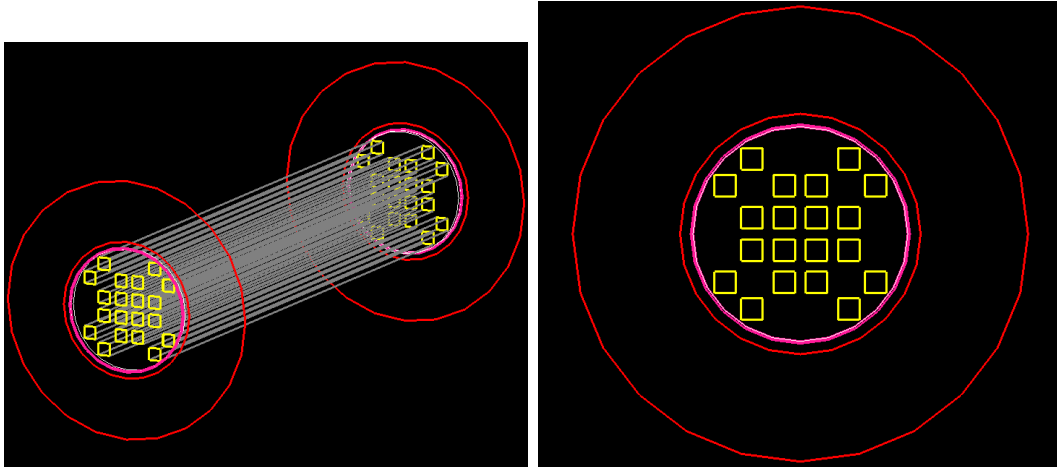


Figure 3.7: The detector setup as constructed in the Geant4 framework. For clarity, only the ends of the rock cylinder (red) and the steel casing (pink) have been drawn. In total, there are 20 scintillator bars (grey, with yellow ends) each with a thickness of 2 cm and a length of 100 cm.

borehole detector, and is similar to a smaller scale prototype detector that was tested inside a mock borehole at the STFC Boulby Underground Science Facility.

The rock material is defined as ‘standard rock’ with atomic number $Z = 11$, atomic mass $A = 22$ and density $\rho = 2.65 \text{ g}\cdot\text{cm}^{-3}$. The event generator described in Section 3.1 is used to simulate the radioactive decays of ^{238}U and ^{232}Th in the rock. For these simulations, the activity of ^{238}U and ^{232}Th are each assumed to be 10 Bq/kg based on measurements of typical oceanic rock concentrations for uranium (0.64 ppm = 7.9 Bq/kg) and thorium (2.8 ppm = 11 Bq/kg) [104]. Setting the activities of both isotopes to be equal is convenient for this study since it allows direct comparisons between the two isotopes. In reality, the activity of rock in the vicinity of a borehole detector may be significantly different than the values assumed here, but given the approach to the simulations it is easy to rescale the results from the assumed concentrations to some other activity. The initial decays are distributed uniformly throughout the volume and all particles that emerge from the rock surface are transported through the detector setup. All energy depositions in the scintillator bars are tracked and saved to a ROOT file for further analysis. The live time τ corresponding to N primary decays of an isotope i simulated using the generator is written as:

$$\tau[\text{s}] = \frac{N_i}{A_i[\text{Bq/kg}] \cdot V[\text{m}^3] \cdot \rho[\text{kg m}^{-3}]} \quad (3.5)$$

where A is the activity of isotope and V is the size of source volume. Since $\tau \propto 1/V$ for a given number of decays N , a reduction in V will also reduce CPU requirements. The inner radius of the rock $r_{in} = 11.2$ cm is fixed by the size of the borehole, so changes to V are considered by varying the values of outer radius r_{out} and length of the cylinder l . The distribution of R , the radial distance from the center of the borehole to the position of primary decays that produce an interaction in any of the scintillator bars is shown in Figure 3.8. This distribution is based on a preliminary simulation of 10^8 decays in a rock cylinder with $r_{in} = 11.2$ cm, $r_{out} = 41.2$ cm, and $l = 100$ cm. If the distribution shown in Figure 3.8 is denoted as $f(R)$, the fraction of events that will be lost if r_{out} is reduced to some value r_{new} in the simulation geometry is then given by:

$$L_f = 1 - \frac{\int_{r_{in}}^{r_{new}} f(R) dR}{\int_{r_{in}}^{r_{out}} f(R) dR} \quad (3.6)$$

The simulation code can process ≈ 240 decay chains in the rock per second including propagation of particles through the detector geometry. Assuming the activity A of ^{238}U and ^{232}Th is 10 Bq/kg, the total number CPU days t_{cpu} corresponding to a live time $\tau = 31$ days is then:

$$t_{cpu} = \frac{k \cdot (r_{new}^2 - r_{in}^2)}{240 \cdot N_s} \quad (3.7)$$

where $k = \tau [\text{s}] \cdot A [\text{Bq/kg}] \cdot \rho [\text{kg cm}^{-3}] \cdot \pi \cdot l [\text{cm}] = 2.23 \times 10^7 \text{ cm}^{-2}$ and $N_s = 86400$ is the number of seconds in a day. A reduction in the outer radius of the rock cylinder to $r_{new} = 21.2$ cm implies a run time $t_{cpu} \sim 348$ CPU days for each decay chain. This is almost 5 times less than the total run time for an outer radius of 41.2 cm. Using Eq. (3.6), $r_{new} = 21.2$ cm equates to $L_f = 0.248$ based on the preliminary simulation data shown in Figure 3.8. Given that the speed of the simulations can be increased drastically for a relatively small loss of events, an outer radius of 21.2 cm is adopted for this study. A similar but smaller loss of events is caused by constructing the rock cylinder with a length $l = 100$ cm. Combined, the overall reduction in the rock volume results in a loss of $L_f = 0.292$. The primary positions of decays in the rock that contribute to the background rate in the detector are shown in Figure 3.9.

The simulations for this study have been processed using the HEP computing cluster at the University of Sheffield. The outputs from the simulations are a collection of ROOT files which are stored on a central data disk.

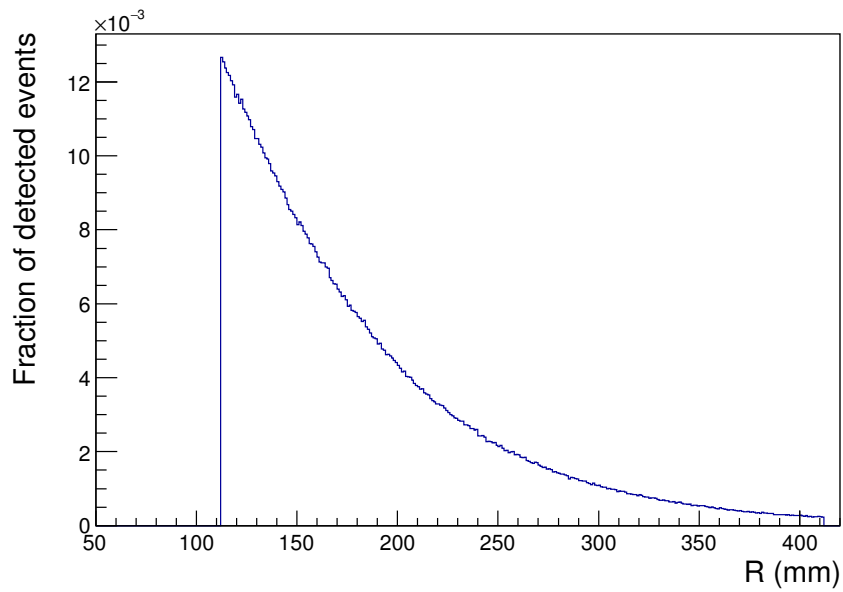


Figure 3.8: The fraction of detected events as a function of R , the distance from the center of the borehole detector.

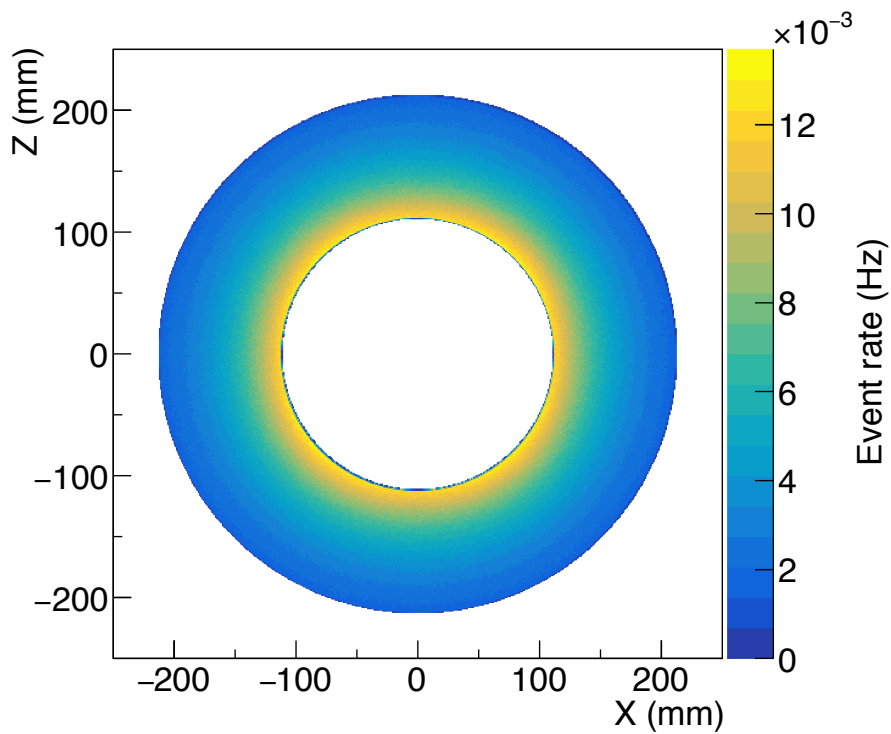


Figure 3.9: Initial positions of events in the rock that contribute to the background rate in the borehole detector i.e. events that give an energy deposition in any of the scintillator bars.

3.2.2 Background events in the detector

In total, approximately 1 live month of data has been simulated for both ^{238}U and ^{232}Th decay chains. Note that ^{238}U and ^{232}Th have been assigned the same activity, and therefore the same number of simulated decays produces the same live time for simulations according to Eq. (3.5). Instead of a full simulation of the detector response, the effects of energy resolution and position resolution are applied to the data during post-processing. Each deposition of energy - or ‘hit’ - by a particle inside of the scintillator bars is saved from Geant4 and stored in the output file. In reality, the energy depositions produce scintillation photons, which are then detected at the end of the bars using photosensors. To replicate this response, all of the hits in a bar that belong to same primary decay are grouped into a single ‘event’ with an energy, $E_{evt} = \sum E_{hit}$ and position $x_{evt} = \frac{\sum x_{hit} \cdot E_{hit}}{\sum E_{hit}}$ (where x represents the three coordinates x, y, z). To account for the energy resolution of the scintillator bars, the true energy of the event E_{evt} is smeared by selecting a random value from a gaussian distribution centered on E_{evt} with a spread σ_E given by:

$$\sigma_E = \xi \cdot \sqrt{E} \quad (3.8)$$

The value of ξ accounts for the intrinsic resolution of the detector and statistical fluctuations related to the counting of photoelectrons in the photosensors. The resolution of plastic scintillators has been investigated by other experiments [105] and for the study presented in this thesis a nominal value of $\xi = 0.032$ (for energy units in MeV) has been used. This is optimistic, since a the response of a scintillator bar geometry is likely to give lower resolutions, however the exact value of ξ isn’t expected to affect the final results drastically.

The true and smeared energy deposition per bar from ^{238}U and ^{232}Th decays are shown in Figures 3.10 and 3.11 respectively. The main features of the ^{238}U spectrum without energy smearing are the Compton edges at 0.43 MeV, 0.91 MeV, 1.54 MeV, 1.98 MeV and 2.20 MeV. The edges are produced by Compton scattering interactions at large ($\sim 180^\circ$) angles, where the incoming gamma ray will deposit the most energy. The Compton edge is given by:

$$E_{edge} = E \cdot \left(1 - \frac{1}{1 + \frac{2E}{m_e c^2}}\right) \quad (3.9)$$

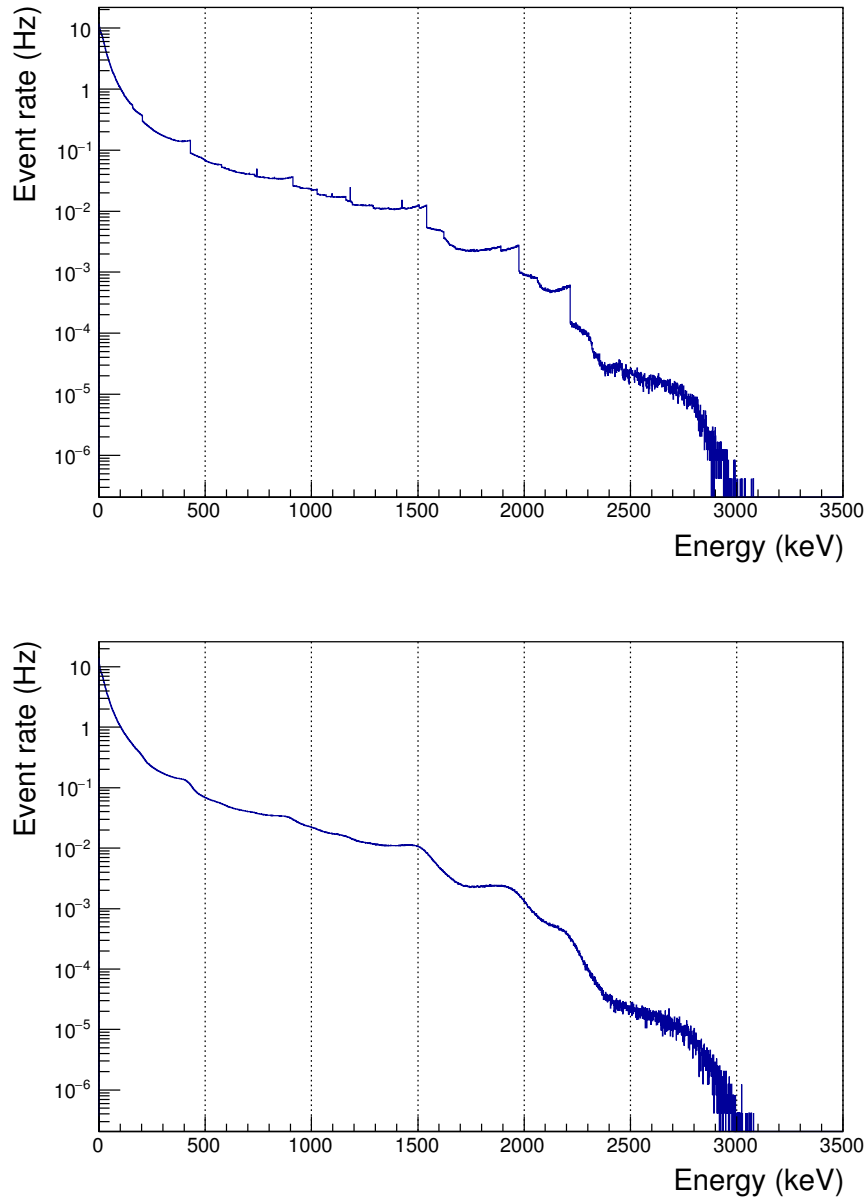


Figure 3.10: Energy deposition in the scintillator bars for all events coming from ^{238}U decays in the rock. The distribution in the top plot shows the true energy deposits and the distribution in the bottom plot shows the energy deposits after the smearing is applied according to Eq. (3.8) with $\xi = 0.032$.

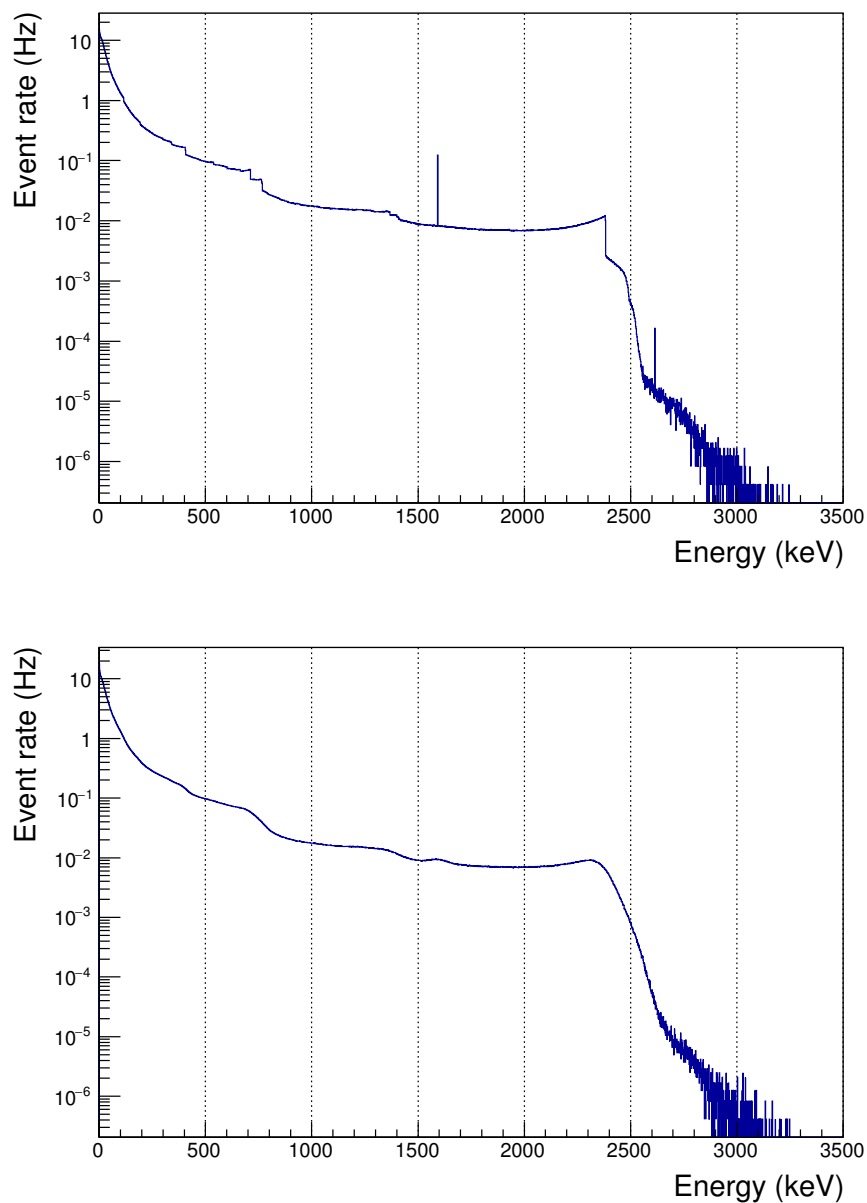


Figure 3.11: Energy deposition in the scintillator bars for all events coming from ^{232}Th decays in the rock. The distribution in the top plot shows the true energy deposits and the distribution in the bottom plot shows the energy deposits after the smearing is applied according to Eq. (3.8) with $\xi = 0.032$. For an explanation of the features visible in the top figure, the reader is referred to the main text.

where E is the energy of the incoming particle and $m_e c^2 = 0.511$ MeV is the rest mass of the electron. By rearranging Eq. (3.9) the incident particle energy corresponding to an edge energy E_{edge} is expressed as:

$$E = \frac{E_{edge} + \sqrt{E_{edge}^2 + 2 \cdot E_{edge} \cdot m_e c^2}}{2} \quad (3.10)$$

Using Eq. (3.9) the Compton edges correspond to incident photon energies of 0.61 MeV, 1.12 MeV, 1.76 MeV, 2.20 MeV and 2.43 MeV. These correspond to the prominent lines from the ^{238}U decay chain (see Figure 3.6 for reference). The ‘unsmearred’ ^{232}Th spectrum contains Compton edges at 0.40 MeV, 0.71 MeV, 0.76 MeV and 2.38 MeV, which correspond to initial photon energies of 0.58 MeV, 0.91 MeV, 0.97 MeV and 2.61 MeV. As expected, these are all prominent decay lines in the ^{232}Th . There are also two prominent peaks in the distribution at energies of 1.59 MeV and 2.61 MeV. Both peaks arise from an incident photon with energy $E_{inc} = 2.61$ MeV coming from ^{208}Tl . At this energy, pair-production contributes to the photon cross-section, and an electron-positron pair can be created within the scintillator bar. The electron is then captured by the scintillator and the positron annihilates with another electron, producing two photons each with a combined energy $E_\gamma = 2 \cdot m_e = 1.02$ MeV. If these photons escape the bar and deposit their energy elsewhere, the total energy deposited in the bar will be $E_{inc} - E_\gamma = 1.59$ MeV. If the photon does not escape, and deposits its energy in the same bar the total energy deposited in the entire event will simply be $E_{inc} = 2.61$ MeV. As expected, after the energy smearing is applied, these features are no longer identifiable. These energy distributions serve to validate the code framework that has been developed for this study, specifically the physics of the radioactive decay generator and the implementation of the particle transport included in the Geant4 toolkit.

Figure 3.12 shows the energy-weighted positions of events in the x - y plane (perpendicular to the length of the bars). Despite the fact that the outer bars subtend a larger solid from the rock surface, there are more events concentrated towards the central bars. After further study in which events were randomly distributed in the rock and then ‘traced’ through the geometry, it is found that events that traverse multiple bars produce more hits in the inner bars. This is not surprising given the circular nature of the rock, in order for an event to transverse more than one bar it should be heading roughly towards the center of the borehole. Furthermore, particles that scatter from one bar to another bar are more likely to do so from an outer bar to an inner bar, than from an inner bar to an outer bar. It can be argued that, since most events do produce

energy depositions in more than 1 bar, the excess of events in the central bars is a real effect.

3.2.3 Evaluating trigger conditions

The goal of this study is to understand the required trigger setup for the borehole detectors to eliminate local radioactive backgrounds while still detecting muons efficiently. The distribution of the number of bars hit for each event, N_{bar}^{hit} , is shown in Figure 3.13 for ^{238}U and ^{232}Th decays separately and then in Figure 3.14 for both isotopes combined, for various assumptions of the energy threshold of the bars. The rate of muons arriving at a single borehole detector for the depth considered in the simulations presented in Section 2.1 is approximately 0.5 mHz, which is also plotted in Figure 3.14 for comparison. Overall, the rate is higher for ^{232}Th due to the presence of higher energy γ -lines in the decay chain.

The results from the muon transport studies presented in Section 2.1 assume a negligible background, and therefore suitable values for N_{bar}^{hit} and the energy threshold E_{thres} need to be chosen in order to remove all backgrounds. It is clear that at least some energy threshold is required given the large number of bar hits per event for $E_{thres} = 0$. Indeed, it is surprising that up to 15 bars can be hit in a single event. Further investigation shows that these pathologies are indeed real and arise from radioactive decays in the rock with multiple photon emission lines. The background rate for $E_{thres} = 100$ keV, $N_{bar}^{hit} \geq 6$ and $E_{thres} = 200$ keV, $N_{bar}^{hit} \geq 7$ is still a significant fraction (over half) of the muon rate. A tighter restriction on N_{bar}^{hit} at these thresholds would significantly reduce the efficiency of muon detection. This can be seen in Figure 2.18 on page 63, where the acceptance A of muons is shown to be $< 1\%$ for such a requirement on N_{bar}^{hit} . A threshold of $E_{thres} = 500$ keV imposes a limit of $N_{bar}^{hit} \geq 5$. As was argued in Section 2.1.1, a minimum of 5 bars is required in any case to be able to reconstruct muon angles within a 5° accuracy. In this scenario, the background is $\lesssim 0.2\%$ of the muon rate and still subdominant to the predicted change in muon count, and is therefore not expected to impact the sensitivity of the tomographic method significantly.

Another factor to consider is the fraction of muon events which will experience some random coincidence with a background event. This rate should be low to ensure genuine muon tracks are to be reconstructed with a high efficiency. From Figure 3.14, the total rate of background events is $R_{bkg} \sim 10^2$ Hz assuming $E_{thres} = 500$ keV and activities of 10 Bq/kg for both isotopes. Assuming a muon event will be detected

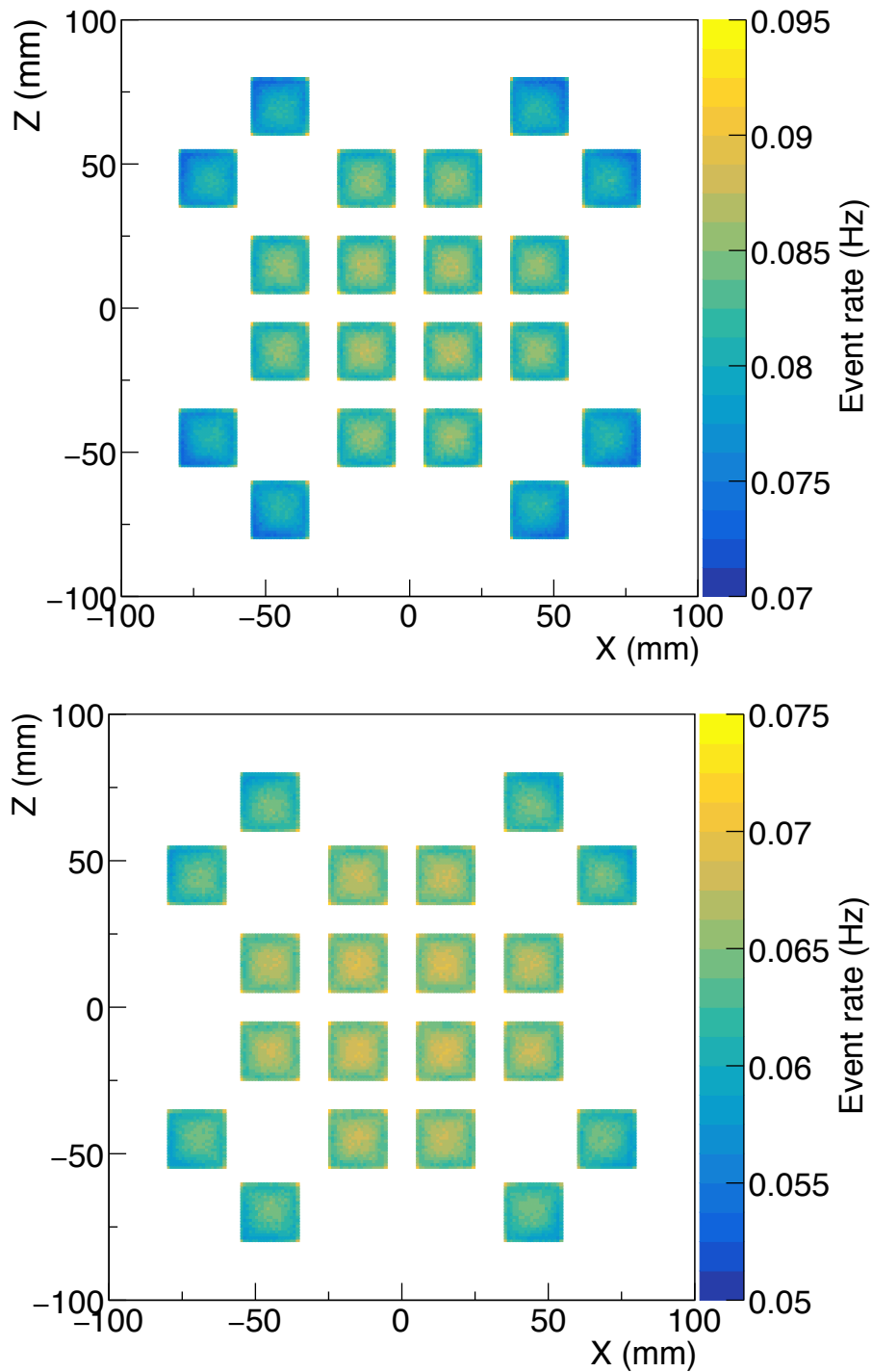


Figure 3.12: Energy-weighted positions of events in the scintillator bars from ^{232}Th decays (top) and ^{238}U decays (bottom). Note the different colour scales on the z axis. The overall rate is higher for ^{232}Th compared with ^{238}U .

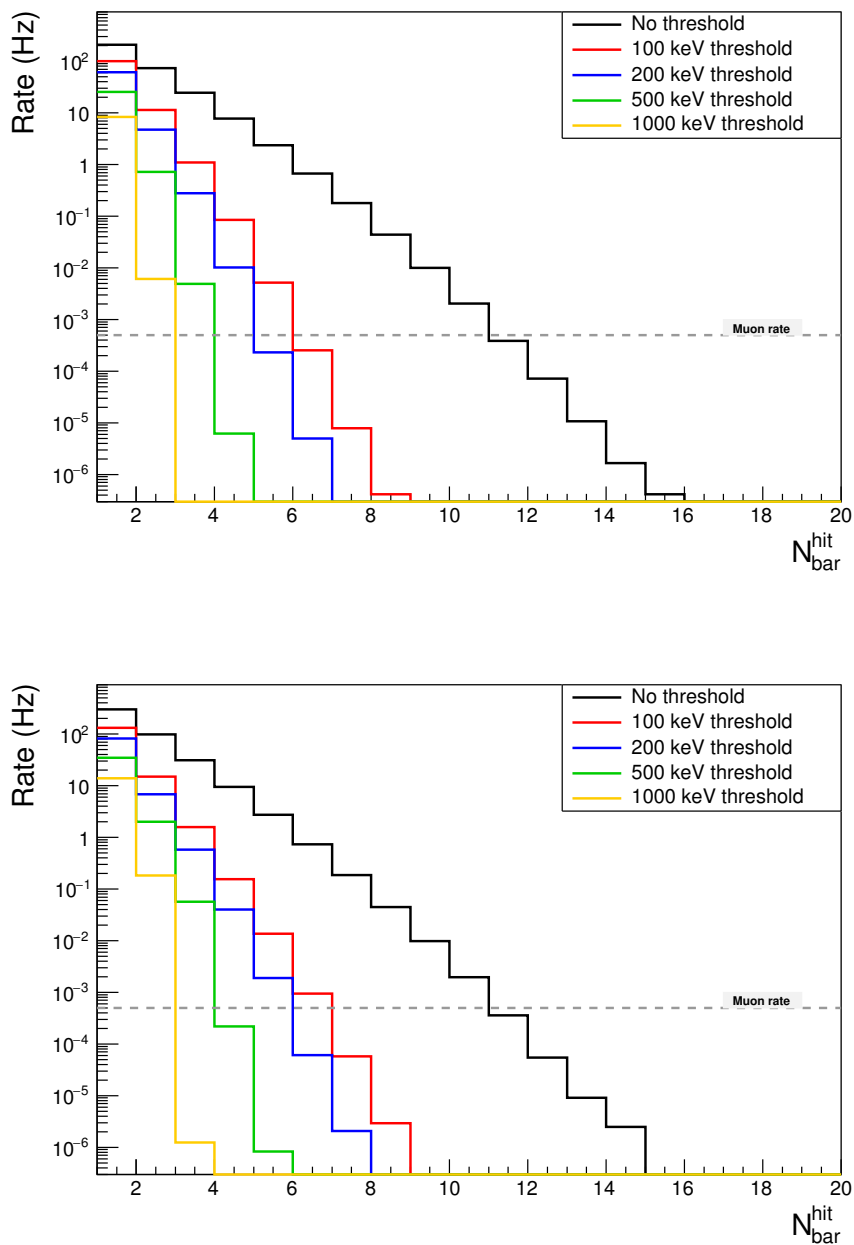


Figure 3.13: Rate of events as a function of the number of bars hit per event N_{bar}^{hit} for ^{238}U (top) and ^{232}Th (bottom). The distributions are shown for different energy thresholds E_{thres} ranging from 0 - 1000 keV. The rate of muons through the borehole detector, based on the simulations described in Section 2.1 is also shown.

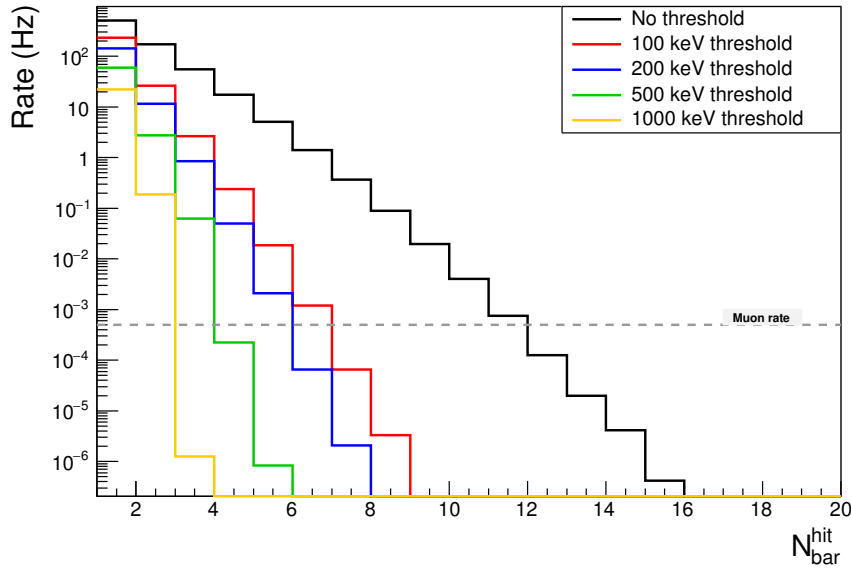


Figure 3.14: Rate of events as a function of the number of bars hit per event N_{bar}^{hit} for both ^{238}U and ^{232}Th events combined. The distribution is shown for different energy thresholds E_{thres} ranging from 0 - 1000 keV. The rate of muons through the borehole detector, based on the simulations described in Section 2.1 is also shown.

within a time window $\tau_w \sim 1 \mu\text{s}$, the probability of random coincidences is simply $\tau_w \times R_{bkg} = 10^{-4}$, which is an acceptable rate of signal loss.

3.3 Radioactive backgrounds for underground experiments

The most dangerous radiogenic backgrounds for underground experiments are derived from sources that are not shielded from a detector or have a very high activity. Many low-background experiments try to control radiogenic backgrounds by screening and cleaning materials that are used to construct the detector. As was discussed in Section 3.2 in the context of borehole muon detectors, rock naturally contains concentrations of radioactive elements. Even if a detector is surrounded by high-density materials, high energy γ -rays may penetrate the shielding and produce background signals. Neutrons are also a problem if they are not shielded by hydrogenous material. This section will describe Monte Carlo simulations of backgrounds for the LZ detector, both γ -rays and neutrons, coming from the rock of the Davis cavern at SURF.

3.3.1 Gammas from rock

Before embarking on a Monte Carlo simulation, it is instructive to estimate the background coming from the cavern walls. This will provide a useful cross-check of results obtained using detailed simulations and it also gives an estimate of the number of primary decays that should be simulated in order to produce some events in the detector. The calculation involves estimating the flux of γ -rays that are emitted from the rock surface, and then accounting for their suppression via shielding, the surface area of the detector and finally the expected suppression factor after event selections are applied. This procedure is quite generic, but the details depend on the setup of a specific experiment.

For LZ, the gamma flux coming from the cavern walls is attenuated significantly by the water tank, scintillator and the outer region of liquid xenon. Figure 3.15 shows the configuration of the LZ detector systems and the amount of shielding on all sides of the TPC. The smallest amount of shielding is on top where the thickness of water, scintillator tank (acrylic) and scintillator is ~ 175 cm. It is possible to write the background contribution of rock gammas as:

$$B [\text{s}^{-1}] = \phi_{wt} [\text{cm}^{-2} \text{s}^{-1}] \cdot A_{ocv} [\text{cm}^2] \cdot \alpha_{shield} \cdot R_{ocv} \quad (3.11)$$

where ϕ_{wt} is the flux of gammas at the water tank, A_{ocv} is the surface area of the outer cryostat vessel (OCV), α_{shield} is the attenuation of gammas due to the water, acrylic and scintillator shielding, and R_{ocv} is the rejection factor for gammas originating from the OCV to pass all analysis cuts and contribute to the LZ background rate. Recently, the gamma flux in the Davis cavern has been measured with a high-purity germanium (HPGe) detector and the integrated flux from 1.0 - 2.7 MeV calculated as $2.2 \text{ cm}^{-2} \text{ s}^{-1}$ [24]. Given the large amount of shielding on the sides of the detector and the presence of the steel pyramid beneath the water tank, most of the background from rock gammas is expected to be coming from the top of the cavern. As viewed from above, the OCV has an area of $A_{ocv} = 3.1 \times 10^4 \text{ cm}^2$. The highest energy gammas from the rock are 2614 keV from ^{208}Tl decay in the ^{232}Th chain. At this energy, the attenuation length in water is 23 cm [106], and therefore $\alpha_{shield} = e^{-175/23} = 5 \times 10^{-4}$ assuming the attenuation in scintillator and acrylic is similar to water given their comparable densities. Finally, $R_{ocv} = 2.5 \times 10^{-9}$ (for gammas emitted towards the detector) based on previous simulations [16]. Using Eq. (3.11), the estimated rate from rock gammas is $B [\text{s}^{-1}] \sim 8.6 \times 10^{-8}$ which is ~ 7 events in 1000 days in the energy range 1.5 - 6.5 keV_{ee}.

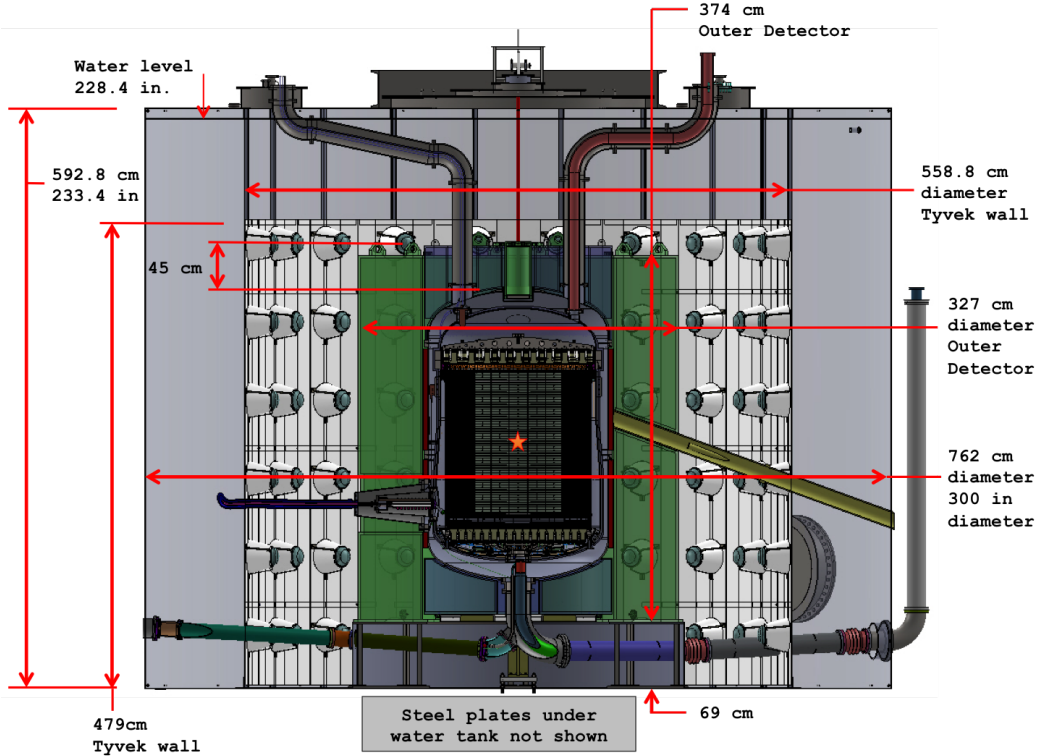


Figure 3.15: The arrangement and dimensions of the LZ detector systems [19].

3.3.2 CPU requirements

Although the rate calculated in Section 3.3.1 would be manageable for LZ, especially after applying ER/NR discrimination of $\sim 99.5\%$ [16], it motivates a full Monte Carlo study to reduce the large systematic uncertainties in the calculation. Additionally, this estimate provides an idea of the number of primary particles that is required to obtain some events that survive all analysis cuts. The number of gammas emerging from the rock surface for an isotope i is:

$$N_{\gamma,i} = N_{\gamma}^{chain} \cdot M [\text{kg}] \cdot A_i [\text{Bq/kg}] \quad (3.12)$$

where A_i [Bq/kg] is the activity of the isotope i in the rock, M [kg] is the mass of the rock volume from which the gammas are generated and N_{γ}^{chain} is the number of γ -rays emitted per decay chain. As was mentioned in Section 3.3.1 the flux of gammas in the Davis Cavern has been measured using a HPGe detector. The intensities of the highest energy lines from the ^{238}U and ^{232}Th decay chains and the ^{40}K single decay have been measured and are shown in Table 3.2. The errors quoted here are purely statistical, and the systematic uncertainties are much larger (approximately a factor

Table 3.2: Intensities of the highest energy gamma lines from the ^{238}U and ^{232}Th decay chains and the ^{40}K single decay as measured by a HPGe detector in the Davis cavern [24].

Isotope (chain)	γ -ray energy	Flux ($\text{cm}^{-2} \text{s}^{-1}$)
^{40}K	1460 keV	$3.6 \times 10^{-1} \pm 8.1 \times 10^{-4}$
^{214}Bi (^{238}U)	1764 keV	$5.9 \times 10^{-2} \pm 3.4 \times 10^{-4}$
^{208}Tl (^{232}Th)	2614 keV	$5.6 \times 10^{-2} \pm 3.4 \times 10^{-4}$

Table 3.3: Activity, concentration and number of gammas in 1000 days coming from the Davis cavern for each radioisotope. These values are calculated from the gamma spectrum shown in Figure 3.16, which is based on measurements made in [24].

Isotope	Activity (Bq/kg)	Concentration	Decays in 1000 days
^{40}K	716	2.31 % ($^{\text{nat}}\text{K}$)	7.18×10^{16}
^{238}U	73.4	5.95 ppm	7.36×10^{15}
^{232}Th	26.1	6.42 ppm	2.62×10^{15}

of 2) since the calibration data that was used to interpret these results is taken from a different detector, albeit one of the same type and size. The activities of the three isotopes (^{238}U , ^{232}Th and ^{40}K) can be determined by normalising the highest energy lines of the simulated spectrum, shown in Figure 3.16, to the measured flux values in Table 3.2. The gamma flux was generated using LUXSim [91], assuming the same cavern geometry that was described in Section 2.2.5. 10^9 ions of each radioisotope were uniformly distributed throughout a 30 cm ‘shell’ of rock on the inside of the cavern and allowed to decay according to the generator described in Section 3.1. All gammas emerging from the cavern walls were recorded. The calculated activities, and the corresponding concentrations, are tabulated in Table 3.16 along with the number of decays corresponding to 1000 days ¹.

From these estimates, it is clear that a very large number of initial decays are required to simulate the equivalent of 1000 days and produce some events in the liquid xenon after all cuts. This is computationally expensive - transporting gammas from the rock through the entire geometry takes approximately 5 ms per decay chain, which equates to an unfeasible amount of computing resources for $O(10^{15})$ initial events. A solution to this problem is to break the simulation into several stages. Gammas can be propagated through a section of the geometry at each stage, with those surviving being ‘boosted’ i.e. re-propagated again several times during the next stage of the simulation.

¹1000 days in the intended exposure time for LZ data taking.

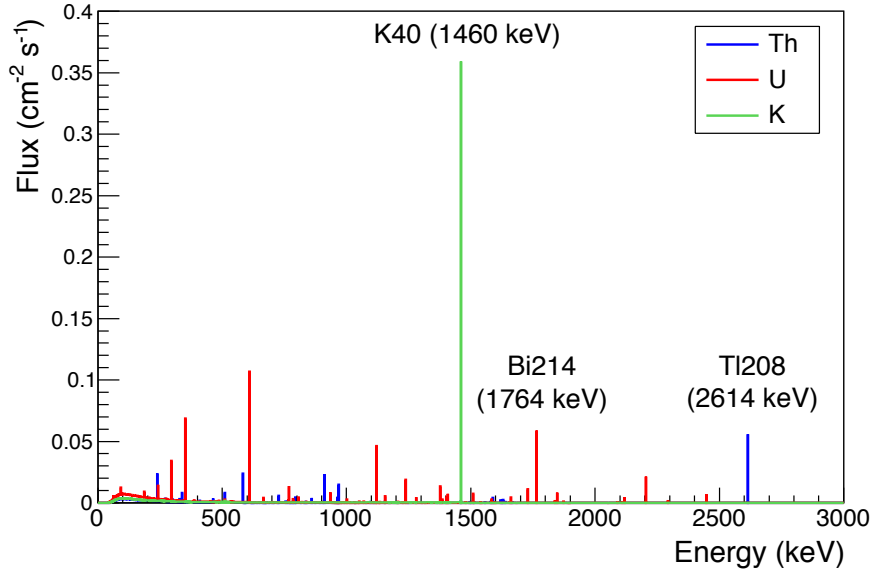


Figure 3.16: The simulated gamma flux emerging from the rock, normalised to the measured gamma lines from Table 3.2.

3.3.3 Event biasing scheme

The event biasing scheme requires significant changes to the LUXSim framework to allow particles to be saved (and terminated) as they pass through a user-defined surface, and for these events to be read in during the next stage of the simulation.

For any Geant4-based simulation, a particle ‘track’ is sub-divided into steps, and at each step the particle being tracked will undergo some type of interaction. A ‘step’ is also forced by Geant4 when a particle crosses a boundary between two volumes. In its regular operation, the LUXSim code requires a user to specify (at run-time) which particle tracks should be recorded by assigning record levels to volumes in the geometry. LUXSim collects all of the steps as they are processed by Geant4 into a number of ‘step records’. Each ‘step record’ belongs to an individual geometry volume, and at the end of each event the ‘step record’ is written to the output file for all volumes that have a record level specified by the user. With this in mind, the obvious way to implement the event biasing scheme is to construct physical surfaces inside of the existing geometry, which can then be assigned a record level in LUXSim such that gammas which pass through it are recorded and then immediately killed. This approach has proven unsuccessful due to the requirement, enforced by Geant4, that geometry volumes cannot overlap. Given the complicated structure of the LZ detector

setup, including conduits and ports, it is not possible to define a surface that does not overlap with any of the existing volumes.

An alternative approach is to construct an artificial volume. As each particle takes a step (due to an interaction or because it traverses a physical boundary) its position can be used to determine whether it is outside or inside of this artificial volume. Those tracks which pass inside of the artificial volume can then be recorded, written to the LUXSim output and subsequently terminated. This approach has been implemented in LUXSim in such a way that the artificial volume can be defined at run-time. This is preferable, since several different stages of the simulation can then use the same compiled code. Given that most of the detector volumes outside of the TPC (water tank, scintillator, cryostat vessels) are approximately cylindrical, the surfaces are also defined as cylinders to ensure gammas travel through a similar amount of shielding on all sides at each stage. The placement of the cylinders is important - if there is too much shielding between surfaces for a stage of the simulation, only a small proportion of gammas will survive and the result may be incorrectly biased. Furthermore, because physical volumes are not being constructed in the simulation geometry, the artificial surfaces should be defined just outside of a physical geometry boundary. This means that gammas that do not interact (which in fact are those that will contribute most to the background) will be saved as they cross the boundary between the physical volumes. Figure 3.17 shows the approximate positions of three surfaces that have been used in these simulations overlaid on the LZ geometry.

In addition to saving gammas, a new particle generator has been developed to read in the binary output from the previous stage of the simulation and regenerate the particles. The ‘boost factor’ i.e. the number of times a gamma should be re-propagated, is configured using a command specified at run-time.

Given the requirements set out in Section 3.3.2, $O(10^{15})$ decays in the cavern are required to produce background events that survive all analysis cuts. The gammas are ‘boosted’ by a factor of 100 at each of the three surfaces, which has the effect of increasing the effective number of primary decays in the rock by a factor of 10^6 . An initial batch of 100 simulation jobs, each containing 10^7 primary decays per job, has been processed through the four stages of the simulation using the Sheffield HEP computing cluster. During the final stage all interactions in the liquid xenon TPC, liquid xenon skin and scintillator are recorded for further processing.

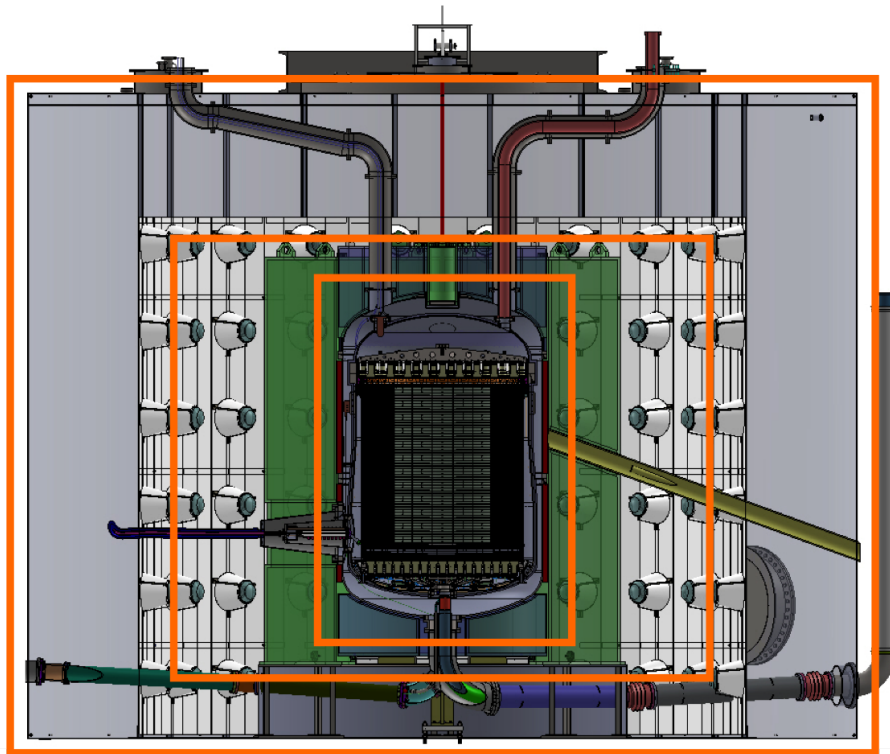


Figure 3.17: The arrangement of the LZ detector with the approximate positions of the three surfaces on which gammas are saved and boosted shown in orange [19].

3.3.4 Geometry construction

The dimensions of the cavern and the composition of the rock has been discussed in Section 2.2.5. The thickness of rock that contributes significantly to the gamma flux in the lab is approximately 30 cm, as calculated from previous simulations using a similar setup [107]. For these simulations, a 30 cm ‘shell’ of rock has been constructed in LUXSim to be the source volume for radioactive decays of each isotope. In addition, a cylindrical section of rock (radius = 3 m, height = 0.15 m) is added beneath the steel pyramid at the bottom of the water tank. Figure 3.18 shows a visualisation of these volumes.

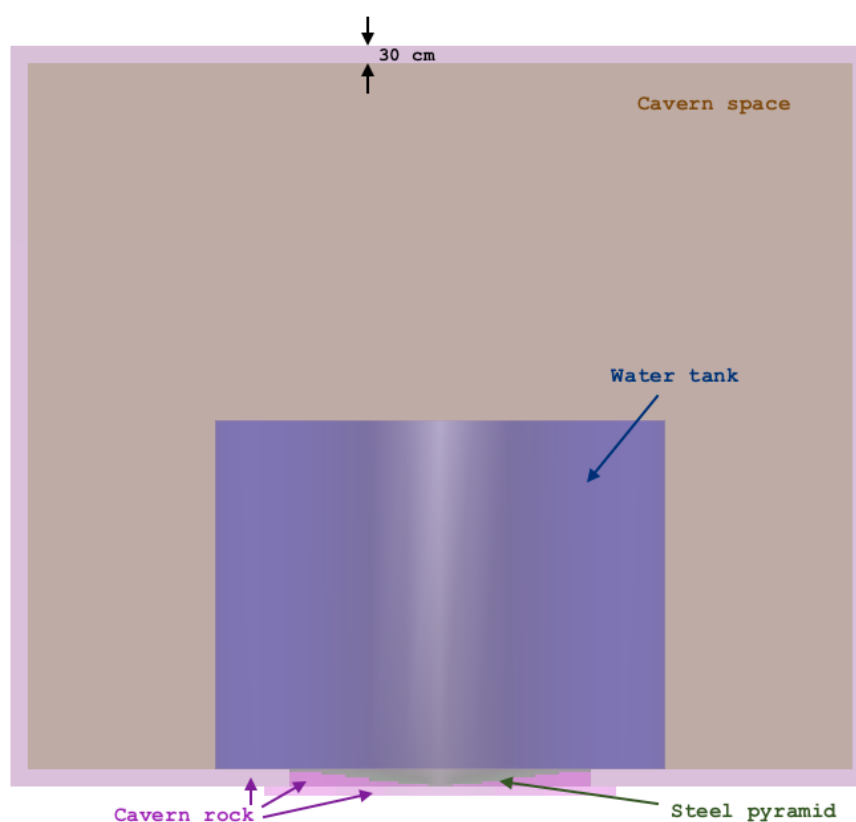


Figure 3.18: Visualisation of the simulation geometry showing the cavern rock ‘shell’ (magenta), the cavern space (brown), the water tank (blue) and the steel pyramid (green).

3.3.5 Analysis and results

The spectrum of gammas at each stage of the simulation is shown in Figure 3.19 for each isotope in the cavern rock. At stage 1, the gammas are arriving at the surface of

the water tank having only been attenuated slightly by interactions in the rock prior to entering the lab. The effect of the shielding from water and scintillator, as well as the solid angle from one surface to the next, can be seen in the reduction of the gamma flux at the two subsequent stages. At the end of stage 3, just before gammas enter the inner cryostat vessel, the 2.6 MeV line from ^{208}Tl is the largest contributor to the overall flux.

The analysis software for data obtained with the LUXSim/BACCARAT has previously been described in Section 2.2.8 of this thesis. For this study, in addition to the reduced quantities for each event such as total energy deposition, energy-weighted position, energy-weighted variance etc., the response of the LZ detector to interactions in the liquid xenon TPC has been calculated using the Noble Element Simulation Technique (NEST) [108] package. The NEST code consists of a collection of physics models to calculate the scintillation light and ionisation charge yields based on interaction type (NR or ER) and total energy deposition. A detector model, also included in NEST, then takes the number of quanta (scintillation photons and ionisation electrons) produced in an interaction and calculates the total size of the S1 and S2 observables. The detector model takes into account the light collection response of the detector, which is modelled using a dedicated simulation of scintillation photons distributed throughout the TPC, the electric field and the probability of a single photon to generate two photoelectrons on the PMT photocathode. The later effect was first discussed in the context of metallic surfaces [109, 110], but has since been studied and measured using PMTs [111]. The result is the number of detected photoelectrons (phd) for both S1 and S2 signals. NEST then applies the LZ trigger requirement of a three-fold coincidence of PMT hits for S1 signals. At this point, NEST also computes a ‘corrected’ S1 and S2 response, S1c and S2c. For S1 signals, the correction is based on the position dependent light collection efficiency. S2 signals are corrected for the expected electron lifetime ($\sim 800 \mu\text{s}$).

The spectrum of events in the the TPC at low energies coming from $10^{15} \text{ }^{232}\text{Th}$ decays in the rock is shown in Figure 3.20. As well as reducing the overall rate of events, applying the selection cuts produces a flat spectrum up to 150 keV_{ee} . The number of events in the region of interest can then be calculated as:

$$N_{roi} = \frac{W_{roi}}{E_{max} - E_{min}} \cdot \int_{E_{min}}^{E_{max}} f(E) \quad (3.13)$$

where W_{roi} is the size of the region of interest (in energy units) and E_{min} and E_{max} are the limits over which the energy spectrum $f(E)$ is flat. In the previous study of muon-induced backgrounds, the region of interest was defined as $1.5\text{-}6.5 \text{ keV}_{ee}$. Now

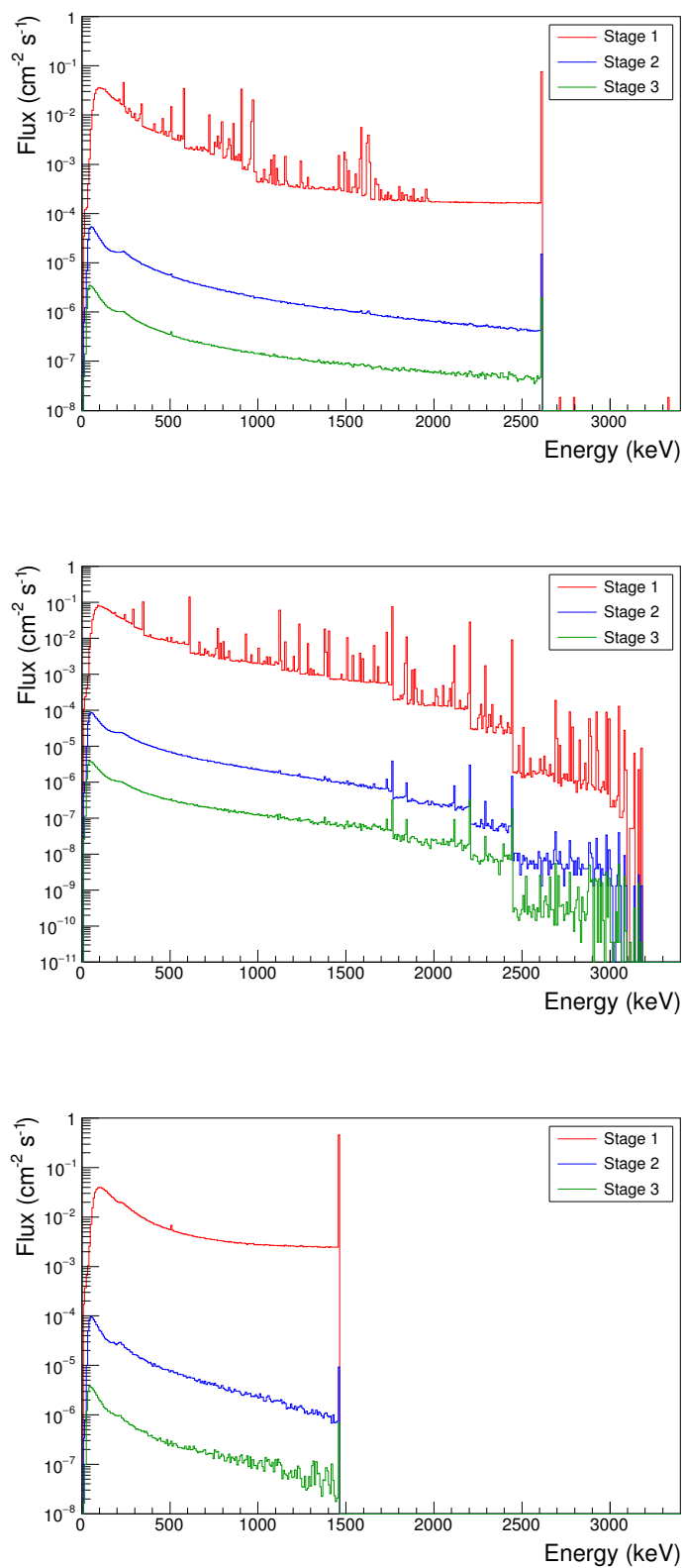


Figure 3.19: Energy spectra of gammas, coming from ^{232}Th (top), ^{238}U (middle) and ^{40}K (bottom) decays, at the end of each stage of the simulation run.

that the detector response in terms of S1/S2 signals is available, the region of interest is defined as $0 < S1c \text{ (phd)} < 20$ and $S2 \text{ (phd)} > 450$. The cut on $S1c > 0$ includes the three fold coincident requirement that has already been applied by NEST. The cut on S2 corresponds to ~ 5 single electrons per interaction site and ensures the S2 signal is large enough to reconstruct the position of an event. This region of interest corresponds to $1 < E_{dep} \text{ (keV}_{ee}) < 7.81$ ². So, from Eq. (3.13), the number of events between 0-150 keV_{ee} should be multiplied by a factor of $\frac{6.81}{149} = 0.0457$ to obtain the total background for each isotope. In the case of ²³²Th, $\int_{1\text{keV}_{ee}}^{150\text{keV}_{ee}} f(E) = 28$ and the simulated data (10^{15} decays) corresponds to 382 days, so the total background in 1000 days is simply $N_{bkg} = 28 \cdot 0.0457 \cdot \frac{1000}{382} = 3.35 \pm 0.63$. This result, along with those from ²³⁸U and ⁴⁰K is shown in Table 3.4. Note that for ⁴⁰K an additional ‘boost’ of a factor of 10 was applied at the final stage of simulations to ensure some events were surviving all analysis cuts.

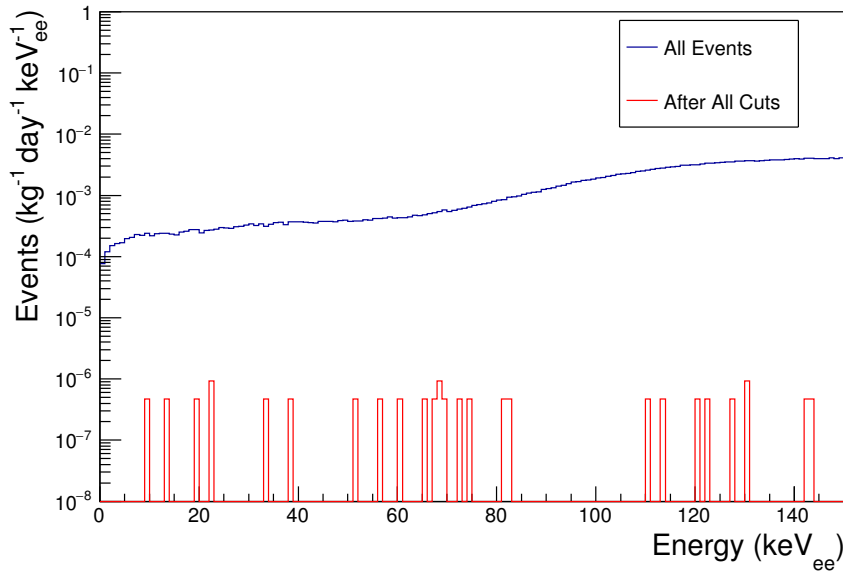


Figure 3.20: Energy spectrum of events in the forward-field region of the TPC after 10^{15} ²³²Th decays in the rock, before any cuts are applied (blue) and after all cuts are applied (red). Only events with $S1c \text{ (phd)} > 0$ and $S2 \text{ (phd)} > 450$ are included.

The final background rate from all isotopes combined is 5.7 ± 1.1 ER events in 1000 days. This agrees well with the very simple calculation presented in Section 3.3.1.

²Based on simulations of ²²²Rn dispersed throughout the liquid xenon volumes, then selecting $0 < S1c \text{ (phd)} < 20$ to get the equivalent energy range in units of keV_{ee}.

Table 3.4: Simulated live time and background rates coming from the decays of ^{40}K , ^{238}U and ^{232}Th in the cavern rock.

Isotope	Decays simulated	Live time (days)	Extended ROI	Background (1000 days)
^{40}K	10^{16}	139	3	0.99 ± 0.57
^{238}U	10^{15}	136	4	1.34 ± 0.77
^{232}Th	10^{15}	382	28	3.35 ± 0.63
Total				5.7 ± 1.1

This rate is sub-dominant to many other sources of ER background for LZ [16], as discussed in more detail in Section 3.3.8.

The distribution of events in the TPC is shown in Figure 3.21 for ^{232}Th decays. The 28 events surviving all cuts and depositing energy inside the fiducial volume are mostly clustered in the top right-hand corner. These events are caused by gammas that travel vertically downwards through the smallest section of shielding at the center of the water tank and undergo a large deflection, losing a significant fraction of their total energy. They subsequently travel towards the corner of the TPC (close to the wall) and deposit a small amount of energy ($< 150 \text{ keV}_{ee}$).

3.3.6 Neutrons from rock

Neutrons are expected to be shielded by the water tank, given that the flux of neutrons from radioactivity is attenuated by an order of magnitude in $\sim 10 \text{ cm}$ of water. There are, however, several pipes that connect the inner detector to the laboratory for cabling, calibration source delivery, xenon purification and cooling. These pipes represent gaps in the shielding, through which neutrons may pass and enter the liquid xenon. A parameter to describe the penetration of neutrons through a pipe can be written as:

$$\omega = \Omega \cdot \pi R^2 \cdot 10^{-\tau_w/100} \quad (3.14)$$

where Ω is the solid angle from the center of the opening to the end of the pipe, πR^2 is the cross-sectional area of the pipe and τ_w is the minimum thickness of water shielding (measured in mm) from the rock to the entrance of the pipe. The factor of $10^{-\tau_w/100}$ represents the attenuation of neutrons, which is approximately an order of magnitude for 10 cm of water. This parameter only considers the neutron flux coming perpendicularly to the entry of the pipe and assumes the flux of reflected neutrons, for example in a curved pipe, is negligible. Table 3.5 shows an inventory of all tubes/pipes/conduits that will be present during the science data taking and

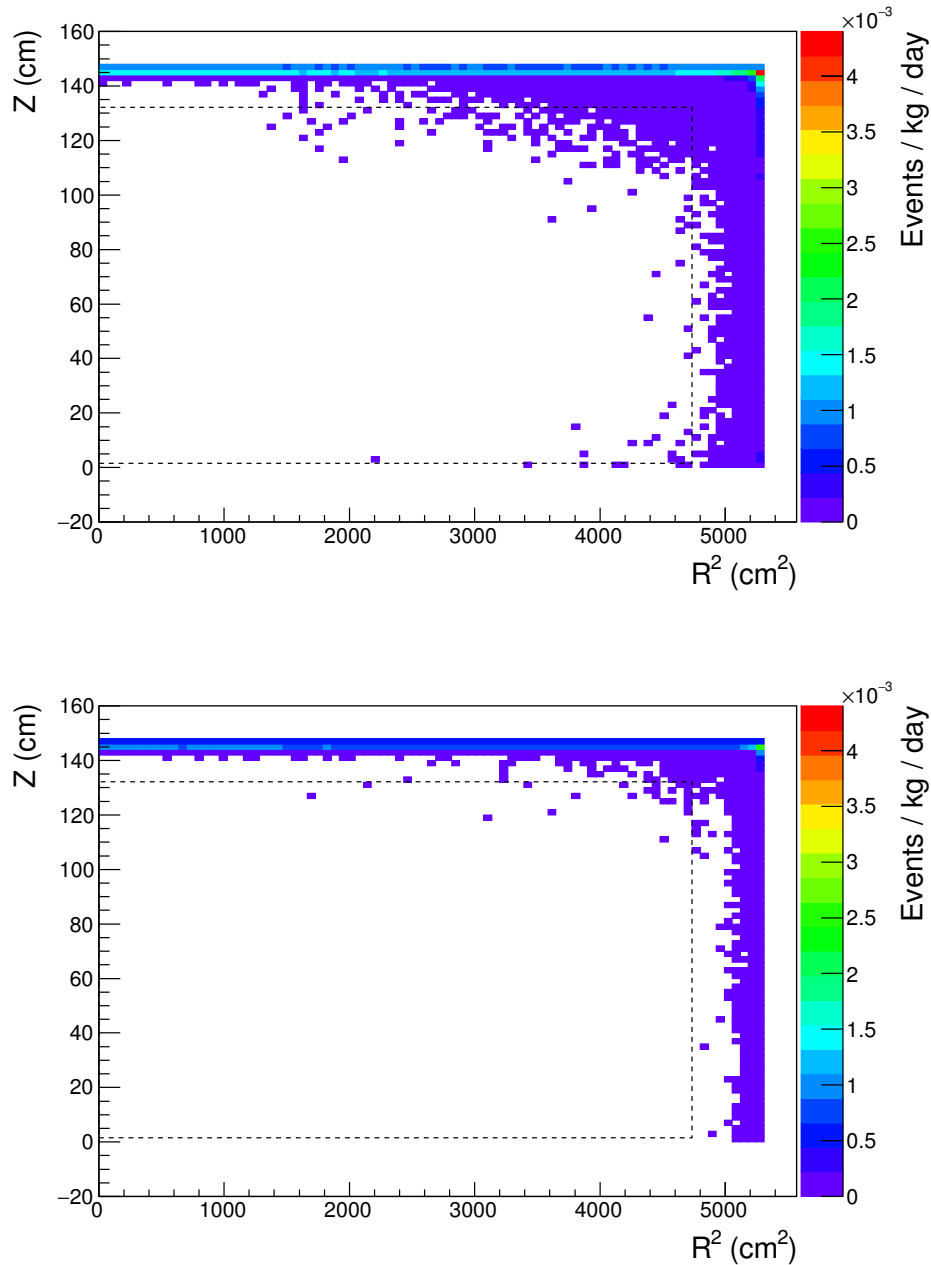


Figure 3.21: Distribution of events coming from gammas from ^{232}Th decays in the rock. The top plot shows all events depositing $< 150 \text{ keV}_{ee}$, and the bottom plot shows events surviving all analysis cuts and depositing $< 150 \text{ keV}_{ee}$. In both plots, only events occurring in the forward-field region of the TPC ($z > 0$) are shown. The dashed line represents the fiducial volume.

their corresponding ‘ ω -values’. The same components are also shown in the diagram in Figure 3.22. Two calibration tubes, one inclined and one horizontal, designed to deliver neutrons from a dedicated deuterium-deuterium (DD) source have not been considered since they will be filled with water after calibrations are completed. In addition, the high-voltage conduit that is attached to the TPC cathode is not considered since there is a large thickness of water between the edge of the water tank and the horizontal section of the conduit.

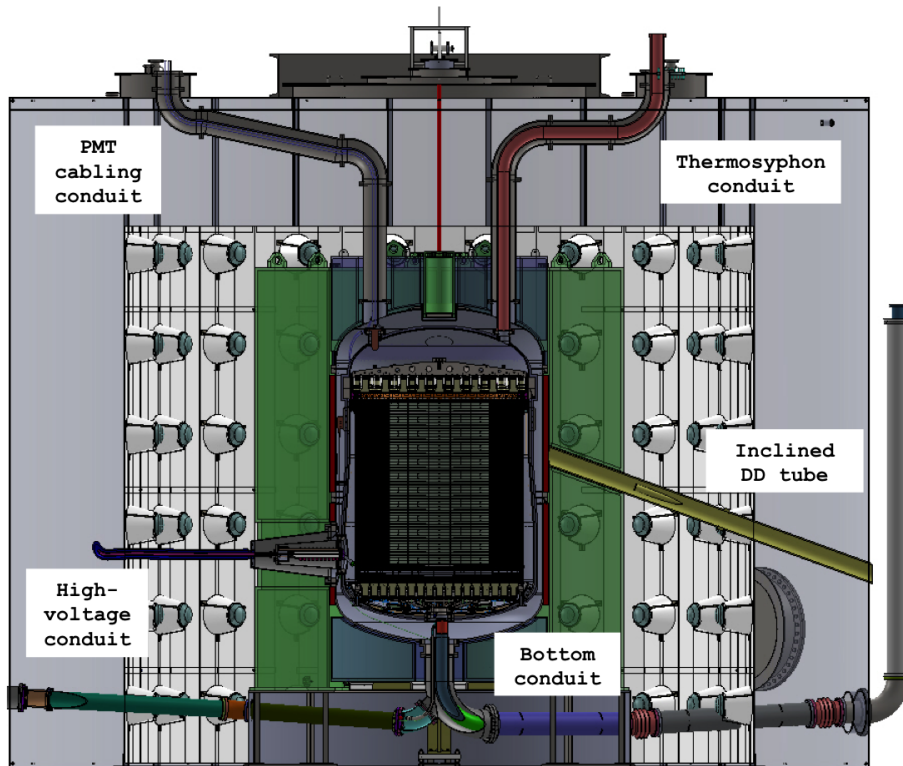


Figure 3.22: Diagram of the LZ detector highlighting the tubes/pipes/conduits that connect the inner detector with the laboratory [19]. Three vertical calibration delivery tubes and one horizontal neutron calibration tube on the opposite side of the detector are not shown.

Since the potential background from neutrons comes specifically from regions that are not shielded, simulations are designed to focus specifically on the most dangerous opening; the bottom conduit. To simulate neutrons passing through this section of the detector, a box is defined in the rock directly beneath the steel pyramid at the center of the water tank. The box measures $1 \times 1 \times 0.5$ m in x, y, z . The depth is informed by a preliminary simulation of 10^6 neutrons, which showed that the flux of neutrons at the TPC and scintillator originating from a distance > 0.5 m from the edge of steel pyramid is negligible.

Table 3.5: Summary of the conduits/pipes that connect the inner detector to the outside of the water tank (see 3.22) and the corresponding ‘ ω -value’. The bottom conduit will allow the passage of the most neutrons from the rock based on this metric.

	Length of pipe (mm)	Radius, R of pipe (mm)	Solid angle, Ω (sr)	Water shielding, τ_w (mm)	‘ ω -value’ $= \Omega \cdot \pi R^2 \cdot 10^{-\tau_w/100}$
Bottom conduit	871	102	4.23×10^{-2}	129	70
Theremophon conduit	1.49×10^3	80	9.10×10^{-3}	585	2.6×10^{-4}
PMT cabling conduit	1.62×10^3	110	1.44×10^{-3}	286	0.74
Vertical neutron tubes	2.06×10^3	23.7	4.2×10^{-4}	0	0.73

3.3.7 Spectra of neutrons from rock

The spectra (and yield) of neutrons coming from radioactivity in the cavern rock is calculated using a computer code called SOURCES4A [112]. As was discussed in Section 1.5.3, neutrons are produced from spontaneous fission and (α, n) reactions. The latter involves interactions of α particles with nuclei in the source material, and so the composition of the rock (see Table 2.4) and concentration of the radioactive isotope (see Table 3.16) is required as an input to the code. The code also contains libraries to describe the α energies (and intensities) coming from radioactive decay, the stopping power and energy losses of α particles and the cross-sections of reactions. The original SOURCES4A code was limited to α energies below 6.5 MeV, but has since been extended up to 10 MeV [113]. In addition, the cross-sections libraries for a large number of materials has been extended and improved [114, 115, 107], with cross-sections and branching ratios to excited states calculated using the EMPIRE-2.19 code [116]. As well as the libraries for dealing with (α, n) reactions, a library that describes the spectra of neutrons from spontaneous fission is also included.

The neutron spectra that is outputted by the SOURCES4A code is shown in Figure 3.23. Uranium contains contributions from the early chain of ^{238}U and from ^{235}U , whereas the thorium spectrum comes solely from ^{232}Th . The neutron yield (neutrons per decay) is $Y_U = 3.95 \times 10^{-6}$ n/decay for uranium and $Y_{Th} = 4.15 \times 10^{-6}$ n/decay for thorium.

3.3.8 Simulation, processing and final rate

For this study, neutrons have been generated within the cavern rock in a $1 \times 1 \times 0.5$ m region directly beneath the steel pyramid. They were then transported through the LZ detector setup using LUXSim and all interactions in the liquid xenon TPC, liquid xenon skin and scintillator are recorded for further processing. Neutrons with discrete energies in the range 0.05 - 9.95 MeV, with 0.1 MeV intervals, were generated as single particle sources each with a probability that reproduces the spectrum shown in Figure 3.23. In total, 8×10^8 neutrons from thorium and 24×10^8 neutrons have been processed using the Sheffield HEP computing cluster. For these simulations, the live time for a specific isotope, i , can be written as:

$$\tau_i [\text{days}] = \frac{N_n}{A_i [\text{Bq/kg}] \cdot M [\text{kg}] \cdot Y_i \cdot N_s} \quad (3.15)$$

where N_n is the number of simulated neutrons, A_i is the activity of the isotope, M is the mass of the source volume, Y_i is the neutron yield and $N_s = 8.64 \times 10^4$ is

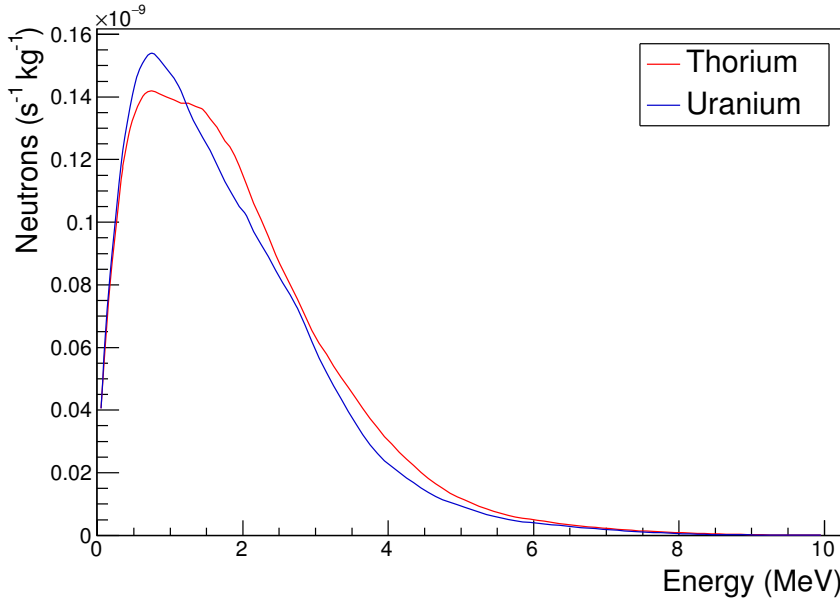


Figure 3.23: Spectra of neutrons from the cavern rock due to spontaneous fission and (α, n) reactions from ^{232}Th and ^{238}U decays. The spectra have been normalised assuming an activity of 1 mBq/kg.

the number of seconds a day. The mass of the source volume for neutrons in these simulations is $M = 1.35 \times 10^3$ kg. Using the activities listed in Table 3.16 and the yields from SOURCES4A ($Y_U = 3.95 \times 10^{-6}$ n/decay, $Y_{Th} = 4.15 \times 10^{-6}$ n/decay), the total live time is $\tau_U = 7.1 \times 10^4$ days for uranium and $\tau_U = 6.3 \times 10^4$ days for thorium.

The neutron files are processed through the same analysis framework as the simulations of gammas from rock. For both isotopes, there are no events above the 5 electron threshold ($S2 > 450$) and in the region of interest ($0 < S1c < 20$) even before any analysis cuts are applied. Using the Feldman-Cousins approach, as was done for muon-induced backgrounds in Section 2.2.9, the upper limit for the total exposure is 2.44 background events. Since neutrons are coming from both isotopes simultaneously, the upper limit on the total background from both uranium and thorium in 1000 days is $2.44 \times \frac{1000}{\tau}$, where $\tau = 6.3 \times 10^4$ days is the lowest simulated live-time from the two isotopes. So, the total background coming from neutrons beneath the bottom conduit is $< 3.9 \times 10^{-2}$ events in 1000 days.

It is possible to reduce this rate further by considering the extra rejection factor, f_R^i , that is expected for each isotope, i , after applying analysis cuts. These factors, which are calculated from previous simulations of neutrons from the cryostat vessels [16], are $f_R^U = 3.95 \times 10^{-5}$ and $f_R^{Th} = 3.85 \times 10^{-5}$ for uranium and thorium respectively. The

value for uranium is taken from simulations of the late chain, which produces more neutrons than the early chain. Using the same reasoning as before, the background rate is $< 1.5 \times 10^{-6}$ events in 1000 days. An important limitation of this final result are the uncertainties in applying a set of rejection factors for neutrons from the cryostat vessels to simulations of neutrons from the rock. Additionally, only one section of the cavern rock has been simulated, albeit the region that is expected to contribute the most background. These uncertainties are difficult to quantify, but the resulting background rate is so much smaller than the nuclear recoil background from detector components that it is safe to conclude that the contribution from the cavern rock will be subdominant.

Figure 3.24 shows a table of predicted backgrounds source and rates for the LZ experiment. The contribution of muon-induced particles and neutrons/gammas from rock, which have been described in this thesis, are included in the ‘Laboratory and Cosmogenics’ field. The result for this category of background also includes rates from cosmogenic activation, which are beyond the scope of this thesis. The electron recoil (ER) backgrounds for detector components, which is shown in the top half of the table, were calculated using the generator described in Section 3.1. It is clear that laboratory and cosmogenic backgrounds are subdominant to other sources, and that the current detector design does not need to be modified to introduce additional shielding or vetoing of backgrounds from these sources.

	Mass	$^{238}\text{U}_e$	$^{238}\text{U}_l$	$^{232}\text{Th}_e$	$^{232}\text{Th}_l$	^{60}Co	^{40}K	n/yr	ER	NR
	(kg)	mBq/kg							(cts)	(cts)
Upper PMT Structure	40.5	3.90	0.23	0.49	0.38	0.00	1.46	2.53	0.05	0.000
Lower PMT Structure	69.9	2.40	0.13	0.30	0.24	0.00	0.91	6.06	0.05	0.001
R11410 3" PMTs	91.9	71.6	3.20	3.12	2.99	2.82	15.4	81.8	1.46	0.013
R11410 PMT Bases	2.8	288	75.8	28.4	27.9	1.43	69.4	34.7	0.36	0.004
R8778 2" Skin PMTs	6.1	138	59.4	16.9	16.9	16.3	413	52.8	0.13	0.008
R8520 Skin 1" PMTs	2.2	60.5	5.19	4.75	4.75	24.2	333	4.60	0.02	0.001
R8520 PMT Bases	0.2	213	108	42.2	37.6	2.23	124	3.62	0.00	0.000
PMT Cabling	104	29.8	1.47	3.31	3.15	0.65	33.1	2.65	1.43	0.000
TPC PTFE	184	0.02	0.02	0.03	0.03	0.00	0.12	22.5	0.06	0.008
Grid Wires	0.8	1.20	0.27	0.33	0.49	1.60	0.40	0.02	0.00	0.000
Grid Holders	62.2	1.20	0.27	0.33	0.49	1.60	0.40	6.33	0.27	0.002
Field Shaping Rings	91.6	5.41	0.09	0.28	0.23	0.00	0.54	10.8	0.23	0.004
TPC Sensors	0.90	21.1	13.5	22.9	14.2	0.50	26.3	24.8	0.01	0.002
TPC Thermometers	0.06	336	90.5	38.5	25.0	7.26	3360	1.49	0.05	0.000
Xe Tubing	15.1	0.79	0.18	0.23	0.33	1.05	0.30	0.64	0.00	0.000
HV Components	138	1.90	2.00	0.50	0.60	1.40	1.20	4.90	0.04	0.001
Conduits	200	1.25	0.40	2.59	0.66	1.24	1.47	5.33	0.06	0.001
Cryostat Vessel	2410	1.59	0.11	0.29	0.25	0.07	0.56	124	0.63	0.013
Cryostat Seals	33.7	73.9	26.2	3.22	4.24	10.0	69.1	38.8	0.45	0.002
Cryostat Insulation	23.8	18.9	18.9	3.45	3.45	1.97	51.7	69.8	0.43	0.007
Cryostat Teflon Liner	26	0.02	0.02	0.03	0.03	0.00	0.12	3.18	0.00	0.000
Outer Detector Tanks	3200	0.16	0.39	0.02	0.06	0.04	5.36	78.0	0.45	0.001
Liquid Scintillator	17600	0.01	0.01	0.01	0.01	0.00	0.00	14.3	0.03	0.000
Outer Detector PMTs	205	570	470	395	388	0.00	534	7590	0.01	0.000
OD PMT Supports	770	1.20	0.27	0.33	0.49	1.60	0.40	14.3	0.00	0.000
Subtotal (Detector Components)									6.20	0.070
^{222}Rn (2.0 $\mu\text{Bq/kg}$)									722	-
^{220}Rn (0.1 $\mu\text{Bq/kg}$)									122	-
$^{\text{nat}}\text{Kr}$ (0.015 ppt (g/g))									24.5	-
$^{\text{nat}}\text{Ar}$ (0.45 ppt (g/g))									2.47	-
^{210}Bi (0.1 $\mu\text{Bq/kg}$)									40	-
Laboratory and Cosmogenics									4.3	0.06
Fixed Surface Contamination									0.19	0.37
Subtotal (Non-ν counts)									922	0.50
^{136}Xe 2 $\nu\beta\beta$									67	0.00
Astrophysical ν counts (pp + ^7Be + ^{13}N)									255	0.00
Astrophysical ν counts (^8B)									0.00	0.00
Astrophysical ν counts (hep)									0.00	0.21
Astrophysical ν counts (diffuse supernova)									0.00	0.05
Astrophysical ν counts (atmospheric)									0.00	0.46
Subtotal (Physics backgrounds)									322	0.72
Total									1,244	1.22
Total (with 99.5% ER discrimination, 50% NR efficiency)									6.22	0.61
Sum of ER and NR in LZ for 1,000 d, 5.6 tonne FV, with all analysis cuts									6.83	

Figure 3.24: Estimated background rates for the LZ experiment, parameterised as the number counts in 1000 days for a 5.6 ton fiducial volume [16].

Conclusions and outlook

Presently, there are several industrial-scale CCS projects currently operating throughout the world. The potential of this technology to regulate greenhouse gas emissions is huge, but it is still in its early stages of development and several technological challenges still need to be met. One such issue is the demand for a cheap and passive monitoring technology that can continuously verify the emplacement of carbon dioxide. The studies presented in this thesis seek to address that issue by exploring the possibility of using muon tomography to observe density changes caused by the migration of CO_2 after its injection into a storage reservoir. The work presented in Section 2.1 represents the first time a detailed study using a real geological repository has been undertaken to determine the feasibility of muon tomography for this application. The density changes in the storage reservoir have been accounted for using data from a detailed numerical model of CO_2 fluid dynamics, and the resulting changes in muon intensity and its angular dependence have been characterised. The conclusion is that there is a statistically significant change in the muon intensity to infer the presence of CO_2 in the reservoir within 50 days of detector operation. Furthermore, by considering the efficiency of muon detection with real borehole detectors and the expected backgrounds from local radioactivity, as described in Section 3.2, one can conclude that actually measuring these changes using a real detector is achievable. This requires an aggressive instrumentation strategy with many individual borehole detectors deployed over a relatively large area in order to detect a sufficient number of muons. Clearly there are economic implications of this strategy, which are beyond the scope of this thesis, but one can conclude that it is practically achievable. While it makes sense to view muon tomography as a technology that can compliment existing methods of CCS monitoring, future studies should look at how a tomographic image of a CO_2 plume can be determined from muon data. This would require clusters of detectors at multiple locations, which would increase costs, but may allow the geometric distribution of CO_2 to be mapped in the absence of data from other monitoring sources. The other focus of future study should be on the detectors themselves, and how the scintillator might

degrade over time, or fluctuate with the environmental conditions such as temperature. This needs to be well understood and accounted for in the analysis of muon data.

Although muons constitute a signal for muon tomography applications, they are a background for detectors seeking to observe rare events in underground experiments. In this thesis, the implications of muon-induced backgrounds for the LZ dark matter experiment have been considered, although the models and simulations that have been developed can be readily applied to other experiments. An upper limit on the nuclear recoil background rate has been calculated, and this has been shown to be sub-dominant to other sources background, most notably nuclear recoils from the interactions of neutrinos with xenon nuclei in the LZ detector medium. The effect of rock gamma and rock neutron backgrounds arising from radioisotopes in the laboratory walls of the Davis cavern - which will house the LZ detector - has also been quantified. Again, this contribution is sub-dominant to the other sources, particularly radon which makes up the majority of the electron recoil background budget. Although not discussed in this thesis, the rock gamma simulations can be useful for other low-background studies. For example, the rate of events from the rock can increase the experimental dead-time, since any signal above threshold in a veto detector results in a time window for all events to be thrown away. In the case of LZ, the Monte Carlo methods and code modifications presented in this work can be directly applied to understand the event rate in the outer detector and determine whether or not extra shielding is required or if any other modifications need to be made to the experimental setup. At present, the largest uncertainty in the rock gamma studies is the normalisation of the flux from the cavern. This systematic could be reduced by taking a direct measurement of the gamma spectrum inside of the (empty) water tank in the Davis laboratory.

Beyond the scope of this thesis, the radioactive decay generator described in Section 3.1 has been used to determine other radiogenic backgrounds in LZ, specifically those coming from detector components. In the short-term, this allows those materials contributing significantly to the background rate to be identified and either cleaned or acquired again. It also allows projections to be made about the sensitivity of the experiment. In the long-term, these simulations combined with data acquired when the detector becomes operational will be used to develop a complete background model. This is important, since a full understanding of detector backgrounds is crucial if a convincing claim for the direct detection of dark matter is to be made.

This thesis has more than 600 occurrences of the word ‘muon’, so it feels appropriate to end with a quote about that very particle. Regarding its discovery, the Nobel laureate Isidor Rabi famously exclaimed "*Who ordered that?*". Given the synergy of two very

different topics - one concerned with climate change, the other seeking to improve our fundamental knowledge of the universe - a reader might be forgiven for thinking the same thing about this thesis. Nevertheless, I hope it has made a contribution, however small, to the development of these fields of study.

References

- [1] Metz, B., et al., editors (2005). *Carbon dioxide capture and storage: special report of the intergovernmental panel on climate change*. Cambridge University Press.
- [2] Chadwick, R. A., Arts, R., and Eiken, O. (2005). 4D seismic quantification of a growing CO₂ plume at Sleipner, North Sea. In *Geological Society, London, Petroleum Geology Conference series*, volume 6, pages 1385–1399.
- [3] Telford, W. M., et al. (1990). *Applied Geophysics*. Cambridge University Press.
- [4] Arts, R., et al. (2008). Ten years' experience of monitoring CO₂ injection in the Utsira Sand at Sleipner offshore Norway. *First Break*, **26**, 65–72.
- [5] Vasco, D. W., et al. (2010). Satellite-based measurements of surface deformation reveal fluid flow associated with the geological storage of carbon dioxide. *Geophysical Research Letters*, **37**(3).
- [6] Patrighani, C. (2016). Review of Particle Physics. *Chinese Physics C*, **40**(10), 100001.
- [7] Longair, M. S. (2011). *High Energy Astrophysics*. Cambridge University Press.
- [8] Kudryavtsev, V. A. (2009). Muon simulation codes MUSIC and MUSUN for underground physics. *Computer Physics Communications*, **180**(3), 339–346.
- [9] Crouch, M. (1987). In *Proc. of the 20th International Cosmic Ray Conference*, volume 6, page 165.
- [10] Belolaptikov, I., et al. (1997). The Baikal underwater neutrino telescope: Design, performance, and first results. *Astroparticle Physics*, **7**(3), 263–282.
- [11] Andres, E., et al. (2000). The AMANDA neutrino telescope: principle of operation and first results. *Astroparticle Physics*, **13**(1), 1 – 20.
- [12] Decay Chain (n.d.). In *Wikipedia*. Retrieved October 2017, https://en.wikipedia.org/wiki/Decay_chain.
- [13] Pages, L., et al. (1972). Energy loss, range, and bremsstrahlung yield for 10-keV to 100-MeV electrons in various elements and chemical compounds. *Atomic Data and Nuclear Data Tables*, **4**, 1–27.
- [14] Sellars, R. (2012). Summer project report, University of Sheffield.

- [15] Klinger, J., et al. (2015). Simulation of muon radiography for monitoring CO₂ stored in a geological reservoir. *International Journal of Greenhouse Gas Control*, **42**, 644–654.
- [16] Mount, B. J., et al. (2017). LUX-ZEPLIN (LZ) Technical Design Report. *arXiv:1509.02910*.
- [17] Shaw, S. (2016). Identification of Dark Matter 2016, Sheffield, UK.
- [18] Akerib, D. S., et al. (2017). Signal yields, energy resolution, and recombination fluctuations in liquid xenon. *Phys. Rev. D*, **95**(1), 012008.
- [19] Hoff, M. (2017). Private communication.
- [20] Leung, D. Y. C., Caramanna, G., and Maroto-Valer, M. M. (2014). An overview of current status of carbon dioxide capture and storage technologies. *Renewable and Sustainable Energy Reviews*, **39**, 426–443.
- [21] Smith, N. J. T. (2012). The Current Status and Planned Developments for Deep Underground Astro-particle Physics Science Facilities. *Journal of Physics: Conference Series*, **375**(4), 042059.
- [22] Mei, D.-M., et al. (2010). Early results on radioactive background characterization for Sanford Laboratory and DUSEL experiments. *Astroparticle Physics*, **34**(1), 33–39.
- [23] Chadwick, M., et al. (2011). ENDF/B-VII.1 Nuclear Data for Science and Technology: Cross Sections, Covariances, Fission Product Yields and Decay Data. *Nuclear Data Sheets*, **112**(12), 2887 – 2996. Special Issue on ENDF/B-VII.1 Library.
- [24] Tables of X-Ray Mass Attenuation Coefficients and Mass Energy-Absorption Coefficients (version 1.4). Available: <http://physics.nist.gov/xaamdi> (Accessed June 2017).
- [25] Stocker, T. (2014). *Climate change 2013: the physical science basis: Working Group I contribution to the Fifth assessment report of the Intergovernmental Panel on Climate Change*. Cambridge University Press.
- [26] Nakicenovic, N. and Swart, R. (2000). Intergovernmental Panel on Climate Change: Special Report on Emissions Scenarios.
- [27] Scott, V., et al. (2013). Last chance for carbon capture and storage. *Nature Climate Change*, **3**(2), 105.
- [28] Holloway, S. and Savage, D. (1993). The potential for aquifer disposal of carbon dioxide in the UK. *Energy Conversion and Management*, **34**, 925–932.
- [29] Koide, H., et al. (1993). Underground storage of carbon dioxide in depleted natural gas reservoirs and in useless aquifers. *Engineering Geology*, **34**(3-4), 175–179.

- [30] Eiken, O., et al. (2011). Lessons Learned from 14 years of CCS Operations: Sleipner, In Salah and Snøhvit. In *Energy Procedia*, volume 4, pages 5541–5548. Elsevier.
- [31] Thomas, D. C. and Benson, S. M. (2005). *Carbon dioxide capture for storage in deep geologic formations-results from the CO₂ Capture Project: Vol 2-Geologic Storage of Carbon Dioxide with Monitoring and Verification*. Elsevier.
- [32] Emberley, S., et al. (2004). Geochemical monitoring of fluid-rock interaction and CO₂ storage at the Weyburn CO₂-injection enhanced oil recovery site, Saskatchewan, Canada. *Energy*, **29**(9-10), 1393–1401.
- [33] Ringrose, P., et al. (2013). The In Salah CO₂ Storage Project: Lessons Learned and Knowledge Transfer. In *Energy Procedia*, volume 37, pages 6226–6236.
- [34] Studlick, J. R. J., et al. (1990). *A Giant Carbon Dioxide Accumulation in the Norphlet Formation, Pisgah Anticline, Mississippi*, pages 181–203. Springer New York.
- [35] Thibeau, S. and Mucha, V. (2011). Have we overestimated saline aquifer CO₂ storage capacities? *Oil & Gas Science and Technology—Revue d'IFP Energies nouvelles*, **66**(1), 81–92.
- [36] Cavanagh, A. and Wildgust, N. (2011). Pressurization and brine displacement issues for deep saline formation CO₂ storage. In *Energy Procedia*, volume 4, pages 4814–4821.
- [37] Baines, S. J. and Worden, R. H. (2004). Geological storage of carbon dioxide. *Geological Society, London, Special Publications*, **233**(1), 1–6.
- [38] Doyle, H. (1995). *Seismology*. Wiley.
- [39] Arts, R., et al. (2004). Monitoring of CO₂ injected at Sleipner using time-lapse seismic data. *Energy*, **29**(9-10), 1383–1392.
- [40] Berryman, J. G. (1999). Origin of Gassmann's equations. *Geophysics*, **64**(5), 1627–1629.
- [41] Nooner, S. L., et al. (2007). Constraints on the in situ density of CO₂ within the Utsira formation from time-lapse seafloor gravity measurements. *International Journal of Greenhouse Gas Control*, **1**(2), 198–214.
- [42] Alnes, H., et al. (2011). Results from Sleipner gravity monitoring: Updated density and temperature distribution of the CO₂ plume. In *Energy Procedia*, volume 4, pages 5504–5511. Elsevier.
- [43] Gaisser, T. K. (1990). *Cosmic rays and particle physics*. Cambridge University Press.
- [44] Aglietta, M., et al. (1998). Muon “depth-intensity” relation measured by the LVD underground experiment and cosmic-ray muon spectrum at sea level. *Physical Review D*, **58**(9), 092005.

- [45] Aglietta, M., et al. (1999). Upper limit on the prompt muon flux derived from the LVD underground experiment. *Physical Review D - Particles, Fields, Gravitation and Cosmology*, **60**(11), 112001.
- [46] Kudryavtsev, V. A., et al. (2012). Monitoring subsurface CO2 emplacement and security of storage using muon tomography. *International Journal of Greenhouse Gas Control*, **11**, 21–24.
- [47] Bethe, H. A. (1953). Molière’s Theory of Multiple Scattering. *Physical Review*, **89**(6), 1256–1266.
- [48] Rossi, B. B. (1952). *High-energy particles*. Prentice-Hall.
- [49] Antonioli, P., et al. (1997). A three-dimensional code for muon propagation through the rock: MUSIC. *Astroparticle Physics*, **7**(4), 357–368.
- [50] Lipari, P. and Stanev, T. (1991). Propagation of multi-TeV muons. *Physical Review D*, **44**(11), 3543–3554.
- [51] Sokalski, I. A., Bugaev, E. V., and Klimushin, S. I. (2001). MUM: Flexible precise Monte Carlo algorithm for muon propagation through thick layers of matter. *Physical Review D*, **64**(7), 074015.
- [52] Chirkin, D. and Rhode, W. (2004). Propagating leptons through matter with Muon Monte Carlo (MMC). *arXiv:hep-ph/0407075*.
- [53] Agostinelli, S., et al. (2003). Geant4 - a simulation toolkit. *Nuclear Instruments and Methods in Physics Research Section A: Accelerators, Spectrometers, Detectors and Associated Equipment*, **506**, 250–303.
- [54] Ferrari, A., et al. (2005). FLUKA: A Multi-Particle Transport Code. *Slac*, **773**(October), 406.
- [55] Böhlen, T. T., et al. (2014). The FLUKA Code: Developments and challenges for high energy and medical applications. *Nuclear Data Sheets*, **120**, 211–214.
- [56] Alvarez, L. W., et al. (1970). Search for Hidden Chambers in the Pyramids. *Science*, **167**(3919), 832–839.
- [57] Marteau, J., et al. (2012). Muons tomography applied to geosciences and volcanology. In *Nuclear Instruments and Methods in Physics Research, Section A: Accelerators, Spectrometers, Detectors and Associated Equipment*, volume 695, pages 23–28.
- [58] Kanetada, N. (1995). Geo-tomographic observation of inner-structure of volcano with cosmic-ray muons. *Journal of Geography (Chigaku Zasshi)*, **104**(7), 998–1007.
- [59] Bryman, D., Bueno, J., and Jansen, J. (2015). Blind Test of Muon Geotomography for Mineral Exploration. *ASEG Extended Abstracts*, **2015**(1), 1.
- [60] Borozdin, K. N., et al. (2003). Surveillance: Radiographic imaging with cosmic-ray muons. *Nature*, **422**, 277–278.

-
- [61] Priedhorsky, W. C., et al. (2003). Detection of high-Z objects using multiple scattering of cosmic ray muons. *Review of Scientific Instruments*, **74**(10), 4294–4297.
- [62] Furlan, M., et al. (2014). Application of muon tomography to detect radioactive sources hidden in scrap metal containers. *IEEE Transactions on Nuclear Science*, **61**(4), 2204–2209.
- [63] Bonneville, A., et al. (2017). A novel muon detector for borehole density tomography. *Nuclear Instruments and Methods in Physics Research, Section A: Accelerators, Spectrometers, Detectors and Associated Equipment*, **851**, 108–117.
- [64] Akerib, D. S., et al. (2017). Results from a Search for Dark Matter in the Complete LUX Exposure. *Phys. Rev. Lett.*, **118**(2), 21303.
- [65] Eguchi, K., et al. (2003). First Results from KamLAND: Evidence for Reactor Antineutrino Disappearance. *Physical Review Letters*, **90**(2), 021802.
- [66] Robinson, M., et al. (2003). Measurements of muon flux at 1070 m vertical depth in the Boulby underground laboratory. *Nuclear Instruments and Methods in Physics Research, Section A: Accelerators, Spectrometers, Detectors and Associated Equipment*, **511**(3), 347–353.
- [67] Cribier, M., et al. (1997). The muon induced background in the GALLEX experiment. *Astroparticle Physics*, **6**(2), 129–141.
- [68] Aglietta, M., et al. (1994). Single muon angular distributions observed in the LVD particle astrophysics experiment. *Astroparticle Physics*, **2**(2), 103–116.
- [69] Ahlen, S., et al. (1992). Study of the ultrahigh-energy primary-cosmic-ray composition with the MACRO experiment. *Physical Review D*, **46**(3), 895–902.
- [70] Abgrall, N., et al. (2017). Muon flux measurements at the davis campus of the sanford underground research facility with the majorana demonstrator veto system. *Astroparticle Physics*, **93**(1), 70–75.
- [71] Berger, C., et al. (1989). Experimental study of muon bundles observed in the Fréjus detector. *Physical Review D*, **40**(7), 2163–2171.
- [72] Waltham, C. (2000). XIX International Conference on Neutrino Physics & Astrophysics, Sudbury, Canada.
- [73] Yu-Cheng, W., et al. (2013). Measurement of cosmic ray flux in the China JinPing underground laboratory. *Chinese Physics C*, **37**(8), 086001.
- [74] Mei, D.-M. and Hime, A. (2006). Muon-induced background study for underground laboratories. *Phys. Rev.*, **D73**, 53004.
- [75] Reichhart, L., et al. (2013). Measurement and simulation of the muon-induced neutron yield in lead. *Astroparticle Physics*, **47**, 67–76.
- [76] Lindote, A., et al. (2009). Simulation of neutrons produced by high-energy muons underground. *Astroparticle Physics*, **31**(5), 366–375.

- [77] Araújo, H. M., et al. (2005). Muon-induced neutron production and detection with GEANT4 and FLUKA. *Nuclear Instruments and Methods in Physics Research Section A: Accelerators, Spectrometers, Detectors and Associated Equipment*, **545**(1-2), 398–411.
- [78] Kudryavtsev, V. A., Spooner, N. J. C., and McMillan, J. E. (2003). Simulations of muon induced neutron flux at large depths underground. *Nucl. Instrum. Meth.*, **A505**, 688–698.
- [79] Aprile, E., et al. (2012). Dark Matter Results from 225 Live Days of XENON100 Data. *Physical Review Letters*, **109**(18), 181301.
- [80] Bateman, H. (1910). In *Proceedings of the Cambridge Philosophical Society*, volume 15, pages 423–427.
- [81] Afghoul, A., et al. (2004). Coiled tubing: the next generation. *Oilfield Rev*, **6**(4), 9–23.
- [82] Hill, D., et al. (1996). Reentry drilling gives new life to aging fields. *Oilfield review*, **8**(3), 4–17.
- [83] Brun, R. and Rademakers, F. (1997). ROOT—an object oriented data analysis framework. *Nuclear Instruments and Methods in Physics Research Section A: Accelerators, Spectrometers, Detectors and Associated Equipment*, **389**(1-2), 81–86.
- [84] Murphy, A. and Paling, S. (2012). The Boulby Mine Underground Science Facility: The Search for Dark Matter, and Beyond. *Nuclear Physics News*, **22**(1), 19–24.
- [85] Lincoln, D., et al. (2014). Coupled two-component flow in deformable fractured porous media with application to modelling geological carbon storage. *Numerical Methods in Geotechnical Engineering*, pages 989–994.
- [86] Lincoln, D. (2015). Ph.D. thesis, University of Sheffield.
- [87] Lewis, R. W. and Schrefler, B. A. (1998). *The finite element method in the static and dynamic deformation and consolidation of porous media*. John Wiley.
- [88] Nordbotten, J. M., Celia, M. A., and Bachu, S. (2005). Injection and Storage of CO₂ in Deep Saline Aquifers: Analytical Solution for CO₂ Plume Evolution During Injection. *Transport in Porous Media*, **58**(3), 339–360.
- [89] Richardson, M. (2016). Ph.D. thesis, University of Sheffield.
- [90] Cherry, M. L., et al. (1983). Multiple muons in the Homestake underground detector. *Phys. Rev. D*, **27**(7), 1444–1447.
- [91] Akerib, D., et al. (2012). LUXSim: A component-centric approach to low-background simulations. *Nuclear Instruments and Methods in Physics Research Section A: Accelerators, Spectrometers, Detectors and Associated Equipment*, **675**, 63–77.

- [92] Geant4 Physics Reference Manual available from <http://cern.ch/geant4>.
- [93] The XENON Collaboration (2016). Physics reach of the XENON1T dark matter experiment. *Journal of Cosmology and Astroparticle Physics*, **2016**(04), 027.
- [94] Tan, A., et al. (2016). Dark Matter Results from First 98.7 Days of Data from the PandaX-II Experiment. *Physical Review Letters*, **117**(12), 121303.
- [95] Agnes, P., et al. (2015). First results from the DarkSide-50 dark matter experiment at Laboratori Nazionali del Gran Sasso. *Physics Letters, Section B: Nuclear, Elementary Particle and High-Energy Physics*, **743**, 456–466.
- [96] Rubbia, A. (2006). ArDM: a ton-scale liquid Argon experiment for direct detection of Dark Matter in the Universe. *Journal of Physics: Conference Series*, **39**, 129–132.
- [97] Chepel, V. and Araújo, H. (2013). Liquid noble gas detectors for low energy particle physics. *Journal of Instrumentation*, **8**(04), R04001.
- [98] Dahl, C. E. (2009). Ph.D. thesis, Princeton University.
- [99] Aprile, E. and Doke, T. (2010). Liquid xenon detectors for particle physics and astrophysics. *Reviews of Modern Physics*, **82**(3), 2053–2097.
- [100] Akerib, D. S., et al. (2016). Tritium calibration of the LUX dark matter experiment. *Physical Review D*, **93**(7), 072009.
- [101] Lewin, J. and Smith, P. (1996). Review of mathematics, numerical factors, and corrections for dark matter experiments based on elastic nuclear recoil. *Astroparticle Physics*, **6**, 87–112.
- [102] Feldman, G. J. and Cousins, R. D. (1998). Unified approach to the classical statistical analysis of small signals. *Physical Review D*, **57**(7), 3873.
- [103] Kinsey, R., et al. (1996). The NUDAT/PCNUDAT program for nuclear data. Technical report, Brookhaven National Lab., Upton, NY (United States).
- [104] Schön, J. H. (2015). Physical Properties of Rocks: Fundamentals and Principles of Petrophysics (2nd edition). *Developments in Petroleum Science (Elsevier)*, **65**, 499.
- [105] Vo, H. H., et al. (2008). Energy resolution of plastic scintillation detector for beta rays. *IEEE Transactions on Nuclear Science*, **55**(6), 3717–3724.
- [106] Hubbell, J. H. and Seltzer, S. M. Tables of X-ray mass attenuation coefficients and mass energy-absorption coefficients 1 keV to 20 MeV for elements $Z = 1$ to 92 and 48 additional substances of dosimetric interest.
- [107] Tomasello, V., Robinson, M., and Kudryavtsev, V. A. (2010). Radioactive background in a cryogenic dark matter experiment. *Astroparticle Physics*, **34**(2), 70–79.

-
- [108] Szydagis, M., et al. (2013). Enhancement of NEST capabilities for simulating low-energy recoils in liquid xenon. *Journal of Instrumentation*, **8**(10), C10003.
- [109] Schattke, W. and Van Hove, M. A. (2008). *Solid-state photoemission and related methods: Theory and experiment*. John Wiley & Sons.
- [110] Fominykh, N., et al. (2000). Theory of two-electron photoemission from surfaces. *Solid State Communications*, **113**(12), 665–669.
- [111] Faham, C. H., et al. (2015). Measurements of wavelength-dependent double photoelectron emission from single photons in VUV-sensitive photomultiplier tubes. *Journal of Instrumentation*, **09010**(09), 9010.
- [112] Wilson, W. B., et al. (2009). Sources: A code for calculating (α , n), spontaneous fission, and delayed neutron sources and spectra. *Progress in Nuclear Energy*, **51**(4-5), 608–613.
- [113] Carson, M. J., et al. (2004). Neutron background in large-scale xenon detectors for dark matter searches. *Astroparticle Physics*, **21**(6), 667–687.
- [114] Lemrani, R., et al. (2006). Low-energy neutron propagation in MCNPX and GEANT4. *Nuclear Instruments and Methods in Physics Research, Section A: Accelerators, Spectrometers, Detectors and Associated Equipment*, **560**(2), 454–459.
- [115] Tomasello, V., Kudryavtsev, V. A., and Robinson, M. (2008). Calculation of neutron background for underground experiments. *Nuclear Instruments and Methods in Physics Research, Section A: Accelerators, Spectrometers, Detectors and Associated Equipment*, **595**(2), 431–438.
- [116] Herman, M., et al. (2007). EMPIRE: Nuclear Reaction Model Code System for Data Evaluation. *Nuclear Data Sheets*, **108**(12), 2655–2715.